OPTICAL FIBER PHOTOTHERMAL SPECTROSCOPY FOR GAS SENSORS AND PHASE MODULATORS

GUO LINHAO

PhD

The Hong Kong Polytechnic University

2025

The Hong Kong Polytechnic University

Department of Electrical and Electronic Engineering

Optical fiber photothermal spectroscopy for gas sensors and phase modulators

GUO Linhao

A thesis submitted in partial fulfilment of the requirements for the degree of Doctor of Philosophy

Dec 2024

CERTIFICATE OF ORIGINALITY

I hereby declare that this thesis is my own work and that, to the best of my knowledge and belief, it reproduces no material previously published or written, nor material that has been accepted for the award of any other degree or diploma, except where due acknowledgement has been made in the text.

_____(Signed)

GUO Linhao (Name of student)

Abstract

Optical fiber photothermal spectroscopy (PTS) has been used for gas sensors over the last decade, with high selectivity and sensitivity. Involving a pump-probe configuration, PTS with hollow core fibers (HCFs) enables efficient photothermal (PT) phase modulation at frequencies up to tens of kHz, which ensures gas detection with high signal-to-noise ratio (SNR). In this thesis, we conduct further research to improve the sensor performance and reduce the cost, with an ultra-compact gas sensor using single mode fibers (SMFs) for real-time gas detection, and pump-probe-alternating and Fourier-transform-PTS techniques for multi-component gas sensing. Meanwhile we explore another application of the PTS for phase modulators (PMs).

Real-time gas sensing is very important from daily life to the industrial and agricultural production. Thus, we propose a miniature optical fiber PT gas sensor with fast response and large dynamic range. The sensing region is an air gap formed between the cleaved ends of two SMFs. Theoretical formulations of photothermal phase modulation and interferometric phase detection are presented. Numerical simulation and experimental investigation are carried out to optimize the system parameters to maximize the photothermal signal. A gas sensor with an air gap of 130 μm demonstrates a noise equivalent concentration (NEC) of 45 ppb and dynamic range of 2×10^7 for acetylene (C_2H_2) detection, with a response time of 0.9 s. The sensor is simple to construct and may be used for real-time gas detection in a confined space.

Moreover, in conventional fiber optical PTS (FO-PTS) systems, in addition to the pump lasers tuned to the specific absorption lines of the target gas species, an additional laser is used as the probe beam for PT phase detection. For this, we demonstrate an C_2H_2 /methane (CH_4) gas sensor based on HCF-PTS with a pump–probe-alternating technique. This technique utilizes two distributed-feedback lasers as pump and probe

beams alternatively for two gas components through time-division multiplexing. With a 2.5-cm-long HCF, NECs of 370 ppb and 130 ppb are demonstrated for methane and acetylene, respectively. The proposed technique eliminates the need for an additional laser in the traditional PTS setup, enabling the construction of a sensitive yet more cost-effective multi-component gas detection system.

Furthermore, as the number of targeted gas species increases, FO-PTS systems normally require more pump lasers. To counteract this, we demonstrate a gas sensor by combining the techniques of HCF-enhanced FO-PTS with Fourier transform spectroscopy. A broadband light source (BLS) is used as the pump beam, with the light intensity modulated at different frequencies for different wavenumbers by passing through a scanning two-beam interferometer. The PT spectrum is obtained by Fourier transform of the measured interferogram. With a 10-cm-long HCF, NECs of ~465 ppb and ~457 ppm are demonstrated for C_2H_2 and carbon dioxide (CO_2), respectively, with only one pump beam. Detection of the two-component gas of C_2H_2 and CO_2 is demonstrated with the same system. The proposed method enables the construction of a PTS system with a compact size for multi-component gas detection.

Meanwhile, we explore the PTS for the application of PMs with HCFs. We study the effect of varying gas concentration, buffer gas, length and type of fibers on the performance of optical fiber photothermal PMs based on C_2H_2-filled hollow-core fibers. For the same control power level, the PM with Ar as the buffer gas achieves largest phase modulation. For a fixed length of hollow-core fiber, there exists an optimal C_2H_2 concentration that achieves the largest phase modulation. With a 23-cm-long hollow-core anti-resonant fiber filled with 12.5% C_2H_2 balanced with Ar, phase modulation of π-rad at 100 kHz is achieved with a control power of 200 mW. The modulation bandwidth of the PM is 150 kHz. The modulation bandwidth is extended to ~1.1 MHz with a hollow-core photonic bandgap fiber (HC-PBGF) of the same length filled with the same gas mixture. The measured rise and fall time of HC-PBGF PM are 0.57 μs and

0.55 μs, respectively.

Acknowledgements

First, I would like to express my profound sincere thanks to my supervisor Prof. Wei Jin for giving me this opportunity to work with him and meet many outstanding colleagues in my PhD study. His broad vision, professional guidance and endless patience help and inspire me a lot. His research attitude with innovation, responsibility, and intellectual rigor and integrity would continuously encourage me in my future career.

Special thanks go to Dr. Hoi Lut Ho, Prof. Haihong Bao, Dr. Pengcheng Zhao, and Dr. Shoulin Jiang for your useful and inspiring discussions and kind help, especially at the early stage of my PhD journey.

My heartfelt appreciation goes out to my colleagues Dr. Feifang Chen, Dr. Yingzhen Hong, Dr. Shuangxiang Zhao, Dr. Kaiyuan Zheng, Dr. Yun Qi, Dr. Yan Zhao, Prof. Chao Wang, Mr. Hanyu Liao, Miss Jingwen Wu and Miss Mengrui Han for your generous assistance during my PhD studies.

I would also acknowledge Prof. Yingying Wang and Dr. Shoufei Gao for kindly providing us the hollow-core fibers.

Finally, I would like to thank my loving wife and parents for their love, encouragement and support.

Publications Arising from the Thesis

Journal articles

[1] **L.H. Guo**, H.H. Bao, F.F. Chen, P.C. Zhao, S.L. Jiang, H.L. Ho, and W. Jin, “Ultra-compact optical fiber gas sensor with high sensitivity, fast response and large dynamic range,” J. Lightw. Technol. 42, 2617-2624 (2023).

[2] **L.H. Guo**, S.L. Jiang, S.F. Gao, Y.Y. Wang, S.X. Zhao, H.L. Ho, and W. Jin, “Parameter optimization of hollow-core optical fiber phase modulators,” Opt. Lett. 48, 3335-3338 (2023).

[3] **L.H. Guo**, P.C. Zhao, H.L. Ho, S.L. Jiang, H.H. Bao, S.F. Gao, Y.Y. Wang, S.X. Zhao, H.L. Ho, and W. Jin, “Pump–probe-alternating photothermal interferometry for two-component gas sensing,” Opt. Lett. 48, 6440-6443 (2023).

[4] P.C. Zhao, K.V. Krishnaiah, **L.H. Guo**, T.G. Li, H.L. Ho, A.P. Zhang, W. Jin, “Ultraminiature Optical Fiber-Tip 3D-Microprinted Photothermal Interferometric Gas Sensors,” Laser Photonics Rev. 2301285, 1-8 (2024).

Conference articles

[1] **L.H. Guo**, P.C. Zhao, S.L. Jiang, H.H. Bao, S.F. Gao, Y.Y. Wang, H. L. Ho, and W. Jin, "Two-component photothermal gas sensor with a pump-probe-alternating technique," in 28th International Conference on Optical Fiber Sensors, Technical Digest Series (Optica Publishing Group). paper Tu3.16 (2023).

[2] P.C. Zhao, K.V. Krishnaiah, **L.H. Guo**, T.G. Li, H.L. Ho, A.P. Zhang, W. Jin, "High-sensitivity fiber-tip photothermal gas sensor based on a 3D μ-printed Fabry-Pérot microcavity," in 28th International Conference on Optical Fiber Sensors, Technical

Digest Series (Optica Publishing Group), paper Th5.2 (2023).

Table of Contents

List of Figures

reflected probe beams are obtained from the two endfaces, respectively. (c) Normalized intensity distribution of the incident laser after leaving the left end face. (d) Schematic of light propagation in the SMF and the air gap. n' and n are RI of the silica fiber and gas, respectively.

Figure 3.2 (a) Measured interferometric fringes of the FPI with gap distance of 130 μm. (b) Experimental and calculated results of the fringe contrast as functions of gap distance.

Figure 3.3 (a) Schematic of the simulation model. (b) Calculated results of I_r in time domain for a pump modulation frequency of 2 kHz. The gap distance is 130 μm. The inset is the evolution of temperature distribution along axis of symmetry from z=0 to z=130 μm during half a period indicated by the red dotted box. (c) Normalized laser intensity distribution, (d) heat source distribution, (e) temperature distribution, and (f) RI distribution in the gap at the time of 1 ms. The contour lines in (e-f) are used to indicate the gradient of the change.

Figure 3.4 (a) Experimental setup for measuring frequency response. OC: optical circulator, PD: photodetector. (b) Experimental and calculated results of frequency response of the sensor with the gap distance of 130 μm. (c) Experimental and calculated -3-dB roll-off frequencies.

Figure 3.5 Influence of gap distance on PT signal. (a) Calculated phase modulation amplitude for pump modulation frequency of 20 kHz. (b) Experimental and calculated results of ΔI_r at the modulation frequency of 20 kHz.

Figure 3.6 Gas detection with a sensor with the gap distance of 130 μm. (a) Experimental setup. LC: laser controller. (b) Measured LIA 2*f* output of the PT phase modulation for different pump power from 20 dBm to 28 dBm. The gas is 1% C_2H_2 balanced with N_2. (c) Experimental results and linear fit of p-p values of the LIA 2*f*

Figure 5.2. (a) Measured spectrum of the BLS with an optical spectrometer. (b) Calculated absorption coefficient of 0.02% C_2H_2, 0.1% NH_3, 100% CO_2, 100% H_2S and 100% H_2O from HITRAN database [14]. (c) Generation of the pump beam from the BLS through a scanning Michelson interferometer, and detection of the PT-phase modulation of the probe beam through a Fabry-Perot interferometer. (d) Spectral transmission of a 2-m-long HC-CTF, with its cross-section image on the left inset. The right inset is the spectral transmission to indicate the position of the probe beam and the BLS.

Figure 5.3. (a) Experimental setup for measuring the pump spectrum. (b) Interferogram of the pump signal after equal interval sampling. (c) Measured and fitted spectra of the pump spectrum. (d) Loss spectrum of the SMI.

Figure 5.4. Simulation of the phase modulation of fiber-enhanced FT-PTS. (a) Interferogram of the phase modulation for acetylene detection. The inset is the simulation model. (b) Phase spectrum by Fourier transform of the interferogram shown in (a).

Figure 5.5 Experimental setup for gas sensing based on the FT-PTS with an HC-CTF. HPF: high-pass filter. LPF: low-pass filter.

Figure 5.6. (a) The measured interferogram of the photothermal signal. The HCF is filled with 1000-ppm C_2H_2 balanced with N_2. (b) The measured PT spectrum by Fourier transform of the interferogram shown in (a). (c) The interferogram by inverse Fourier transform of the spectrum shown in the red dashed box of (b) with removal of the low-frequency components. (d) The measured PT spectrum by Fourier transform of the interferogram for 1000-ppm C_2H_2, and the simulated PT spectrum. (e) The measured PT spectra for different C_2H_2 concentration from 200 ppm to 1000 ppm. (f) The fitting coefficient x_1 and (g) the solved concentration as functions of the input C_2H_2 concentration with reference spectrum of 1000-ppm C_2H_2. The input pump power is

~45 mW. The buff gas is N_2.

Figure 5.7. (a) The measured interferogram of the photothermal signal. The HCF is filled with 100% CO_2. (b) The measured PT spectrum by Fourier transform of the interferogram shown in (a). (c) The interferogram by inverse Fourier transform of the spectrum shown in the red dashed box of (b) with removal of the low-frequency components. (d) The measured PT spectrum by Fourier transform of the interferogram for 100% CO_2, and the simulated PT spectrum. (e) The measured PT spectra for different CO_2 concentration from 20% to 100%. (f) The fitting coefficient and (d) the solved concentration as functions of the input CO_2 concentration with reference spectrum of 100% CO_2. The input pump power is ~45 mW. The buff gas is N_2.

Figure 5.8. (a) Calculated absorption coefficient of 100% CO_2 and 200-ppm C_2H_2 from HITRAN database. (b) The measured PT spectrum with the HCF filled with a fixed C_2H_2 concentration of 200 ppm under different CO_2 concentration from 0 to 80%. (c) The calculated spectrum by subtracting the corresponding spectrum of high-concentration CO_2 shown in Fig. 5.7(e) from the spectrum of the gas mixture shown in (b). (d) The fitting coefficient of the C_2H_2 spectra in (c) as functions of the CO_2 concentration with the reference spectrum of 1000-ppm C_2H_2. The input pump power is ~45 mW. The buff gas is N_2.

Figure 5.9. (a) The measured PT spectrum with the HCF filled with a gas mixture of 60% CO_2 and 400-ppm C_2H_2 and the fitted individual spectra for CO_2 and C_2H_2 from the gas mixture. (b) The residual between the measured PT spectrum and the fitted spectrum by adding the fitted CO_2 spectrum with C_2H_2 spectrum shown in (a). The input pump power is ~45 mW. The buff gas is N_2.

Figure 6.1 Basics and parameters of PM with a gas-filled HCF. The insets are cross-sections of HC-ARF and HC-PBGF, respectively.

Figure 6.2 (a) Experimental setup for characterizing the PM. LPF, low-pass filter. (b) Voltage output from the MZI (PD2) with and without servo control. (c) Operating phase of the MZI with phase stabilization, where phase fluctuation is stabilized around the quadrature point.

Figure 6.3 Phase modulation as a function of P_{ctrl} for a 23-cm-long HC-ARF filled with 5% C_2H_2 in different buffer gases of Ar, N_2 and He. The modulation frequency is 100 kHz.

Figure 6.4 (a) Absorbance and (b) phase modulation amplitude as a function of C_2H_2 concentration for three PMs using HC-ARFs with lengths of 10 cm, 15.5 cm and 23 cm. The buffer gas is Ar. The modulation frequency is 100 kHz. P_{ctrl} is 675 mW. C: concentration of C_2H_2.

Figure 6.5 Comparison of the modulation performance between two samples based on HC-PBGF and HC-ARF. The two HCFs have the same length of 23 cm, and filled with 12.5% C_2H_2 in buffer gas of Ar. (a) Phase modulation as a function of P_{ctrl} for modulation frequency of 100 kHz. (b) Frequency response with P_{ctrl} of 150 mW.

Figure 6.6 Response of the PT phase modulation with the HC-PBGF to square control pulses with pulse width of 2.5 μs.

List of Tables

List of Acronyms

2D	two-dimensional
AOM	acoustic optical modulator
ARROW	anti-resonant reflecting optical waveguide
BLS	broadband light source
BP	black phosphorus
CA	cavity-enhanced
CF	compensation fiber
CLS	classic least-squares
CTRL	control signal
DAQ	data acquisition card
DFB	distributed-feedback
DLAS	direct laser absorption spectroscopy
EDFA	erbium-doped fiber amplifier
EDL	electrical delay line
ESW	electrical switch
FDM	frequency division multiplexing
FE-PTS	fiber-enhanced photothermal spectroscopy

FG	function generator
FO-PTS	fiber optical photothermal spectroscopy
FT-FE-PTS	Fourier transform FE-PTS
FPI	Fabry-Perot interferometer
FSR	free spectral range
FT-PTS	Fourier transform photothermal spectroscopy
FWHM	full width at half maximum
GAS	gas absorption spectroscopy
GS/MS	gas chromatographic mass spectrometry
HC-ARF	hollow-core anti-resonant fiber
HC-CTF	hollow-core conjoint-tube fiber
HCF	hollow-core fiber
HC-PBGF	hollow-core photonic bandgap fiber
HPF	high-pass filter
HWHM	half width at half maximum
IC	intracavity
IL	insertion loss
LAS	laser absorption spectroscopy

LIA	lock-in amplifier
LLS	linear least-squares
LOD	limit of detection
LPF	low-pass filter
MF	microfibers
MI	modal interference
MIR	mid-infrared
MZI	Mach-Zehnder interferometer
NEC	noise equivalent concentration
NIR	near-infrared
NLLSQ	nonlinear least-squares
NTP	normal temperature and pressure
OC	optical circulator
OFM	optical fiber mirror
OPM	optical power meter
OPMA	optical-phase-modulation amplifying
OSC	oscilloscope
OSW	optical switch

p-p	peak-to-peak
PABS	photoacoustic Brillouin spectroscopy
PBG	photonic bandgap
PC	polarization controller
PD	photodetector
PLS	partial least-squares
PM	phase modulator
ppb	parts per billion
ppm	parts per million
ppt	part per trillion
PT	photothermal
PTS	photothermal spectroscopy
PZT	piezoelectric transducer
QCL	Quantum Cascade Laser
RAM	residual amplitude modulation
RF	radiofrequency
RFA	Raman fiber amplifier
RI	refractive index

RS	reference source
SC	supercontinuum source
SI	Sagnac interferometer
SMF	single-mode fiber
SMI	scanning Michelson interferometer
SNR	signal-to-noise ratio
STBI	scanning two-beam interferometer
std	standard deviation
TDLAS	tunable diode laser absorption spectroscopy
TDM	time-division multiplexing
TECF	thermally expanded core fiber
TMD	transition metal dichalcogenides
TSL	tunable semiconductor laser
VOA	variable optical attenuator
WDM	wavelength-division multiplexer
WMS	wavelength modulation spectroscopy

List of Symbols

α	absorption coefficient
$\alpha_0(v)$	absorption coefficient at the gas concentration of 100%
β	propagation constant
γ	half-linewidth
γ_D	Doppler HWHM linewidth
γ_L	Lorentzian HWHM linewidth
γ_0	Lorentzian HWHM linewidth at normal pressure and temperature
η	coupling efficiency
κ	thermal conductivity
λ	wavelength
λ_c	wavelength of the nearest transmission peak
λ_{pr}	wavelength of the probe beam
$\Delta\upsilon$	laser linewidth
π	circularity ratio
ρ	density
σ	absorption cross-section
τ_{fall}	fall time

τ_{rise}	rise time
φ_p	phase modulation
$\phi_p(t)$	phase change in time domain
$\phi(v,P,T)$	lineshape function
$\phi_L(v,P,T)$	Lorentzian lineshape function
$\phi_G(v,T)$	Gaussian lineshape function
$\phi_V(v,P,T)$	Voigt lineshape function
$\Phi_p(f_m)$	phase change in frequency domain
$a(v)$	absorption coefficient at the gas concentration of C
c	speed of light
c_2	second radiation constant
f	modulation frequency
f_{3dB}	-3dB modulation bandwidth
f_m	modulation frequency
g'	upper state statistical weight
h	Planck constant
k	angular wavenumber
k'	phase modulation coefficient

k_B	Boltzmann constant
l	absorption path length
m_d	modulation depth
n_g	number of moles of the target gas
n_{tot}	total number of moles of the gas
t	time
u_r	velocity fields in r direction
u_z	velocity fields in z direction
v	optical wavenumber
v_{pr}	wavenumber of the probe beam
Δv	modulation amplitude
$\bar{v}$	center wavenumber of the modulated laser beam
v_{mn}	wavenumber of the spectral line transition in vacuum between the lower state m and the upper state n
v_0	center wavenumber of the absorption line
w_0	mode field radius from the SMF
w_m	modulation angular frequency
w_{probe}	mode field radius of the probe beam
w_{pump}	mode field radius of the pump beam

$\overline{x_v}$	normalized center wavenumber
z_R	Rayleigh length
A_{mn}	Einstein-A coefficient of a transition
C	target gas concentration
C_P	isobaric heat capacity
E''	low state energy
H_n	the n-order harmonic coefficient
I_a	natural terrestrial isotopic abundances
$I_{abs}(x,y)$	absorbed light power per unit area in the position (x,y)
$I_{in}(x,y)$	incident light power per unit area in the position (x,y)
$I_{in}(v)$	intensity of the BLS at v
$I_p(r)$	area-normalized intensity profile
$I_{out}(v)$	intensity of the output light beam from the STBI
I_r	interference intensity of the reflected light field
ΔI_{r}	peak-to-peak modulation amplitude
$I_{res}(x,y)$	residual light power per unit area in the position (x,y)
$I_L(v)$	loss spectrum
$J_n(x)$	Bessel function of order n

M	molecular weight in atomic mass units
N_g	number of gas molecules in a unit volume
N_A	Avogadro's number
N_0	total molecular density
P	pressure
P_{abs}	absorbed beam power
$\tilde{P}_{abs}(v,t)$	instantaneous absorbed pump power
P_{ctrl}	control light power
P_g	partial pressure of the target gas
P_{in}	incident beam power
P_0	standard atmospheric pressure
$P_{out}(v)$	output spectrum
P_{pump}	power of the pump beam
$\tilde{P}_{pump}(v,t)$	instantaneous power
Q	heat generation
$S(T)$	line strength per molecule at temperature T
$S_{mn}(T)$	line strength per molecule of the transition between the lower state m and the upper state n
ΔT	temperature change

T	temperature
T_{amb}	ambient temperature
T_0	initial temperature
T_s	standard temperature
V	volume
$\tilde{V}$	velocity of the optical path difference
$W(t)$	modulation waveform of the pump
X_g	mole fraction of the target gas

Chapter 1 Introduction

1.1 Literature review

High-sensitivity gas sensing has triggered widespread interests in recent years, due to the increased performance demands for environment protection, health care diagnosis and industrial security application [1-3]. Many traditional gas sensing techniques have been investigated based on non-optical detection, such as gas chromatographic mass spectrometry (GS/MS) [4-6], semiconductor method [7-9], and electrochemical method [10-12].

GS/MS firstly separates the gas mixture into different components based on gas chromatography by introducing the mixture into a long column filled with special stationary phase material. The material makes different gas components pass the column at different rates. Then GS/MS successively analyzes different gas components and determines the species and concentration based on mass spectrometry, for example, by ionizing one gas component into ions with different mass-to-charge ratios, separating the ions under electric or magnetic field, and identifying different ions through the plots of the mass spectrum. This technique has the advantage of high sensitivity, but is bulky, time consuming and expensive, making it difficult for transferring and field applications [6].

Semiconductor gas sensors are based on the oxidation-reduction reaction between the gas and the special sensing material on the surface of the semiconductor, with the physical parameters (e.g. conductivity) of the sensing material changed and converted into measurable electrical parameters (e.g. resistance). Electrochemical method is based on the oxidation or reduction reaction of the target gas at an electrode in contact with an electrolyte, with the gas concentration determined by measuring the resulting current.

The semiconductor and electrochemical techniques can achieve a small size, but have low selectivity and short service life [13-14].

Compared to the non-optical techniques, optical technologies provide a new approach for gas sensing. Among the optical gas sensing technologies, laser absorption spectroscopy (LAS) provides high selectivity and sensitivity [15-17]. In this method, gas absorbs photons from a laser when the laser wavelength matches the absorption line of the target gas molecule, with different absorption ratio of the laser power for different concentration of the target gas according to the Beer-Lambert low [18].

As a common LAS technique, direct laser absorption spectroscopy (DLAS) determines the gas concentration by measuring the attenuation of the input laser power, but it suffers from any noise introduced by the laser source, the system or ambient environment [19]. Traditional LAS based on free-space optics increases absorption by increasing the effective absorption length (i.e., the light-gas interaction length) with multiple-pass cells or cavity enhanced absorption spectroscopy, but the system is bulky and its performance may be difficult to maintain for long-term use in the real situation due to the requirements of punctilious calibrations or complicated locking techniques [15].

Compared to free-space optical methods, fiber-optic technologies can realize a compact, flexible and convenient configuration [20-21]. By use of hollow-core fibers (HCFs), light-gas interaction is enhanced due to stronger light confinement and longer interaction distance [22-23]. Using HCFs as the gas cell also has the advantages of low insertion loss, wide bandwidth, immunity to electromagnetic interference, high photodamage threshold and remote sensing. Connecting of HCFs and single-mode fibers (SMFs) has been being studied to pursue a lower insertion loss through fusion splicing, with a promising value of 0.3 dB reported so far, which shows excellent integration into an overall optical fiber system [24-26]. Besides, the center wavelength

of a HCF is reported to cover from visible light to near-infrared light, with bandwidth over many hundreds of nanometers. The center wavelength can also be shifted to cover any desired wavelength range under further design [27]. Gas can also be filled into the HCFs by fabricating holes on the HCFs to speed up the gas diffusion process by laser processing [28].

In addition to enhance the absorption by HCFs, the sensitivity in LAS can also be improved by reducing the noise with wavelength modulation spectroscopy (WMS) to detect the absorption signal at a high frequency with low noise level [29]. By combining WMS with tunable diode lasers, tunable diode laser absorption spectroscopy (TDLAS) tunes the laser wavelength repeatedly across the absorption line of the target gas, with harmonic components of the signal demodulated by a lock-in amplifier [30]. TDLAS with long HCFs greatly increases the sensitivity by enhancing the absorption and reducing the noise at the same time [31-32]. However, because the modulated beam is detected directly by a photodetector, this technique may suffer from residual amplitude modulation (RAM) noise, interference fringe noise and mode interference noise, causing signal distortion and decreasing the detection accuracy and sensitivity [33-35].

Instead of detecting the absorbed beam (also called the pump beam), photothermal spectroscopy (PTS) detects the indirect effect, i.e., photothermal (PT) effect [36-37]. Gas absorption of the pump beam generates heat via PT effect and modulates the RI of the gas medium, which is detected by measuring the phase modulation of a probe beam propagating through the medium. PTS is a sensitive technique. Because the probe beam is not modulated, so the system is free from RAM noise. PTS may use a pump laser with sufficiently high power to increase the PT phase signal without additional noise or power saturation effect in terms of the probe beam. Early PTS systems use free-space optics, which are bulky and complex to construct, with the detection sensitivity limited by the low efficiency of PT phase modulation and large noise at low modulation frequencies [38].

PTS with HCFs enables efficient PT phase modulation at frequencies up to tens of kHz, which ensures gas detection with high signal-to-noise ratio (SNR). Jin et al. proposed all-fiber PTS gas sensors the first time in 2015, by using a 10-m hollow-core photonic bandgap (HC-PBGF) and demodulating the PTS phase modulation through a Mach-Zehnder interferometer (MZI), and achieved noise equivalent concentration (NEC) of 2 parts per billion (ppb) and large dynamic range of 5.3×10^5 for acetylene [39]. The response time, however, was about 7200s due to the long fiber length. Stabilization through servo control was also needed due to the environmental physical variations. In 2016, Lin et al. used a 0.62-m HC-PBGF to achieve NEC of 3.3 parts per million (ppm) for acetylene detection based on pulsed PTS, through a Sagnac interferometer (SI) without stabilization, and Yang et al. applied 0.3-m HC-PBGF to achieve NEC of 1 ppm through an MZI with stabilization [28, 39-40]. The response time was reduced, but still a bit long, and the detection limit was poorer. In the same year, a 0.02-m HC-PBGF was applied by Yang et al. to achieve NEC of 117 ppb and the response time of 19 s through a Fabry-Perot interferometer (FPI) without stabilization [41]. In 2017, Lin et al. used a 1.1-m HC-PBGF to achieve NEC of 18 ppb through a SI [42]. In the same year, Qi et al. used a 0.0012-m Nanofiber to achieve NEC of 600 ppb through an MZI with stabilization [43]. In 2018, Zhao et al. applied a 0.62-m HC-PBGF to achieve NEC of 176 ppb based on intracavity PTS without stabilization [44]. In 2019, Tan et al. used a 0.062-m HC-PBGF to achieve NEC of 126 ppb and response time of 60 s based on a cavity-enhanced FPI with stabilization [45]. In 2020, Zhao et al. applied a 4.67-m hollow-core anti-resonant fiber (HC-ARF) to achieve NEC of 15 part per trillion (ppt), dynamic range of 2×10^7 and response time of 44 s through mode interference PTS without stabilization [46]. In the same year, a 0.055-m HC-ARF was used by Bao et, al. to achieve NEC of 2.3 ppb, dynamic range of 4.3×10^6 and response time of 52 s through an FPI with stabilization [47]. In 2022, Bao et, al. applied a 0.1-m HC-ARF to achieve NEC of 2.7 ppt through optical-phase-modulation amplifying PTS with stabilization [48]. Combining PTS with HCFs enables us to build a gas sensing system with

advantages of flexibility, immunity to electromagnetic interference, high reliability and capability of distributed and remote gas sensing.

PTS with HCFs also enables multi-component gas detection with a single HCF gas cell. Liu et al. demonstrated multicomponent trace gas detection with a single HCF gas cell and multiple distributed-feedback (DFB) pump lasers based on time-division multiplexing, achieving the limit of detection (LOD) in terms of NEC of 24.2 ppb for methane, 11.6 ppb for acetylene and 46.1 ppb for ammonia [49]. Chen et al. used three pump lasers, i.e., a 1390-nm DFB for H_2O, a 2004-nm DFB for CO_2, and a 4600-nm DFB Quantum Cascade Laser (QCL) for CO, which were modulated at different frequencies and launched into the same HCF gas cell to achieve the LOD of 222 ppb for H_2O, 1.5 ppb for CO_2 and 0.6 ppb for CO [50].

1.2 Research motivation

Real-time gas sensing is very important from daily life to the industrial and agricultural production. Non-invasive medical diagnostic according to biomarkers from human breath needs real-time detection of the gas composition, considering that an adult breathes for 12-20 times per minutes, and physiological or pathophysiological effects also induce the quick variations of gas concentration [51-53]. Some chronic diseases caused by noxious gas are also very common today, which can be found in inferior sofas, colored walls, and vehicle exhaust et al., and because of safety concerns, exposure levels below 1ppm are proposed by many institutes [54]. Gas recycling in space stations also needs real-time detection of the gas concentration to avoid pollution and loss of control, where portable and real-time gas sensors are in demands [55]. Fault gas detection in energy storage systems, e.g., detection of Li-ion battery failure, may need a small sensor to be in contact with a small amount of the target gas [56].

What's more, for multi-component gas sensing, traditional fiber optical PTS (FO-PTS)

system normally utilizes an additional laser as the probe beam in addition to the pump lasers tuned to the specific absorption lines of the target gas species. And as the number of the target gas species increases, another pump lasers are normally required, leading to a bulky system for multi-component gas sensing because of a large number of the lasers.

Meanwhile, during the research process of the sensors, we found that phase modulation based on FO-PTS with a fixed gas concentration was rarely researched, which can be applied as phase modulators. The absorption line of the filled gas is very narrow and doesn't bother with other wavelengths, which allows the phase modulators to be applied in a wide spectrum range, particularly for ultraviolet and midinfrared bands, which is challenging for traditional phase modulators with solid materials.

In the first part, we report a miniature optical fiber PT gas sensor with fast response and large dynamic range. The sensing region is an air gap formed between the cleaved ends of two SMFs. Theoretical formulations of PT phase modulation and interferometric phase detection are presented. Numerical simulation and experimental investigation are carried out to optimize the system parameters to maximize the PT signal. A gas sensor with an air gap of 130 μm demonstrates a NEC of 45 ppb and dynamic range of 2×10^7 for acetylene detection. The sensor is simple to construct and may be used for real-time gas detection in a confined space.

In the second part, we present a two-component gas sensor based on FO-PTS with an alternating pump and probe technique. The proposed approach uses two DFB lasers for the detection of acetylene and methane. These two lasers act alternatively as the pump and probe beams respectively for the two gas components via time-division multiplexing. With a centimeter-long hollow-core conjoint-tube fiber (HC-CTF), NEC of 400 ppb and 130 ppb are demonstrated for methane and acetylene detection, respectively.

In the third part, we demonstrate a fiber-enhanced gas sensor based on the Fourier transform photothermal spectroscopy (FT-PTS) with an HCF. The pump beam is generated by a broadband light source passing through a scanning two-beam interferometer with the light intensity modulated at different frequencies for different wavenumbers. The PTS technique is used to demodulate the phase modulation. A ten-centimeter-long HCF demonstrates single-component gas detection of acetylene and carbon dioxide with NECs of ~465 ppb and ~457 ppm, respectively. The system is also used to demonstrate the two-component gas detection of acetylene and carbon dioxide.

In the fourth part, we explore the FO-PTS with HCFs for the application of phase modulators. We investigate the effect of varying gas (C_2H_2) concentration, buffer gas, HCF length and transverse microstructure on the PT phase modulation, which enables better understanding of the modulation process to optimize the performance of the phase modulators.

1.3 Thesis outline

The structure of the thesis is the following:

Chapter 1 reviews the research background of HCF-based PTS gas sensors. The LAS with HCFs and WMS is introduced. The current development of PTS with HCFs for single-component and multi-component gas sensing is reviewed.

Chapter 2 describes the principle of gas absorption spectroscopy in terms of Beer-Lambert law and absorption line shape functions, and wavelength modulation spectroscopy in terms of the modulation coefficients, and hollow-core fiber in terms of HC-PBGF and HC-ARF. The basic of photothermal spectroscopy with HCFs is presented.

Chapter 3 demonstrates a miniature optical fiber gas sensor based on PTS with fast

response and large dynamic range. The sensing head is an air gap formed between the cleaved ends of two SMFs. Theoretical formulations of photothermal phase modulation and interferometric phase detection are presented. Numerical simulation and experimental investigation are carried out to optimize the system parameters to maximize the photothermal signal.

Chapter 4 presents an alternating pump and probe technique, which utilizes two distributed feedback lasers as pump and probe beams alternatively for two gas components to facilitate photothermal phase modulation and detection through time-division multiplexing.

Chapter 5 studies fiber-enhanced Fourier-transform PTS with HCF for multi-component gas sensing. The pump beam is generated by a broadband light source (BLS) passing through a scanning two-beam interferometer with the light intensity modulated at different frequencies for different wavenumbers. The sampled interferogram is Fourier-transformed into the PT spectrum for gas identification and concentration detection.

Chapter 6 explores the modulation performance of phase modulators based on PTS with HCFs filled with acetylene. The effects of varying gas concentration, buffer gas, length and transverse microstructure of the HCFs on the performance of the phase modulators are investigated.

Chapter 7 summarizes the thesis and suggests the future research directions.

1.4 References

1. P. Laj, J. Klausen, M. Bilde, C. Plaß-Duelmer, G. Pappalardo, C. Clerbaux, U. Baltensperger, J. Hjorth, D. Simpson, S. Reimann, P.-F. Coheur, A. Richter, M. De Mazière, Y. Rudich, G. McFiggans, K. Torseth, A. Wiedensohler, S. Morin, M. Schulz,

J.D. Allan, J.-L. Attié, I. Barnes, W. Birmili, J.P. Cammas, J. Dommen, H.-P. Dorn, D. Fowler, S. Fuzzi, M. Glasius, C. Granier, M. Hermann, I.S.A. Isaksen, S. Kinne, I. Koren, F. Madonna, M. Maione, A. Massling, O. Moehler, L. Mona, P.S. Monks, D. Müller, T. Müller, J. Orphal, V.-H. Peuch, F. Stratmann, D. Tanré, G. Tyndall, A. Abo Riziq, M. Van Roozendael, P. Villani, B. Wehner, H. Wex, and A.A. Zardini, "Measuring atmospheric composition change. Atmos," Environ. 43, 5351–5414 (2009).

2. C. Liu, and L. Xu, "Laser absorption spectroscopy for combustion diagnosis in reactive flows: a review," Applied Spectroscopy Reviews. 54, 1–44 (2019).

3. D. Smith, and P. Španěl, "The challenge of breath analysis for clinical diagnosis and therapeutic monitoring," Analyst. 132, 390–396 (2007).

4. A. Pittet, A. Périsset, and J.-M. Oberson, "Trace level determination of acrylamide in cerealbased foods by gas chromatography–mass spectrometry," Journal of Chromatography A. 1035, 123-130 (2004).

5. O. David Sparkman, Z.E. Penton, and F.G. Kitson, "Gas chromatography and mass spectrometry: a practical guide (second edition)," Academic Press (2011).

6. R.A. Hites, "Development of gas chromatographic mass spectrometry," Analytical chemistry. 88, 6955-6961 (2016).

7. S.R. Morrison, "Semiconductor gas sensors," Sensors and Actuators. 2, 329-341, (1981).

8. N. Yamazoe, "New approaches for improving semiconductor gas sensors," Sensors and actuators B: Chemical. 5, 7-19 (1991).

9. M.V. Nikolic, V. Milovanovic, Z.Z. Vasiljevic, and Z. Stamenkovic, "Semiconductor gas sensors: materials, technology, design, and application," Sensors. 20, 1-30 (2020).

10. M.J. Tierney, and H.O.L. Kim, “Electrochemical gas sensor with extremely fast response times,” Analytical Chemistry. 65, 3435-3440 (1993).

11. L.P. Martin, A.-Q. Pham, and R.S. Glass, “Electrochemical hydrogen sensor for safety monitoring,” Solid State Ionics. 175, 527-530 (2004).

12. J.W. Fergus, “Materials for high temperature electrochemical NOx gas sensors,” Sensors and Actuators B: Chemical. 121, 652-663 (2007).

13. S. Ghosh, M.S. Ilango, C.S. Prajapati, and N. Bhat, “Reduction of humidity effect in WO3 thin film-based NO2 sensor using physiochemical optimization,” Cryst. Res.Technol. 56, 1-10 (2021).

14. X. Pang, M.D. Shaw, S. Gillot, and A.C. Lewis, “The impacts of water vapour and copollutants on the performance of electrochemical gas sensors used for air quality monitoring,” Sens. Actuators B: Chem. 266, 674–684 (2018).

15. X. Liu, S. Cheng, H. Liu, S. Hu, D. Zhang, and H. Ning, “A survey on gas sensing technology,” Sensors. 12, 9635–9665 (2012).

16. J. Hodgkinson, and R. P. Tatam, “Optical gas sensing: a review,” Measurement Science and Technology. 24, 1-59 (2012).

17. Z. Wang, P. Fu, and X. Chao, “Laser absorption sensing systems: challenges, modeling, and design optimization,” Applied Sciences. 9, 1-27 (2019).

18. M. Hollas, "Modern Spectroscopy (fourth edition)," England: John Wiley & Sons (2004).

19. X. Gao, H. Fan, T. Huang, X. Wang, J. Bao, X. Li, W. Huang, and W. Zhang, “Natural gas pipeline leak detector based on NIR diode laser absorption spectroscopy,” Spectrochimica Acta Part A Mol. Biomol. Spectrosc. 65, 133–138 (2006).

20. J. Dakin, and B. Culshaw, “Optical fiber sensors, Volume 1: principles and components,” Boston, MA, Artech House (1988).

21. B. Lee, “Review of the present status of optical fiber sensors,” Optical fiber technology. 9, 57-79 (2003).

22. R. Cregan, B. Mangan, J. Knight, T. Birks, P. S. J. Russell, P. Roberts, and D. Allan, “Single-mode photonic band gap guidance of light in air,” Science. 285, 1537-1539 (1999).

23. Y. Hoo, W. Jin, H. Ho, J. Ju, and D. Wang, “Gas diffusion measurement using hollow-core photonic bandgap fiber,” Sensors and Actuators B: Chemical. 105, 183-186 (2005).

24. L. Xiao, W. Jin. And M.S. Demokan, “Fusion splicing small-core photonic crystal fibers and single-mode fibers by repeated arc discharges,” Opt Lett. 32, 115-117 (2007).

25. S. Gao, Y. Wang, C. Tian, and P. Wang, “Splice loss optimization of a photonic bandgap fiber via a high v-number fiber,” IEEE photonics technology letters. 26, 2134-2137 (2014).

26. M. Komanec, D. Suslov, S. Zvánovec, Y. Chen, T. Bradley, S.R. Sandoghchi, E.R. Numkam Fokoua, G.T. Jasion, M.N. Petrovich, F. Poletti, D.J. Richardson, and R. Slavík, “Low-loss and low-back-reflection hollow-core to standard fiber interconnection,” IEEE photonics technology letters. 31, 723-726 (2019).

27. P. Roberts, F. Couny, H. Sabert, B. Mangan, D. Williams, L. Farr, M. Mason, A. Tomlinson, T. Birks, J. Knight, and P.S. Russell, “Ultimate low loss of hollow-core photonic crystal fibres,” Opt Expres. 13, 236-244 (2005).

28. F. Yang, W. Jin, Y. Lin, C. Wang, H.L. Ho, and Y. Tan, “Hollow-core microstructured optical fiber gas Sensors,” Journal of Lightwave Technology. 35, 3413-

3424 (2017).

29. P. Kluczynski, J. Gustafsson, Å.M. Lindberg, and O. Axner, “Wavelength modulation absorption spectrometry - an extensive scrutiny of the generation of signals,” Spectrochim. Acta B At. Spectrosc. 56, 1277–1354 (2001).

30. P. Werle, F. Slemr, K. Maurer, R. Kormann, R. Mücke, and B. Jänker, “Near-and mid-infrared laser-optical sensors for gas analysis,” Optics and lasers in engineering. 37, 101-114 (2002).

31. F. Magalhaes, J. Carvalho, L. Ferreira, F. Araújo, and J. Santos, “Methane detection system based on wavelength modulation spectroscopy and hollow-core fibres,” SENSORS, 2008 IEEE, Lecce, Italy. 1277-1280 (2008).

32. Y. L. Hoo, S. Liu, H. L. Ho, and W. Jin, “Fast response microstructured optical fiber methane sensor with multiple side-openings,” IEEE Photonics Technology Letters. 22, 296-298 (2010).

33. A.L. Chakraborty, K. Ruxton, W. Johnstone, M. Lengden, and K. Duffin, “Elimination of residual amplitude modulation in tunable diode laser wavelength modulation spectroscopy using an optical fiber delay line,” Opt. Express. 17, 9602-9607 (2009).

34. D.S. Bomse, A.C. Stanton, and J.A. Silver, “Frequency modulation and wavelength modulation spectroscopies: comparison of experimental methods using a lead-salt diode laser,” Applied Optics. 31, 718-731 (1992).

35. L. Hu, C. Zheng, D. Yao, D. Yu, Z. Liu, J. Zheng, Y. Wang, and F.K. Tittel, “A hollow-core photonic band-gap fiber based methane sensor system capable of reduced mode interference noise,” Infrared Physics & Technology. 97, 101-107 (2019).

36. C.C. Davis, and S.J. Petuchowski, “Phase fluctuation optical heterodyne

spectroscopy of gases," Appl. Opt. 20, 2539-2554 (1981).

37. S.E. Bialkowski, N.G.C. Astrath, and M.A. Proskurnin, "Photothermal spectroscopy methods (2nd ed)," Wiley (2019).

38. A.J. Campillo, S.J. Petuchowski, C.C. Davis, and H.B. Lin, "Fabry-perot photothermal trace detection," Appl. Phys. Lett. 41, 327–329 (1982).

39. W. Jin, Y. Cao, F. Yang, and H. L. Ho, "Ultra-sensitive all-fibre photothermal spectroscopy with large dynamic range," Nat. Commun. 6, 1-8 (2015).

40. Y. Lin, W. Jin, F. Yang, J. Ma, C. Wang, H. L. Ho, and Y. Liu, "Pulsed photothermal interferometry for spectroscopic gas detection with hollow-core optical fibre," Sci. Rep. 6, 1-12 (2016).

41. F. Yang, Y. Tan, W. Jin, Y. Lin, Y. Qi, and H.L. Ho, "Hollow-core fiber Fabry–Perot photothermal gas sensor," Opt. Lett. 41, 3025-3028 (2016).

42. Y. Lin, W. Jin, F. Yang, Y. Tan, and H. L. Ho, "Performance optimization of hollow-core fiber photothermal gas sensors," Opt. Lett. 42, 4712–4715 (2017).

43. Y. Qi, F. Yang, Y. Lin, W. Jin, and H.L. Ho, "Nanowaveguide enhanced photothermal interferometry spectroscopy," Journal of Lightwave Technology. 35, 5267-5275 (2017).

44. Y. Zhao, W. Jin, Y. Lin, F. Yang, and H.L. Ho, "All-fiber gas sensor with intracavity photothermal spectroscopy," Opt. Lett. 43, 1566-1569 (2018).

45. Y. Tan, W. Jin, F. Yang, Y. Jiang, and H.L. Ho, "Cavity-enhanced photothermal gas detection with a hollow fiber Fabry-Perot absorption cell," Journal of Lightwave Technology. 37, 4222-4228 (2019).

46. P. Zhao, Y. Zhao, H. Bao, H.L. Ho, W. Jin, S. Fan, S. Gao, Y. Wang, and P. Wang, "Mode-phase-difference photothermal spectroscopy for gas detection with an anti-resonant hollow-core optical fiber," Nat Commun. 11, 847 (2020).

47. H. Bao, Y. Hong, W. Jin, H.L. Ho, C. Wang, S. Gao, Y. Wang, and P. Wang, "Modeling and performance evaluation of in-line Fabry-Perot photothermal gas sensors with hollow-core optical fibers," Opt. Express. 28, 5423–5435 (2020).

48. H. Bao, W. Jin, Y. Hong, H.L. Ho, S. Gao, and Y. Wang, "Phase-modulation-amplifying hollow-core fiber photothermal interferometry for ultrasensitive gas sensing," Journal of Lightwave Technology. 40, 313-322 (2022).

49. F. Liu, H.H. Bao, H.L. Ho, W. Jin, S.F. Gao, and Y.Y. Wang, "Multicomponent trace gas detection with hollow-core fiber photothermal interferometry and time-division multiplexing," Optics Express. 29, 43445-43453 (2021).

50. F. Chen, S. Jiang, H.L. Ho, S. Gao, and Y. Wang, "Frequency-division-multiplexed multicomponent gas sensing with photothermal spectroscopy and a single NIR/MIR fiber-optic gas cell," Anal. Chem. 94, 13473–13480 (2022).

51. I.R. White, K.A. Willis, C. Whyte, R. Cordell, R.S. Blake, A.J. Wardlaw, S. Rao, J. Grigg, A.M. Ellis, and P.S. Monks, "Real-time multi-marker measurement of organic compounds in human breath: towards fingerprinting breath," J. Breath Res. 7, 1-11 (2013).

52. P. Trefz, M. Schmidt, P. Oertel, J. Obermeier, B. Brock, S. Kamysek, J. Dunkl, R. Zimmermann, J.K. Schubert, and W. Miekisch, "Continuous real time breath gas monitoring in the clinical environment by proton-transfer-reaction-time-of-flight-mass spectrometry," Analytical chemistry. 85, 10321–10329 (2013).

53. P. Trefz, G. Pugliese, B. Brock, Schubert, J.K. Schubert, and W. Miekisch, "Effects

of elevated oxygen levels on VOC analysis by means of PTR-ToF-MS," J. Breath Res. 13, 1-11 (2019).

54. J.D. Jeffers, C.B. Roller, and K. Namjou, "Real-time diode laser measurements of vapor-phase benzene," Analytical chemistry. 76, 424–432 (2004).

55. D.G. Lancaster, D. Richter, R.F. Curl, and F.K. Tittel, "Real-time measurements of trace gases using a compact difference-frequency-based sensor operating at 3.5 μm," Applied physics. B, Lasers and optics. 67, 339–345 (1998).

56. T. Cai, P. Valecha, V. Tran, B. Engle, A. Stefanopoulou, and J. Siegel, "Detection of Li-ion battery failure and venting with Carbon Dioxide sensors," eTransportation. 7, 1-11 (2021).

Chapter 2 Background knowledge

In this chapter, we review the basic principles of gas absorption spectroscopy (GAS), wavelength modulation spectroscopy (WMS), hollow-core fibers (HCFs) and photothermal spectroscopy (PTS) with HCFs.

2.1 Gas absorption spectroscopy

2.1.1 Beer-Lambert law

Figure 2.1 shows the schematic of gas absorption of an incident beam. When a light beam with the intensity of $I_{in}(x,y)$, i.e., the power per unit area in the position (x,y), is incident into the gas region along the z direction, the residual beam intensity according to the Beer-Lambert law can be expressed as [1]

$$I_{res}(x,y) = I_{in}(x,y)e^{-\sigma N_g l} \tag{2.1}$$

where σ is the absorption cross-section of the absorptive gas, N_g is the number of the gas molecules in a unit volume, and l is the absorption path length. Therefore, the Beer-Lambert law for the absorbed beam intensity is

$$I_{abs}(x,y) = I_{in}(x,y)(1 - e^{-\sigma N_g l}) \tag{2.2}$$

To integrate the (2.2) over the x-y plane, we can get the Beer-Lambert law for the absorbed power:

$$P_{abs} = P_{in}(1 - e^{-\sigma N_g l}) \tag{2.3}$$

where P_{in} is the incident beam power and equal to the integration of $I_{in}(x,y)$ over the x-y plane.

Figure 2.1 Schematic of gas absorption.

Figure 2.2 depicts the parameters of the absorption cross-section of a gas molecule. The absorption cross-section σ of the target gas molecule can be expressed as

$$\sigma = S(T)\phi(v, P, T) \tag{2.4}$$

where v is the optical wavenumber, P is the gas pressure, T is the temperature, $S(T)$ is the line strength per molecule, and $\phi(v, P, T)$ is the lineshape function and is normalized with $\int_{-\infty}^{\infty} \phi(v, P, T)dv = 1$.

On the assumption that the gas medium is an ideal gas, the number of the gas molecules in a unit volume, N_g, i.e., the number density of the target gas, can be calculated as

$$N_g = N_A \cdot \frac{n_g}{V} = \frac{P}{T} \cdot \frac{n_g}{n_{tot}} \cdot \frac{N_A}{R} \cdot \frac{n_{tot}RT}{PV} = \frac{PX_g}{k_B T} = \frac{P_g}{k_B T} \tag{2.5}$$

where N_A is the Avogadro's number, n_g is the number of moles of the target gas, V is the volume, X_g is the mole fraction of the target gas and equal to n_g/n_{tot} with n_{tot} the total number of moles of the gas, $k_B = R/N_A$ is the Boltzmann constant with R the ideal gas constant, and P_g is the partial pressure of the target gas and equal to PX_g. Therefore, we can write the (2.3) as

$$P_{abs} = P_{in}(1 - e^{-\frac{S(T)\phi(v,P,T)P_g l}{k_B T}}) \tag{2.6}$$

When we introduce the absorption coefficient α, the Beer-Lambert law may be written as

$$P_{abs} = P_{in}(1 - e^{-\alpha C l}) \tag{2.7}$$

where C is the target gas concentration and equal to N_g/N_0 with N_0 the total molecular density and equal to P/k_BT, and α is the absorption cross section σ multiplied by N_0 as

$$\alpha(v,P,T) = N_0\,\sigma \tag{2.8}$$

At normal temperature and pressure (NTP) with P_0=1 atm or 101.325 kPa and T_s=293.15 K, N_0 is equal to $P_0/k_BT_s \cong 2.4794 \times 10^{25} m^{-3}$. It should be noted that (2.7) can be deduced by combining (2.6) and (2.8). Hence the gas absorpton can be calculated by using the equivalent forms of the Beer-Lambert law of (2.3), (2.6) and (2.7).

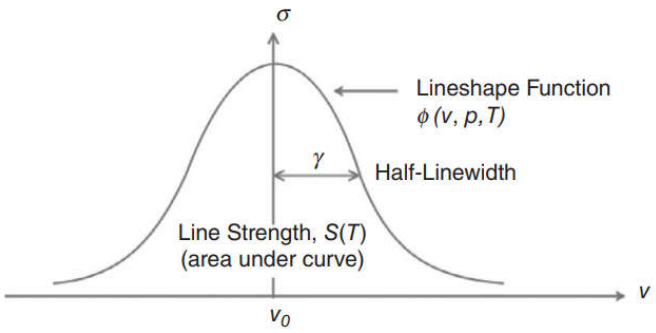

Figure 2.2 Schematic of the parameters of a typical absorption cross-section of a gas molecule [1].

2.1.2 Absorption line shape functions

The molecular absorption cross-section has a certain width as shown in Fig. 2.2, due to the spectral broadening including two kinds, i.e., homogeneous and inhomogeneous broadenings. According to the different broadening mechanisms, the absorption lineshape can be classified into three types of Lorentzian, Gaussian, and Voigt lineshapes [1-4].

Homogeneous broadening comes from natural broadening due to photon absorption

under the inherent uncertainty principle, or collision broadening due to the collision of gas molecules with each other. Its absorption cross-section can be expressed by a Lorentzian lineshape as

$$\phi_L(v, P, T) = \frac{1}{\pi\gamma_L} \frac{1}{1+\left(\frac{v-v_0}{\gamma_L}\right)^2} \tag{2.9}$$

where γ_L is the linewidth, i.e., half width at half maximum (HWHM), and v_0 is the center of the absorption line. γ_L is dependent on the pressure and temperature and may be expressed as

$$\gamma_L = \gamma_0 \frac{PT_s^n}{P_0 T^n} \tag{2.10}$$

where γ_0 is the linewidth at NTP, n is a factor generally between 0.5~1, with 1 for soft collisions and 0.5 for hard ones.

For inhomogeneous broadening, i.e., Doppler broadening, from the random thermal motion of gas molecules, the absorption cross-section can be expressed by a Gaussian lineshape as

$$\phi_G(v, T) = \frac{1}{\sqrt{\pi}\gamma_D} e^{-\left(\frac{v-v_0}{\gamma_D}\right)^2} \tag{2.11}$$

where γ_D is the half-linewidth at Doppler 1/e and expressed as

$$\gamma_D = v_0 \sqrt{\frac{2k_B T}{M}} \tag{2.12}$$

where M is the molecular weight in atomic mass units.

From (2.10) and (2.12), the linewidth of the homogeneous broadening with the Lorentzian lineshape increases as P/T^n increases, whereas that of the inhomogeneous broadening with the Gaussian lineshape is dependent only on T and increases as T

increases. At NTP, the homogeneous broadening is typically dominant over the inhomogeneous broadening and thus the lineshape is Lorentzian. As the pressure drops and/or the temperature rises, the homogeneous and inhomogeneous broadenings may be comparable, and thus the absorption lineshape may be a convolution of the normalized Gaussian and Lorentzian lineshapes, also called a Voigt lineshape and may be expressed as

$$\phi_V(v,P,T) = \frac{\gamma_L}{\pi^{\frac{3}{2}}\gamma_D^2}\int_{-\infty}^{\infty}\frac{e^{-x^2}}{\left(\frac{\gamma_L}{\gamma_D}\right)^2+\left(\frac{v-v_0}{\gamma_D}-x\right)^2}dx \tag{2.13}$$

where x in the integration means the wavenumber.

The line strength per molecule $S(T)$ of an absorption transition is dependent on the population in the lower quantum state and the transition probability between the lower state m and the upper state n, and can be expressed as [5-6]

$$S_{mn}(T) = I_a\frac{A_{mn}}{8\pi c v_{mn}^2}\frac{g' e^{-\frac{c_2 E''}{T}}\left(1-e^{-\frac{c_2 v_{mn}}{T}}\right)}{Q(T)} \tag{2.14}$$

where I_a is the natural terrestrial isotopic abundances, A_{mn} is the Einstein-A coefficient of a transition and independent of temperature and isotopologue abundance, c is the speed of light, v_{mn} is the wavenumber of the spectral line transition in vacuum between the lower state m and the upper state n, g' is the upper state statistical weight, c_2 is the second radiation constant and equal to hc/k_B with h the Planck constant, E'' is the low state energy, and $Q(T)$ is the total internal partition sum at temperature T. $S_{mn}(T)$ can be retrieved from the HITRAN database [7]. The absorption coefficient α can be calculated by combining (2.4), (2.8), (2.9), (2.11), (2.13), (2.14), with the related coefficients retrieved from the HITRAN database. As an example, Figure 2.3 depicts the absorption spectra of 0.02% acetylene (C_2H_2), 20% carbon dioxide (CO_2), 0.1% ammonia (NH_3) and 25% water (H_2O) in the wavelength

range from 1520 nm to 1620 nm.

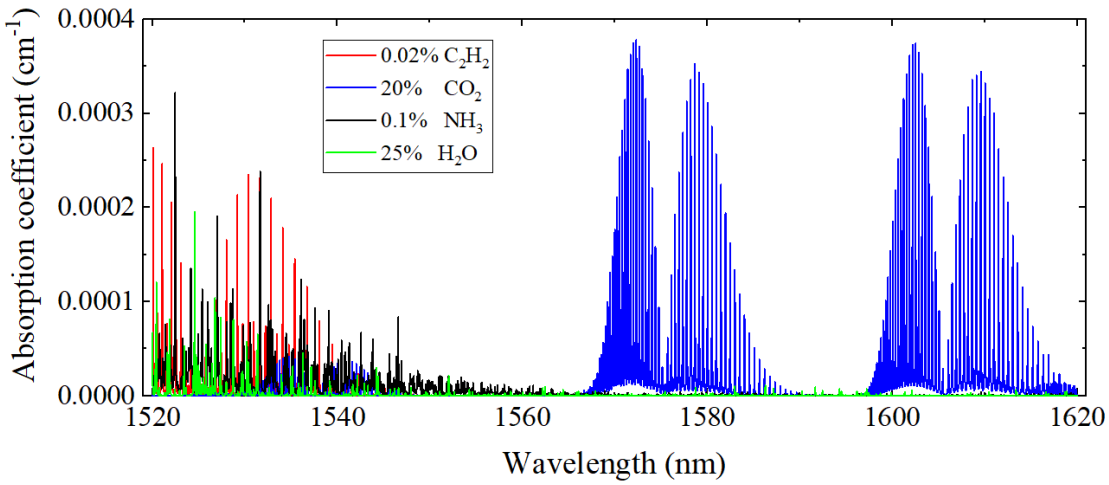

Figure 2.3 Calculated absorption coefficient of 0.02% C_2H_2, 20% CO_2, 0.1% NH_3 and 25% H_2O based on the HITRAN database.

2.2 Wavelength modulation spectroscopy

WMS is a useful technique to improve the signal-to-noise radio by detecting the absorption signal at a high frequency with low noise level [8]. This technique modulates the wavenumber of the laser beam sinusoidally at a high frequency and sweeps it around the absorption line of the target gas. For the absorption line with a Lorentzian lineshape at NTP, the absorption coefficient $a(v)$ for the target gas with the concentration of C can be expressed from (2.4), (2.8) and (2.9) as

$$a(v) = C\alpha(v) = CN_0\,\sigma(v) = C\frac{N_0 S}{\pi\gamma_L}\frac{1}{1+\left(\frac{v-v_0}{\gamma_L}\right)^2} = C\alpha_0\frac{1}{1+\left(\frac{v-v_0}{\gamma_L}\right)^2} \tag{2.15}$$

where $\alpha_0(v)$ is the absorption coefficient at the gas concentration of 100%.

When sinusoidally modulated, the wavenumber v can be expressed as

$$v = \bar{v} + \Delta v cos(w_m t) \tag{2.16}$$

where $\bar{v}$ is the center wavenumber of the modulated laser beam, Δv is the modulation amplitude, w_m is the modulation angular frequency, and t is the time. Let

$$\frac{v-v_0}{\gamma_L} = \frac{\bar{v}+\Delta v cos(w_m t)-v_0}{\gamma_L} = \frac{\bar{v}-v_0}{\gamma_L} + \frac{\Delta v}{\gamma_L} cos(w_m t) = \overline{x_v} + m_d cos(w_m t) = x_v \qquad (2.17)$$

where $\overline{x_v} = \frac{\bar{v}-v_0}{\gamma_L}$ is the normalized center wavenumber and $m_d = \frac{\Delta v}{\gamma_L}$ is the modulation depth. Hence the absorption coefficient $a(v)$ by WMS can be further expressed as [9]

$$a(x_v) = C\alpha_0 \frac{1}{1+x_v^2} = C\alpha_0 \sum_{n=0}^{\infty} H_n(\overline{x_v}) \cos(n w_m t) \qquad (2.16)$$

where

$$H_n(\overline{x_v}) = \frac{1}{2} i^n \varepsilon_n \int_{-\infty}^{+\infty} e^{-|y|} e^{i\overline{x_v} y} J_n(m_d y) dy = \frac{1}{2} i^n \varepsilon_n \frac{1}{m_d^n} \frac{\left[\sqrt{(1-i\overline{x_v})^2+m_d^2}-1+i\overline{x_v}\right]^n}{\sqrt{(1-i\overline{x_v})^2+m_d^2}} + c.c. \qquad (2.17)$$

where $\varepsilon_0 = 1$, $\varepsilon_n = 2$ for $n = 1, 2, ...$, $J_n(x)$ is the Bessel function of order n, and $c.c.$ is the complex conjugate of the former term. For the same modulation depth m_d of 1, the harmonic coefficients from H_0 to H_3 as functions of the normalized center wavenumber $\overline{x_v}$ have different curve shapes, as shown in Fig. 2.4.(a). Besides, for different m_d of 0.1, 0.5, 1, 2, and 3, the curve shapes of the first and the second harmonic components as functions of $\overline{x_v}$ are also different, with different peak-to-peak (p-p) values, as illustrated in Figs. 2.4.(b) and (c). Figure 2.4.(d) depicts the second harmonic component H_2 as functions of $\overline{x_v}$ and m_d. As m_d increases, the curve shape of H_2 as functions of $\overline{x_v}$ has two positive extrema with the same value moving away from $\overline{x_v} = 0$, making the shape seem to be broaden, as shown in Figs. 2.4.(c) and (d). The negative extremum has the maximum at $m_d = 2.2$.

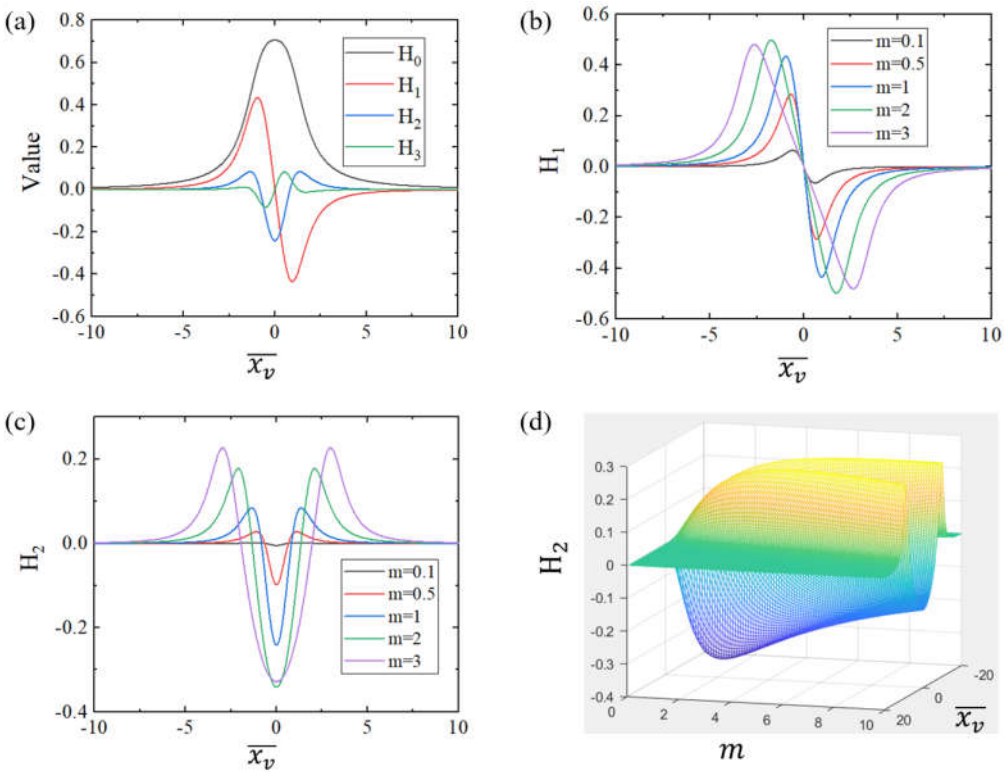

Figure 2.4 (a) The harmonic components from H_0 to H_3 for different normalized center wavenumber $\overline{x_v}$ with the modulation depth m_d of 1. The harmonic components (b) H_1 and (c) H_2 as functions of $\overline{x_v}$ for different m_d of 0.1, 0.5, 1, 2, and 3. (d) The second harmonic component H_2 as functions of $\overline{x_v}$ and m_d.

2.3 Hollow-core fibers

As a class of optical fibers, HCFs confine light beam mostly in a hollow core with less optical power propagating in a surrounding cladding formed with solid material, typically glass. HCFs mainly include hollow-core photonic bandgap fiber (HC-PBGF) and hollow-core anti-resonant fibers (HC-ARFs) with different light guiding mechanisms.

HC-PBGF confines the beam in the hollow core based on the photonic bandgap (PBG) effect with periodic air hole arrays in the cladding [10]. Figure 2.5(a) shows a typical

PBG structure formed through a hexagonal array consisting of circular air rods with the silica background (i.e., the gray regions). The $k-\beta$ plane of the structure is shown in Fig. 2.5(b). By placing a hollow defect in the center surrounded by the hexagonal-array structure, the light incident into the hollow defect may propagate in the hollow defect under the conditions that the wavelengths of the incident light are located at the bandgaps below the light line (i.e., the line with $k=\beta$).

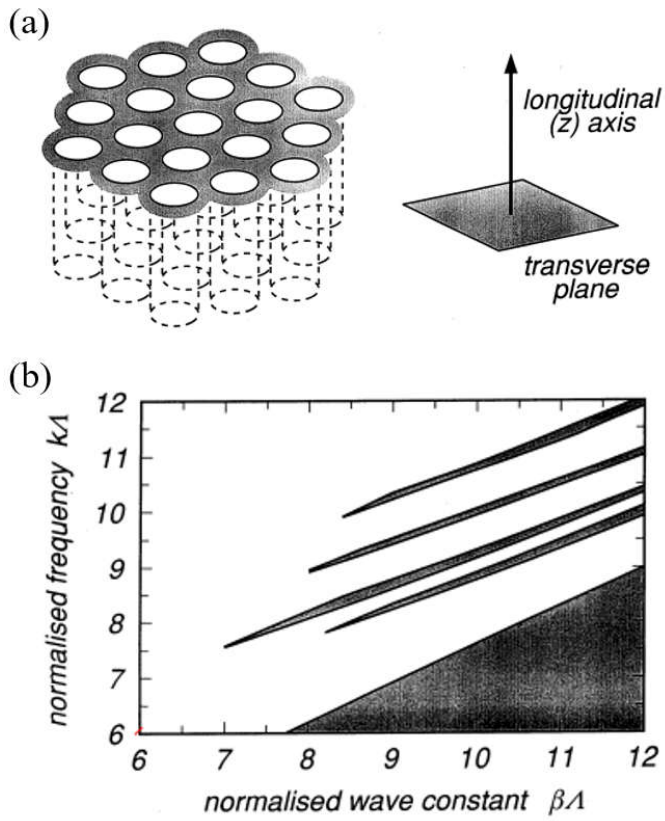

Figure 2.5 (a) Schematic diagram of a hexagonal array consisting of circular air rods with the silica background and (b) $k-\beta$ plane of the structure in (a) [11].

The transmission window of HC-PBGF is typically narrow and determined by the photonic bandgaps of the surrounding microstructured cladding. Figure 2.6 shows a HC-PBGF and its transmission loss spectrum. The HCF has the center wavelength located at ~1064 nm and the transmission bandwidth of ~150 nm.

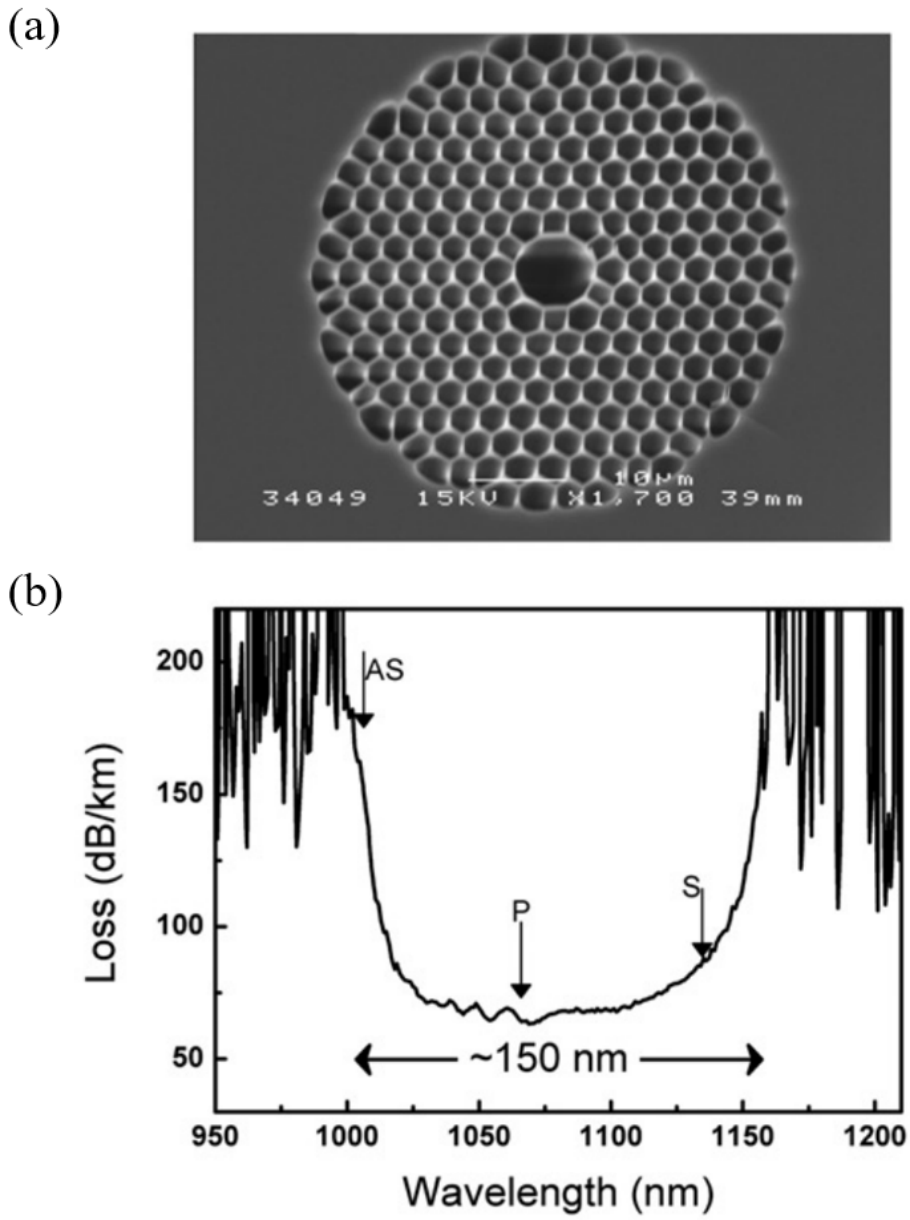

Figure 2.6 (a) SEM of the HC-PBGF and (b) its transmission loss spectrum [10].

The light guiding mechanism of HC-ARFs can be illustrated by use of anti-resonant reflecting optical waveguide (ARROW), with the hollow core surrounding by thin silica layers, as shown in Fig. 2.7(a) [12]. The transverse propagation intensity has the minima due to destructive interference at the anti-resonant wavelengths of an FP resonator in the low-index core layer, resulting in low leakage and thus the maximum transmission coefficient with a wide band as shown in Fig. 2.7(b).

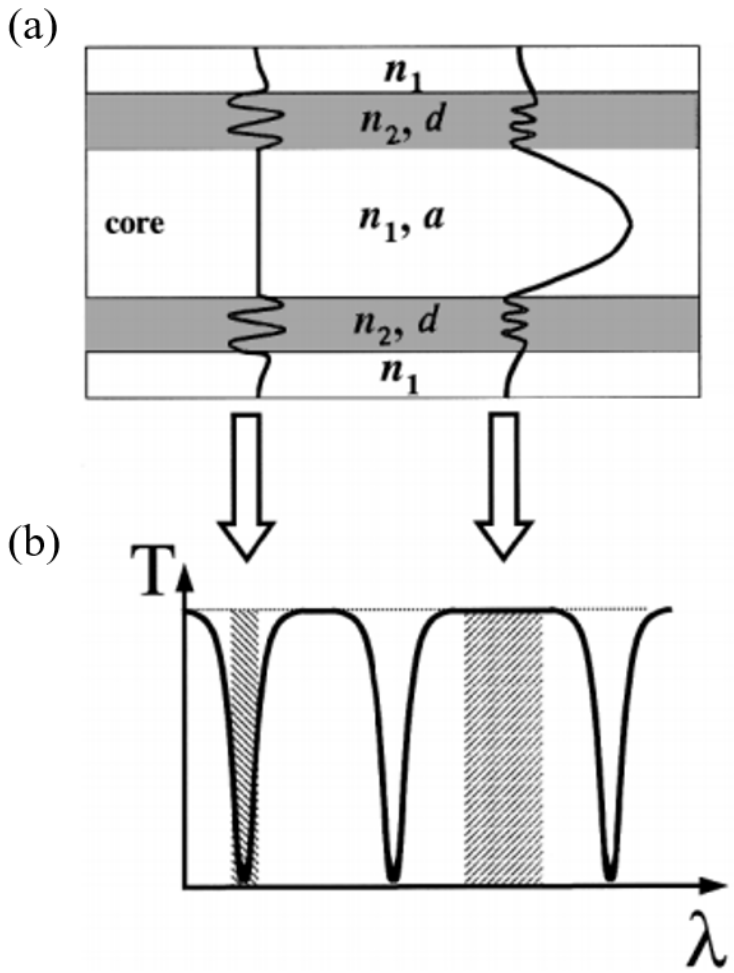

Figure 2.7 Schematic of (a) the ARROW structure and (b) its transmission spectrum [12].

Compared to HC-PBGFs, HC-ARFs can provide a broader transmission window. Figure 2.8 shows a HC-ARF and the transmission loss spectrum thereof. The HCF has the center wavelength located at ~1450 nm and the transmission bandwidth of ~300 nm.

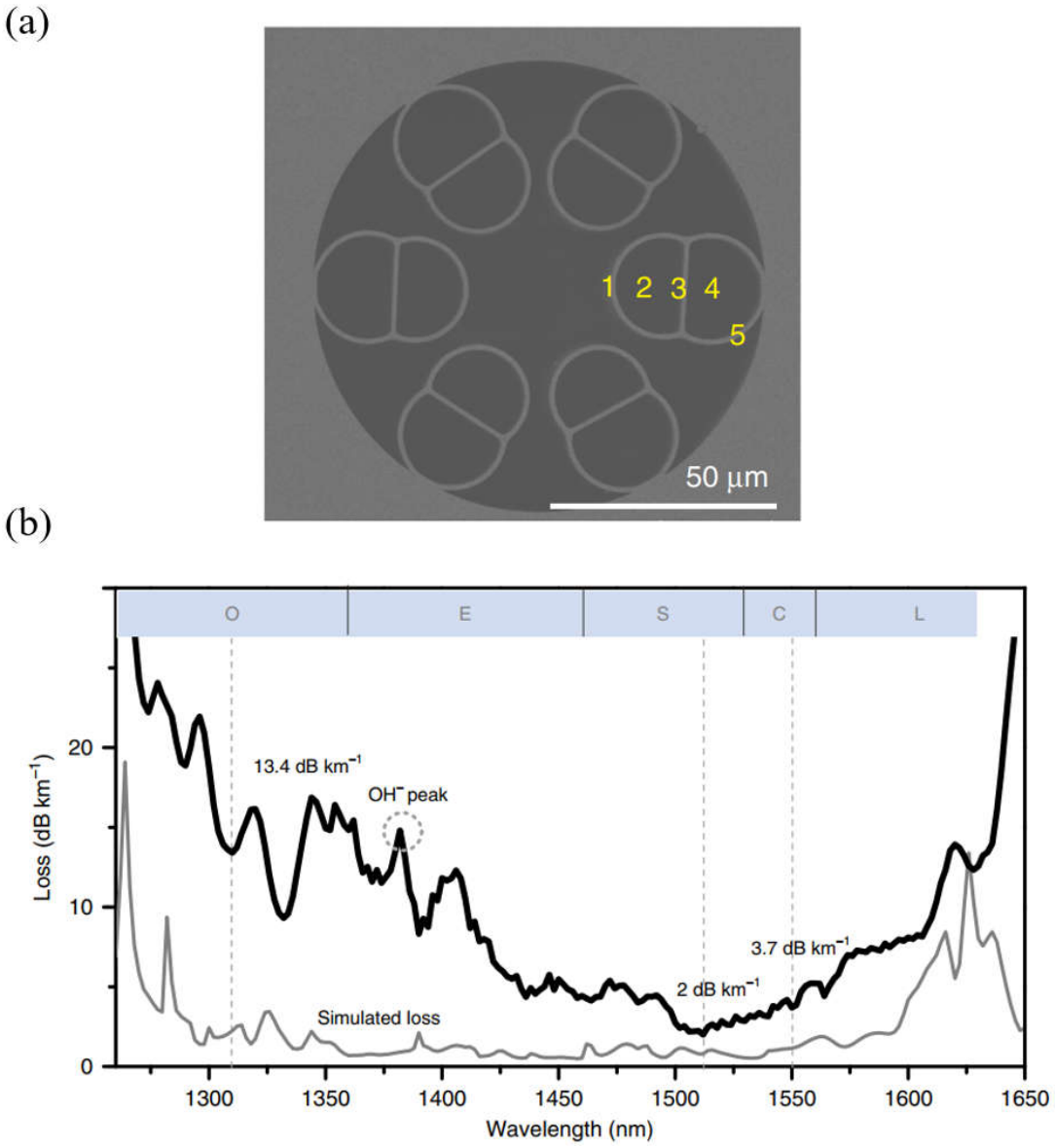

Figure 2.8 (a) SEM of the HC-ARF and (b) its transmission loss spectrum [13].

2.4 Photothermal spectroscopy with HCFs

According to the Beer-Lambert law, the phase changes induced by PT effect in an HCF under low concentration with the assumption of weak absorption may be approximated as [14-15]

$$\varphi_p = k'\alpha(\lambda_{pump})CLP_{pump} \tag{3.1}$$

where k' is the phase modulation coefficient and is a function of the pump modulation frequency, $\alpha(\lambda_{pump})$ is the absorption coefficient for the concentration of 100%, λ_{pump} is the wavelength of the pump, C is the target gas concentration, L is the HCF length, and P_{pump} is the average power of the incident pump beam. The phase modulation of a probe beam copropagating in the HCF can be detected by the PTS method.

In a PTS system, a pump-probe configuration is applied, with a pump laser absorbed by gas molecules inside a gas cell to generate heat via PT effect, which modulates the RI of the gas medium and hence the phase of a probe laser propagating through the optical fiber. The phase variations of the probe beam in the HCF can be measured through an optical interferometer.

To be specific, localized heating in the HCF is generated due to the absorption of the gas molecules, which can modify the pressure, temperature, density, and refractive index of the gas medium, and change the longitudinal and lateral length of the fiber [16]. In this case, the phase of the probe beam is modulated due to the localized heating. The process of the PT-induced phase modulation in an HCF can be explained in Fig. 2.9. The pump beam and probe beam enter the fiber from opposite sides, as shown in Fig. 2.9(a). The HCF is filled with gas. The pump beam has the center wavelength aligning to the absorption line of the target gas molecule and the probe beam can be any wavelengths only if it's not absorbed by the gas. Therefore, the pump beam is absorbed by the gas, leading to temperature, pressure and density variations of the filling gas, which further modify the RI of the gas medium and the lateral and longitudinal dimensions of the HCF, as shown in Fig. 2.9(b). The probe beam isn't absorbed by the gas, but its phase is modulated due to the RI and optical path variations. The phase modulation can be demodulated by interferometric methods. Many interferometric schemes are used to measure the phase modulation, such as the Mach-Zehnder interferometer (MZI) [17-18], modal interferometer [19], Fabry-Perot interferometer

(FPI) [20], white light interferometer [21] and Sagnac interferometer (SI) [22-23].

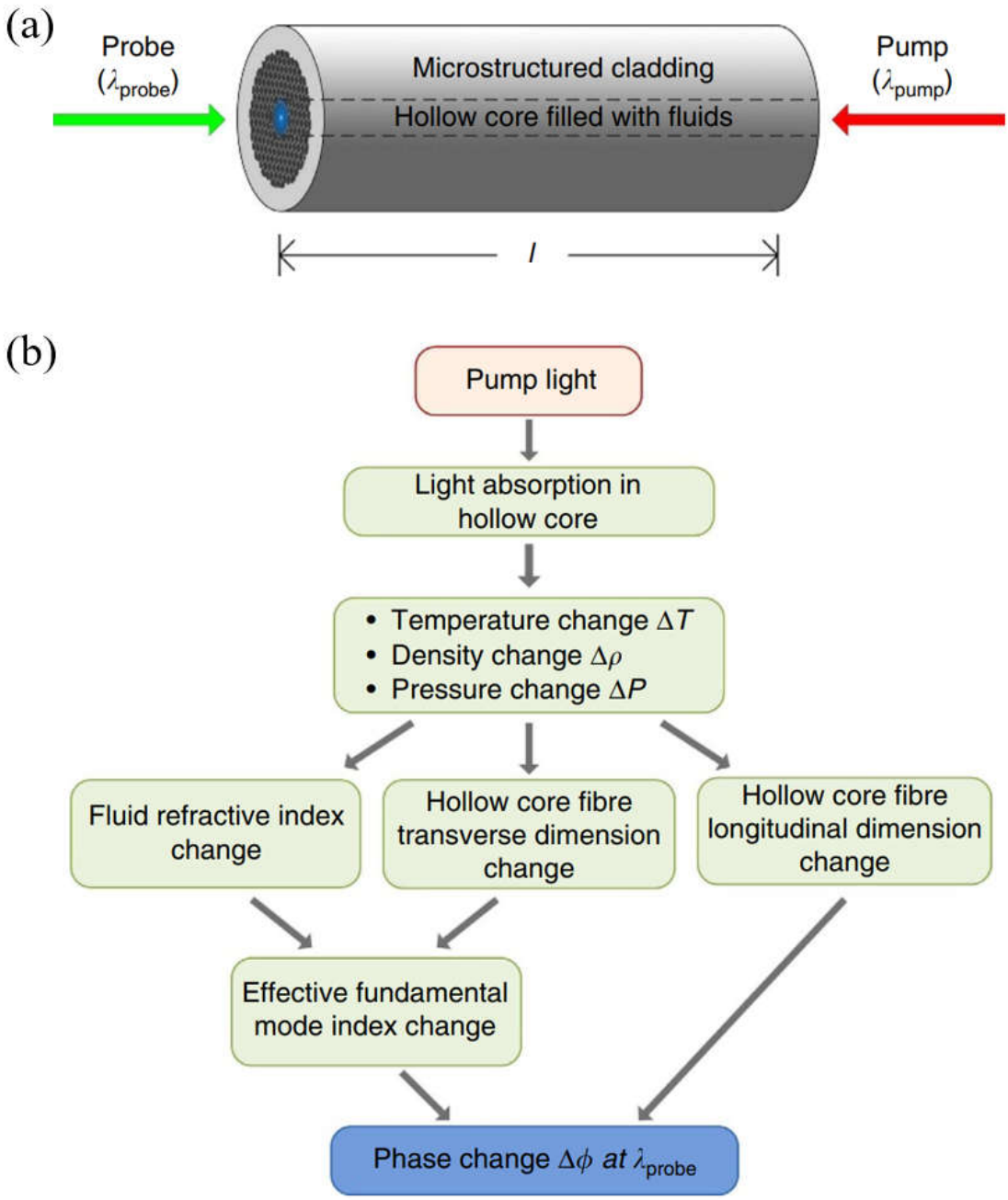

Figure 2.9 Schematic of the process of the PT-induced phase modulation in an HCF [14]. (a) The pump beam and probe beam enter the HCF from different sides. (b) Process of the phase modulation of the probe beam via the pump light.

2.5 Summary

The Beer-Lambert law is used to describe the relationship of the absorption of a laser beam to the target gas concentration, the absorption coefficient and the absorption length. The absorption lineshape may be one of the three types of functions, i.e., the Lorentzian, Gaussian and Voigt lineshapes according to different pressure and temperature. With WMS, different harmonic components can be derived from the absorption coefficient and are functions of the normalized center wavenumber and the modulation depth. The second harmonic component has a higher frequency and has the optimized modulation depth of 2.2 for the negative extremum. Hollow-core fibers can be classified into HC-PBGF and HC-ARF according to different light guiding mechanisms. PTS with HCFs detects the PT phase modulation in the HCF through interferometric methods with a pump-probe configuration.

2.6 References

1. G. Stewart, “Laser and fiber optic gas absorption spectroscopy,” Cambridge University Press (2021).

2. F. Schmidt, “Laser-based absorption spectrometry: development of NICE-OHMS towards ultra-sensitive trace species detection,” PhD Thesis, Umeå University (2007).

3. Y. Tan, “All optical fiber photothermal spectroscopic sensors for high sensitivity gas detection,” PhD Thesis, The HongKong Polytechnic University (2018).

4. B. H. Stuart, “Infrared spectroscopy: fundamentals and applications,” John Wiley & Sons (2004).

5. J. P. Besson, “Photoacoustic spectroscopy for multi-gas sensing using near infrared lasers,” PhD Thesis, École Polytechnic Federale De Lausanne (2006).

6. I.E. Gordon, L.S. Rothman, R.J. Hargreaves, R. Hashemi, E.V. Karlovets, F.M. Skinner, E.K. Conway, C. Hill, R.V. Kochanov, Y. Tan, P. Wcisło, A.A. Finenko, K. Nelson, P.F. Bernath, M. Birk, V. Boudon, A. Campargue, K.V. Chance, A. Coustenis, B.J. Drouin, J.–M. Flaud, R.R. Gamache, J.T. Hodges, D. Jacquemart, E.J. Mlawer, A.V. Nikitin, V.I. Perevalov, M. Rotger, J. Tennyson, G.C. Toon, H. Tran, V.G. Tyuterev, E.M. Adkins, A. Baker, A. Barbe, E. Canè, A.G. Császár, A. Dudaryonok, O. Egorov, A.J. Fleisher, H. Fleurbaey, A. Foltynowicz, T. Furtenbacher, J.J. Harrison, J.–M. Hartmann, V.–M. Horneman, X. Huang, T. Karman, J. Karns, S. Kassi, I. Kleiner, V. Kofman, F. Kwabia–Tchana, N.N. Lavrentieva, T.J. Lee, D.A. Long, A.A. Lukashevskaya, O.M. Lyulin, V.Yu. Makhnev, W. Matt, S.T. Massie, M. Melosso, S.N. Mikhailenko, D. Mondelain, H.S.P. Müller, O.V. Naumenko, A. Perrin, O.L. Polyansky, E. Raddaoui, P.L. Raston, Z.D. Reed, M. Rey, C. Richard, R. Tóbiás, I. Sadiek, D.W. Schwenke, E. Starikova, K. Sung, F. Tamassia, S.A. Tashkun, J. Vander Auwera, I.A. Vasilenko, A.A. Vigasin, G.L. Villanueva, B. Vispoel, G. Wagner, A. Yachmenev, and S.N. Yurchenko, “The HITRAN2020 molecular spectroscopic database,” Journal of Quantitative Spectroscopy and Radiative Transfer. 277, 1-82 (2022).

7. https://hitran.org/docs/iso-meta/

8. P. Kluczynski, J. Gustafsson, Å.M. Lindberg, and O. Axner, “Wavelength modulation absorption spectrometry — an extensive scrutiny of the generation of signals,” Spectrochim. Acta B At. Spectrosc. 56, 1277–1354 (2001).

9. Arndt, R, “Analytical line shapes for Lorentzian signals broadened by modulation,” Journal of Applied Physics. 36, 2522-2524 (1965).

10. F. Benabid, and P. J. Roberts, “Linear and nonlinear optical properties of hollow core photonic crystal fiber,” J. Mod. Opt. 58(2), 87–124 (2011).

11. T.A. Birks, P.J. Roberts, P.S.J. Russell, D.M. Atkin, and T.J. Shepherd, “Full 2-D

photonic bandgaps in silica/air structures," Electronics Letters. 31, 1941-1943 (1995).

12. N. Litchinitser, A. Abeeluck, C. Headley, and B. Eggleton, "Antiresonant reflecting photonic crystal optical waveguides," Optics letters. 27, 1592-1594 (2002).

13. S. Gao, Y. Wang, W. Ding, D. Jiang, S. Gu, X. Zhang, and P. Wang, "Hollow-core conjoined-tube negative-curvature fibre with ultralow loss," Nat. Commun. 9(1), 1–6 (2018).

14. W. Jin, Y. Cao, F. Yang, and H. L. Ho, "Ultra-sensitive all-fibre photothermal spectroscopy with large dynamic range," Nat. Commun. 6, 1-8 (2015).

15. P. Zhao, Y. Zhao, H. Bao, H.L. Ho, W. Jin, S. Fan, S. Gao, Y. Wang, and P. Wang, "Mode-phase-difference photothermal spectroscopy for gas detection with an anti-resonant hollow-core optical fiber," Nat Commun. 11, 847 (2020).

16. S.E. Bialkowski, "Photothermal spectroscopy methods for chemical analysis," John Wiley & Sons (1996).

17. C. Yao, Q. Wang, Y. Lin, W. Jin, L. Xiao, S. Gao, Y. Wang, P. Wang, and W. Ren, "Photothermal CO detection in a hollow-core negative curvature fiber," Opt. Lett. 44, 4048–4051 (2019).

18. G. Weihs, M. Reck, H. Weinfurter, and A. Zeilinger, "All-fiber three-path Mach–Zehnder interferometer," Opt. Lett. 21, 302-304 (1996).

19. A. Hassani, and M. Skorobogatiy, "Design of the microstructured optical fiber-based surface plasmon resonance sensors with enhanced microfluidics," Optics express. 14, 11616-11621 (2006).

20. F. Yang, Y. Tan, W. Jin, Y. Lin, Y. Qi, and H.L. Ho, "Hollow-core fiber Fabry–Perot photothermal gas sensor," Opt. Lett. 41, 3025-3028 (2016).

21. L. Yuan, “Multiplexed, white-light interferometric fiber-optic sensor matrix with a long-cavity, Fabry-Perot resonator,” Applied Optics. 41, 4460-4466 (2002).

22. Y. Lin, W. Jin, F. Yang, Y. Tan, and H. L. Ho, “Performance optimization of hollow-core fiber photothermal gas sensors,” Opt. Lett. 42, 4712–4715 (2017).

23. Y. Lin, W. Jin, F. Yang, J. Ma, C. Wang, H. L. Ho, and Y. Liu, “Pulsed photothermal interferometry for spectroscopic gas detection with hollow-core optical fibre,” Sci. Rep. 6, 1-12 (2016).

Chapter 3 Ultra-compact optical fiber gas sensor based on PTS

3.1 Introduction

PTS provides a sensitive technique for gas sensing [1-6]. For applications that require minimal sensor size and fast response, such as fault gas detection in energy storage systems, non-invasive gas detection from human breath, and gas recycling detection in closed spaces [7-9], we propose a miniature optical fiber gas sensor based on PTS. Light-gas interaction takes place at a small air-gap between the cleaved ends of two single mode fibers (SMFs), which also forms a low-finesse Fabry-Perot interferometer (FPI) for the detection of the PT phase modulation. Theoretical formulation and numerical simulation of phase modulation and detection for varying gap distance are carried out to achieve optimal system performance. A limit of detection (LOD) of 45 ppb for acetylene (C_2H_2) detection is realized with gap distance of 130 μm. The response time and dynamic range of the sensor are respectively 0.9 s and 2×10^7.

3.2 Basics of the gas sensor

Figure. 3.1(a) depicts the structure of the gas sensor. It is simply a low-finesse FPI formed between the cleaved ends of two SMFs. Probe and pump beams incident from the SMF on the left co-propagate in the air gap, as shown in Fig. 3.1(b). The light beam will diverge from the SMF into the air gap, as shown in Fig. 3.1(c). The pump beam is absorbed by gas molecules, which generates heat, changes the temperature distribution and modulates the refractive index (RI) of the gas medium. The RI modulation is detected by measuring the phase difference between the reflected probe beams, i.e., A_1 and A_2, as illustrated in Fig. 3.1(d). It should be noted that using ray optics in Fig. 3.1(d) is only for illustrative purposes.

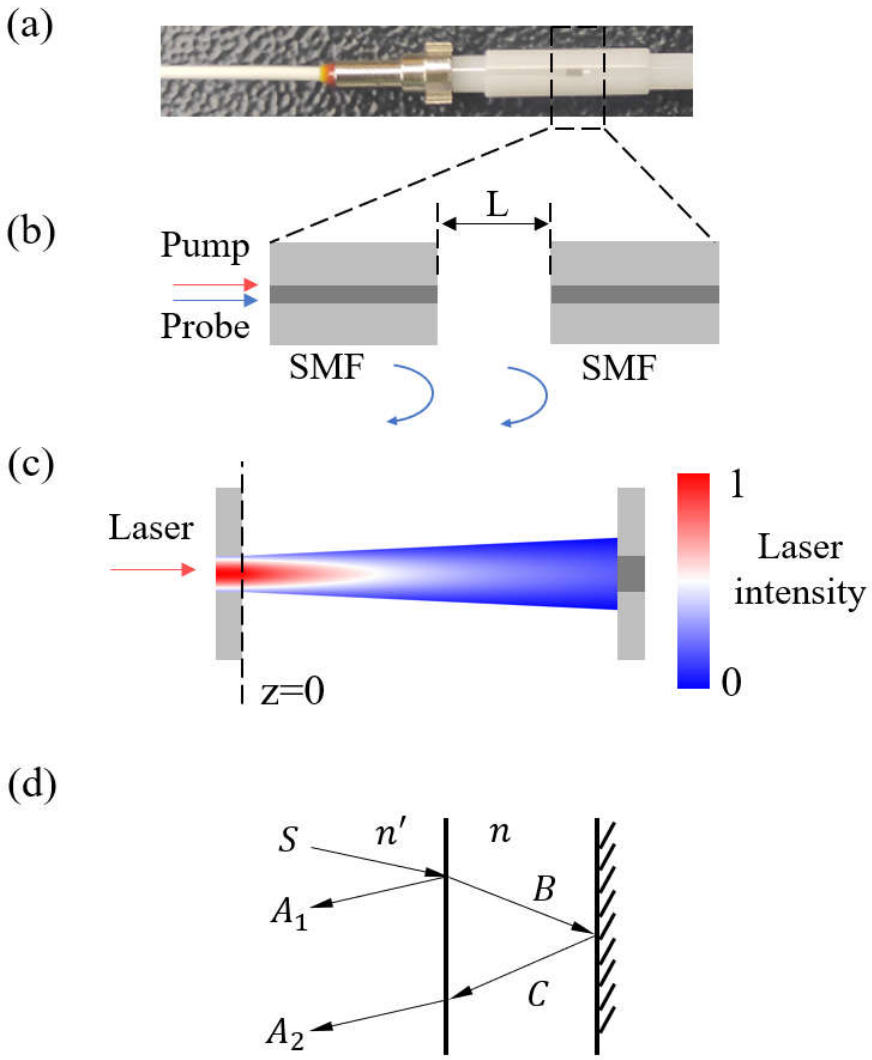

Figure 3.1 (a) FPI sensor head formed by two flat SMF endfaces with an air gap. Light is incident from the left SMF. The right SMF serves as a mirror here. (b) Schematic of the SMF-SMF sensor head, with L indicating the spacing distance between the two endfaces, and the pump and probe beams entering from the same side, where two reflected probe beams are obtained from the two endfaces, respectively. (c) Normalized intensity distribution of the incident laser after leaving the left end face. (d) Schematic of light propagation in the SMF and the air gap. n' and n are RI of the silica fiber and gas, respectively.

3.3 Theoretical formulation of the gas sensor

Analysis of FPI based on the plane wave model is well established [10]. Here the radial distribution of the light fields in the air gap may be approximated as a Gaussian profile with normalized amplitude distribution of $\exp(-r^2/w^2)$, where w is the mode field radius, and r is the radial distance from the center of the beam. Due to low reflectivity (~4%), high-order reflections at the fiber ends are ignored and FPI is regarded as a two-beam interferometer.

At the input fiber end, light beam (S) from the SMF is split into a reflected beam (A_1) and a transmitted beam (B), which is further reflected at the end of the right SMF. The reflected beam (C) is coupled back into the input SMF as beam A_2, as shown in Fig. 3.1(d). The mode field radius of B may be expressed as [11]

$$w_B(z) = w_0\sqrt{1 + (z/z_R)^2} \tag{3.1}$$

where w_0 is the mode field radius of S from the SMF, z is the distance away from the end of the input SMF, and z_R is the Rayleigh length at the incident wavelength λ in vacuum and equals $\pi n w_0^2/\lambda$. The mode field radius w_0 for both the pump and probe beams in the SMF may be approximated as 5.25 μm. Similarly, the mode field radius of C may be expressed as

$$w_C(z) = w_0\sqrt{1 + \left(\frac{2L-z}{z_R}\right)^2} \tag{3.2}$$

where L is the gap distance. The beams S, A_1 and A_2 propagating in the input SMF have the same mode field radius of w_0. The coupling efficiency from C to A_2 may be evaluated by using [12]

$$\eta = \frac{\left[\int_0^{\infty} \exp\left(\frac{-r^2}{w_0^2}\right) \exp\left(\frac{-r^2}{w_C(0)^2}\right) 2\pi r dr\right]^2}{\int_0^{\infty} \exp\left(\frac{-2r^2}{w_0^2}\right) 2\pi r dr \cdot \int_0^{\infty} \exp\left(\frac{-2r^2}{w_C(0)^2}\right) 2\pi r dr} \tag{3.3}$$

When the gap is filled with absorptive gas and the pump wavelength is tuned to an absorption line of the target gas molecules, a volume heat source $Q(r,z,t)$ is established due to PT effect and may be expressed as

$$Q(r,z,t) = P_{pump} W(t) \alpha C (1-R) \frac{2}{\pi w_B(z)^2} exp\left(\frac{-2r^2}{w_B(z)^2}\right) \tag{3.4}$$

where P_{pump} is the power and $W(t)$ is the modulation waveform of the pump, α is the gas absorption coefficient, C is the gas concentration. R is the reflectivity, which is assumed to be the same for both fiber ends. Due to the low reflectivity of the fiber ends, only a single-pass pump is considered here. The temperature distribution in the air gap may be obtained by solving the heat transfer equation [13]

$$\frac{\partial T}{\partial t} + u_r \frac{\partial T}{\partial r} + u_z \frac{\partial T}{\partial z} = \frac{\kappa}{\rho C_P}\left(\frac{\partial^2 T}{\partial r^2} + \frac{1}{r}\frac{\partial T}{\partial r} + \frac{\partial^2 T}{\partial z^2}\right) + \frac{Q}{\rho C_P} \tag{3.5}$$

where T represents the temperature, κ is the thermal conductivity, ρ is the density, and C_P is the isobaric heat capacity, u_r and u_z are the velocity fields in r and z direction, respectively. The distribution of RI change of the gas medium in the gap may be obtained by using Lorentz-Lorentz formula [14]

$$\Delta n(r,z,t) = -(n-1)\frac{T - T_{amb}}{T_{amb}} \tag{3.6}$$

where T_{amb} is the ambient temperature.

The phase modulation of the propagating probe beam due to PT effect is a function of z. The total accumulated phase change for B from the left to the right may be expressed as [15]

$$\Delta\phi_B(t) = \frac{2\pi}{\lambda_{pr}} \int_0^L \int_0^\infty \Delta n \frac{2}{\pi w_B(z)^2} \exp\left(\frac{-2r^2}{w_B(z)^2}\right) 2\pi r dr dz \tag{3.7}$$

and the total accumulated phase change for C from right to left may be expressed as

$$\Delta\phi_C(t) = \frac{2\pi}{\lambda_{pr}} \int_0^L \int_0^\infty \Delta n \frac{2}{\pi w_C(z)^2} \exp\left(\frac{-2r^2}{w_C(z)^2}\right) 2\pi r dr dz \tag{3.8}$$

where λ_{pr} is the wavelength of the probe beam.

Let amplitude of electric vector of the probe beam S to be 1, then the amplitudes of the reflected beams A_1 and A_2 should be $\sqrt{R}$ and $(1-R)\sqrt{R}\sqrt{\eta}$, respectively. In the absence of PT phase modulation, the phase difference between A_1 and A_2 can be expressed as $\pi + \delta$, where δ equals $4\pi nL/\lambda$. The total reflected light field $A^{(R)} = A_1 + A_2$ may be expressed as

$$A^{(R)} = \sqrt{R} - (1-R)\sqrt{R}\sqrt{\eta}\exp(i\delta) \tag{3.9}$$

With PT modulation, $A^{(R)}$ may be expressed as

$$A^{(R)} = \sqrt{R} - (1-R)\sqrt{R}\sqrt{\eta}\exp[i(\delta + \Delta\phi)] \tag{3.10}$$

where $\Delta\phi$ is the total phase modulation and equals to $\Delta\phi_B + \Delta\phi_C$. The interference intensity of the reflected light field is thus

$$I_r = A^{(R)} A^{(R)^*} \tag{3.11}$$

where $A^{(R)^*}$ is the complex conjugate of $A^{(R)}$. The fringe contrast may be expressed as

$$Fringe\ contrast = \frac{\max(I_r) - \min(I_r)}{\max(I_r) + \min(I_r)} = \frac{2\sqrt{\eta}(1-\mathrm{R})}{1+\eta(1-\mathrm{R})^2} \tag{3.12}$$

The fringe contrast can be determined from the measured interferometric fringes of the

FPI. As an example, the reflected spectrum of a FPI with a gap distance of 130 μm is shown in Fig. 3.2(a), which has the fringe contrast of ~0.7 and free spectral range (FSR) of 9 nm. The dBm scale is changed into the linear amplitudes with the mathematical relationship of $P_{mW} = 10\text{^}(P_{dBm}/10)$. The gap distance L can be determined from FSR of the interferometric fringes by using $\lambda_c^2/(2n \cdot FSR)$, where λ_c is the wavelength of the nearest transmission peak and n is the RI of the gas medium [16]. The fringe contrasts for different gap distances from 10 to 1000 μm are calculated using (3.12) and experimentally determined from the measured interferometric fringes, and are shown in Fig. 3.2(b). The fringe contrast decreases as the gap distance increases, because the coupling efficiency η decreases due to beam divergence according to (3.3). The calculated results are in good agreement with the experimental results by taking account of the mode field coupling efficiency and 4% reflection at the SMF endfaces. With the wavelength λ_{pr} of the probe beam stabilized around the quadrature point of the interferometric fringes near 1550 nm, corresponding to $\delta = \pi/2$, as shown in Fig. 3.2(a), the FPI converts the PT modulation efficiently to intensity modulation at the FPI output, which is the PT signal. As the conversion efficiency is proportional to fringe contrast, a high fringe contrast is preferred to maximize the PT signal.

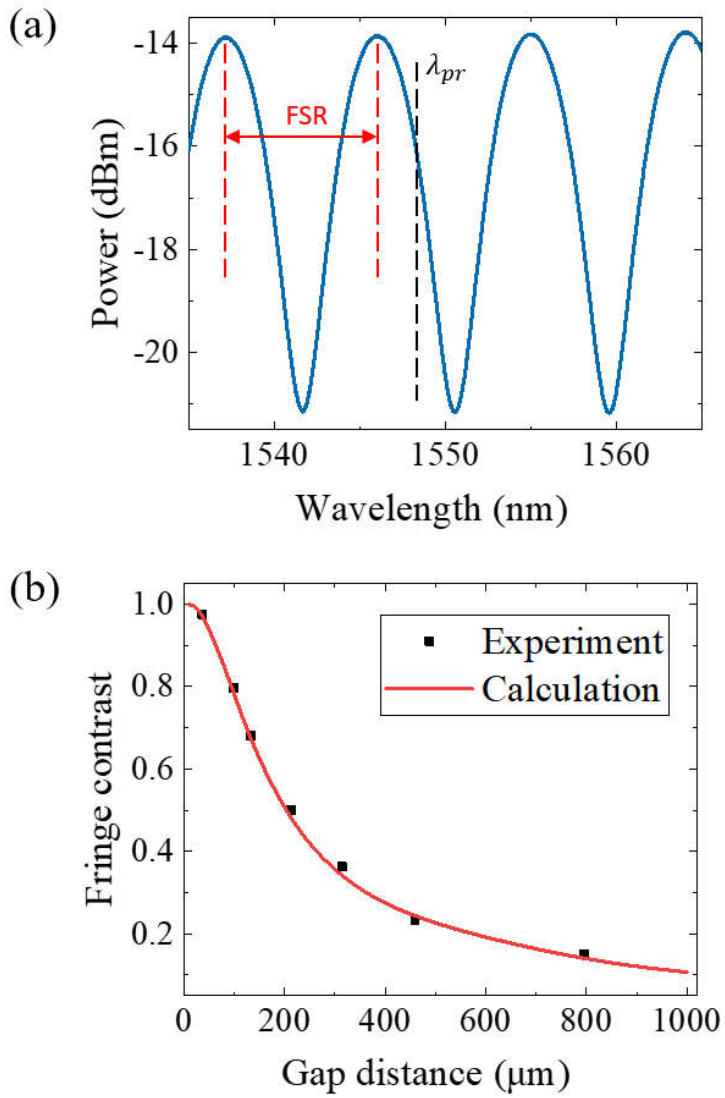

Figure 3.2 (a) Measured interferometric fringes of the FPI with gap distance of 130 μm. (b) Experimental and calculated results of the fringe contrast as functions of gap distance.

3.4 Simulation of the PT phase modulation

The PT phase modulation can be numerically calculated by using COMSOL Multiphysics with the simulation model shown in Fig. 3.3(a). The two-dimensional (2D) axisymmetric module is used for calculating the temperature field, with the rotation axis denoted by a red chain-dotted line. Two SMFs and the air gap are set as two solid

regions and a fluid region, respectively. The outer surfaces of the two SMFs are set to 293.15 K. The peripheries of both the SMFs and the air gap are set as thermal insulation. The absolute pressure of the fluid region is set as 1 atm. The pump power is assumed sinusoidally modulated with $W(t) = 0.5 + 0.5\cos(2\pi f t)$, where f is the modulation frequency. A volume heat source $Q(r, z, t)$ is firstly established according to (3.4) and then applied to the fluid region. After the simulation of heat transfer, the temperature field is extracted and applied to calculate the RI change according to (3.6). Then the phase modulations are calculated by integrating over the fluid region according to (3.7) and (3.8). Finally, the intensity modulation of the FPI output is calculated according to (3.10) and (3.11).

Fig. 3.3(b) shows the calculated FPI output intensity modulation waveform for the pump modulation frequency of 2 kHz and temperature distribution at different times. The gap is 130 μm and filled with pure C_2H_2. The wavelength of the pump beam is 1532.83 nm, corresponding to the P (13) absorption line of C_2H_2. The pump power is ~8 dBm. Wavelength of the probe beam is 1550 nm. After incidence of the pump beam, due to the interplay of heat generation in the fluid region and dissipation to the boundaries, it takes ~0.5 ms to reach a dynamic thermal equilibrium. Then the intensity I_r is stably sinusoidally modulated and has the peak-to-peak modulation amplitude ΔI_{r} of 0.00065.

To better understand the modulation process, Figs. 3.3(c-f) show respectively the distributions of the pump intensity, heat source, temperature and RI distribution at the time of 1 ms. The light field diverges from the left SMF to the right SMF and hence the generated heat is more concentrated near the left SMF, as shown in Figs. 3.3(c-d). The maximum temperature locates near the center of the gap and the temperature decreases from the center to all directions, but decreases faster towards the left and right SMFs and slower in radial direction, as shown in Fig. 3.3(e). The faster rate of decrease in the direction of the fibers is because that the thermal conductivity of the silica is 50 times

larger than that of the gas, and thus the thermal conduction of the solid silica dominates the heat dissipation process. The distribution of RI is similar to that of temperature, as shown in Fig. 3.2(f). Hence the center region of the gap contributes most to the accumulated phase modulation. The inset in Fig. 3.2(b) shows the temperature distribution along the rotation axis from 1 ms to 1.25 ms, half a period of the pump modulation. From 1 ms to 1.25 ms, as the pump intensity decreases, the location of the highest temperature moves from left to closer to the center, as shown by the green dashed line. The pump intensity near the left SMF is higher, which results in higher temperature on the left. As the pump power increases, the temperature difference becomes larger.

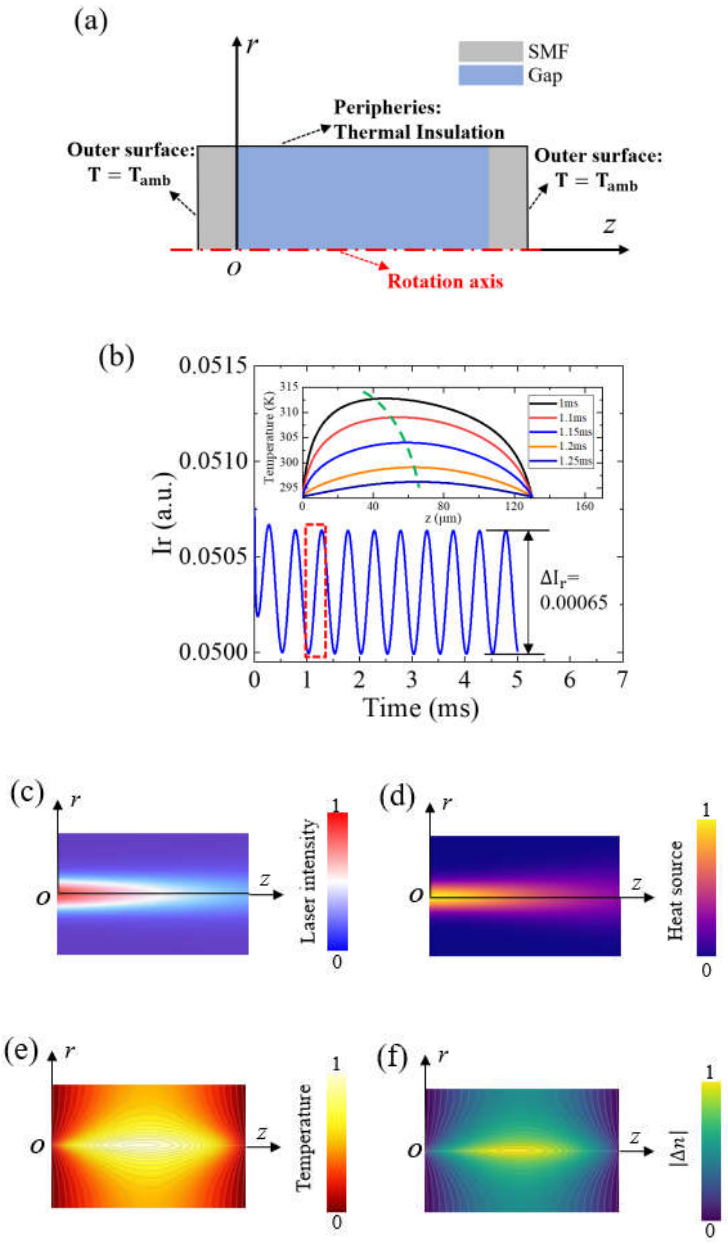

Figure 3.3 (a) Schematic of the simulation model. (b) Calculated results of I_r in time domain for a pump modulation frequency of 2 kHz. The gap distance is 130 μm. The inset is the evolution of temperature distribution along axis of symmetry from z=0 to z=130 μm during half a period indicated by the red dotted box. (c) Normalized laser intensity distribution, (d) heat source distribution, (e) temperature distribution, and (f) RI distribution in the gap at the time of 1 ms. The contour lines in (e-f) are used to indicate the gradient of the change.

3.5 Determining the frequency response

The simulation in section 3.4 is repeated for different modulation frequencies to determine the frequency response of the PT phase modulation, which is also experimentally investigated with the setup shown in Fig. 3.4(a). The pump beam is from a 1532.83-nm distributed feedback (DFB) laser, with its wavelength located at the P (13) absorption line of C_2H_2. The pump intensity is sinusoidally modulated by an acoustic-optic modulator (AOM) with the input electrical signal from a lock-in amplifier (LIA) and then boosted by an erbium-doped fiber amplifier (EDFA). The probe beam is a tunable semiconductor laser (TSL) with wavelength set at the quadrature point of the FPI near 1550 nm. The pump and probe beams are combined through a 1550 / 1530 nm wavelength-division multiplexer (WDM) and co-propagate into the FPI. It should be noted that several WDMs in series are needed to suppress the reflected pump beam so that the residual pump will not increase the system noise. The first harmonic $(1f)$ component of the PT signal due to the intensity modulation of the pump beam is demodulated by the LIA [17].

Experimental and calculated results of the frequency response for the gap distance of 130 μm are shown in Fig. 3.4(b). The experimental conditions are the same as those used in the simulation as described in 3.4. The calculated results are in good agreement with the experimental results. The amplitude ΔI_r of intensity modulation reduces with increasing modulation frequency and the -3 dB roll-off frequency f_{3dB} is ~15 kHz. The -3-dB roll-off frequencies f_{3dB} for different gap distances from 0 to 1000 μm are also measured and calculated, as shown in Fig. 3.4(c). f_{3dB} decreases as the gap distance increases, and reaches 100 kHz at ~35 μm, 50 kHz at ~60 μm and 10 kHz at ~180 μm. The deviation between the experimental and calculated results for gap distance larger than ~400 μm may be resulted from the theoretical plane wave approximation along z direction for pump absorption.

The 3-dB roll-off frequency depends on the heat accumulation and dissipation of the structure of the sensing unit. For the system at dynamic thermal equilibrium, the heat accumulation mainly locates near the center of the fluid region, and the heat dissipation mainly takes place from the fluid region to the left and right solid regions. The tendency of f_{3dB} as function of gap distance may be explained in analogy with a low-pass electrical filter, with the heat accumulation regarded as a capacitor and the heat dissipation as a resistor. The more heat is accumulated, the higher phase modulation will be achieved, just like a low-pass filter with higher voltage output for more electrical storage. For the same sensor unit, the generated heat has enough time to be accumulated at a low frequency, just like a low-pass filter with enough charging time at a low frequency. Therefore, the modulation amplitude decreases as the frequency increases. For a sensor unit with a larger gap, not only is more heat accumulation space provided, but also it would be difficult for heat dissipation from the center to both sides (i.e., higher capacitance and resistance), resulting in a lower -3-dB roll-off frequency, just like a low-pass filter with its cutoff frequency inversely proportional to its capacitance and resistance. As a result, the -3-dB roll-off frequency of the sensing unit decreases as the gap distance increases.

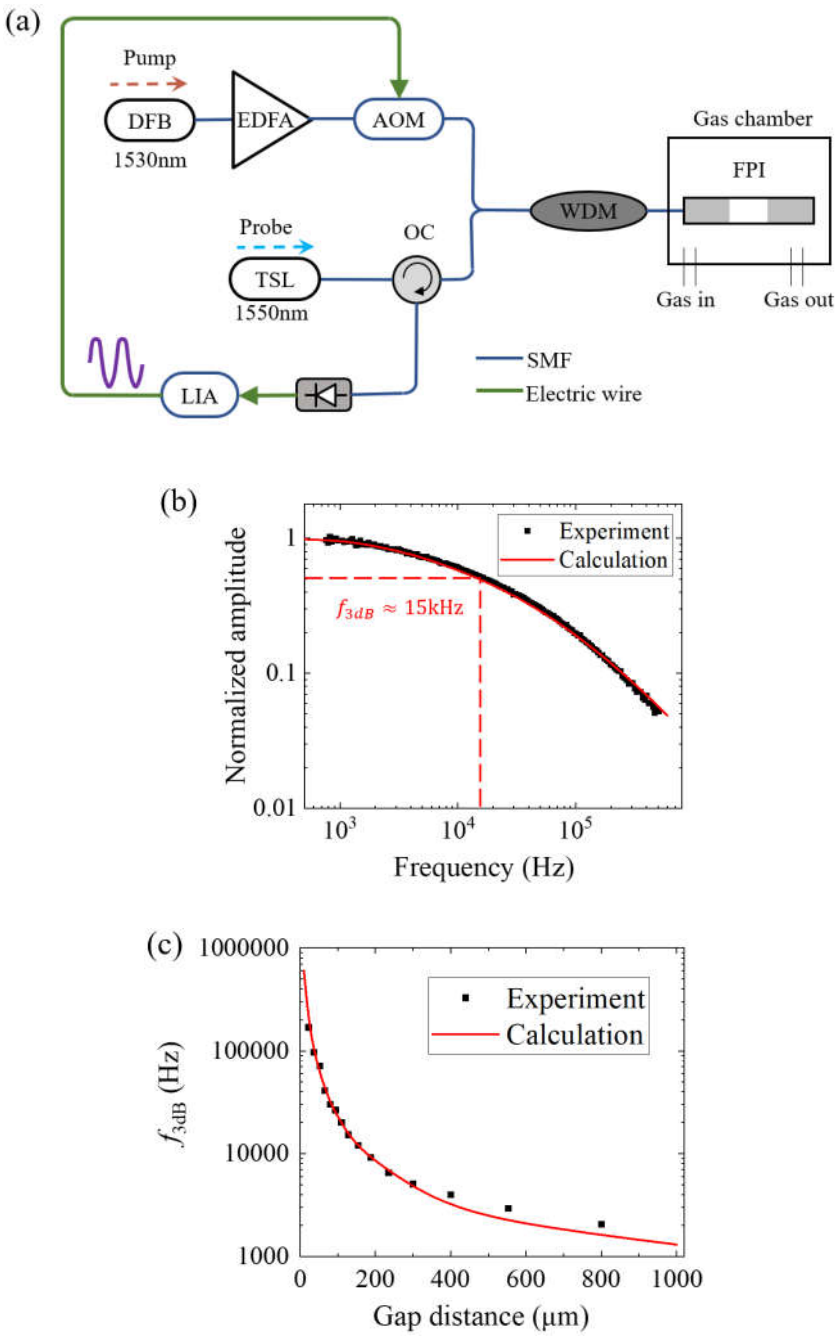

Figure 3.4 (a) Experimental setup for measuring frequency response. OC: optical circulator, PD: photodetector. (b) Experimental and calculated results of frequency response of the sensor with the gap distance of 130 μm. (c) Experimental and calculated -3-dB roll-off frequencies.

3.6 Influence of gap distance on PT signal

The amplitude of PT phase modulation as function of different gap distance from 0 to 1000 μm is calculated by using (3.1) to (3.8) and shown in Fig. 3.5(a). The parameters used for calculation are the same as in Section 3.4 except that the pump power is now 15 dBm and the modulation frequency is 20 kHz. The total phase modulation $\Delta\phi$ increases as the gap distance increases. However, component $\Delta\phi_B$ increases with gap distance while $\Delta\phi_C$ increases first and reaches its peak around 200 μm and then decreases with further increasing the gap distance. This is because the initial transmitted probe beam B overlaps significantly with the pump beam and the heated region, and hence $\Delta\phi_B$ increases monotonically with the gap distance. For small gap distance of less than 200 μm, the reflected probe beam C does not diverse badly and still has a good overlap with the pump beam, hence $\Delta\phi_C$ increases with gap distance. However, as the gap distance further increases, the beam size of the reflected probe increases significantly and the overlap with the heated region becomes small, causing $\Delta\phi_C$ to reduce with the gap distance.

The PT phase modulation is converted into intensity modulation at the output of the FPI, as discussed in Section 3.3. The conversion efficiency depends on the fringe contrast and is related to the reflectivity R of the fiber endfaces and the light coupling efficiency η for the probe beam, as shown in (3.3) and (3.12). The overall PT signal is therefore affected by both the total PT phase modulation $\Delta\phi$ and the fringe contrast. $\Delta\phi$ increases with the gap distance, as shown in Fig. 3.5(a). However, the fringe contrast, reduces with increasing gap distance due to decreasing in η. The measured and calculated amplitude of PT signal ΔI_{r}, for different gap distances from 0 to 1000 μm, is shown in Fig. 3.5(b). As the gap distance increases, ΔI_{r} increases first and then decreases with a peak at ~130 μm.

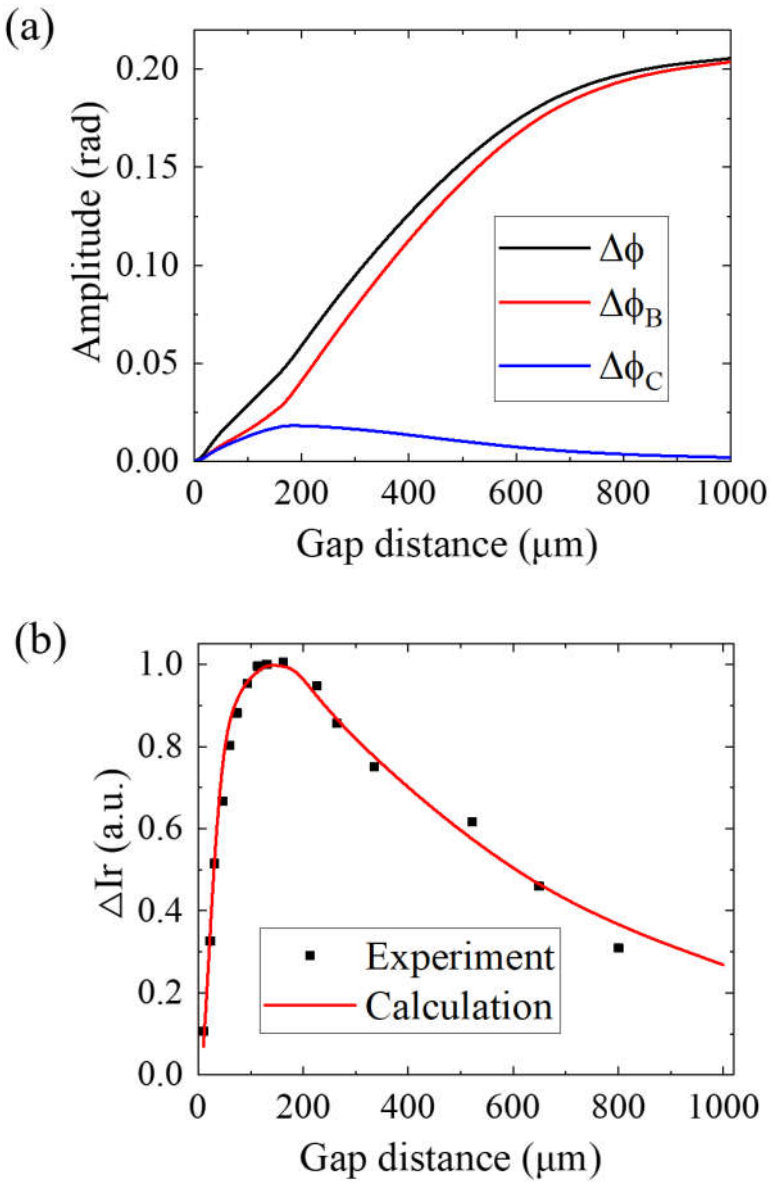

Figure 3.5 Influence of gap distance on PT signal. (a) Calculated phase modulation amplitude for pump modulation frequency of 20 kHz. (b) Experimental and calculated results of ΔI_r at the modulation frequency of 20 kHz.

3.7 Gas detection

We evaluated the performance of a gas sensor with gap distance of ~130 μm for acetylene detection. Fig. 3.6(a) depicts the experimental setup. In comparison with the

experimental setup in Fig. 3.4(a), the pump beam is from a 1530.37-nm distributed feedback (DFB) laser, with its wavelength modulated sinusoidally at 2 kHz and at the same time scanned across the P (9) absorption line of C_2H_2. The pump power is boosted by an erbium-doped fiber amplifier (EDFA). The second harmonic ($2f = 4$ kHz) component of the PT signal from the wavelength modulation spectroscopy is demodulated by the LIA to reduce the background noise [1]. The absolute pressure in the gas chamber is 1 atm.

The experiments were firstly conducted with 1% C_2H_2 balanced with nitrogen (N_2). Fig. 3.6(b) illustrates the LIA $2f$ output for different pump power from 22 dBm to 28 dBm. The peak-to-peak (p-p) value from the LIA $2f$ output increases linearly as the pump power increases. Fig. 3.6(c) shows the p-p values of PT phase modulation signals for 0.01%, 0.1%, 1%, 10% C_2H_2 balanced in N_2 and pure C_2H_2 with pump power of 28 dBm. An approximately linear relationship is obtained for C_2H_2 concentration up to 100%. The noise is measured by filling the gap with pure N_2. The SNR is 5965 for the signal of 1% C_2H_2 and an integration time of 1 s. The noise-equivalent-concentration (NEC) is calculated by C_2H_2 concentration of 1% divided by the SNR and is 1.7 ppm.

Allan deviation analysis is conducted to investigate the stability of the proposed FPI gas sensor with PTS. Allan plot of the baseline noise is recorded for 4 hours when the FPI is filled with pure N_2 and the pump power is 28 dBm, as shown in Fig. 3.6(d). The NEC for 10 s, 100 s, and 1000 s averaging time are 540 ppb, 150 ppb and 45 ppb, respectively. A dynamic range of 2×10^7 is obtained by 100% divided by 45 ppb.

The response time of the gas sensor is estimated by filling the gas chamber with 0.1% C_2H_2 in N_2. The pump wavelength is fixed at the P (9) absorption line of C_2H_2 with pump power of 28 dBm. At ~1 s, 0.1% C_2H_2 balanced in N_2 is filled into the gas chamber with flow rate of ~300 sccm, and at ~69 s, pure N_2 is filled into the gas chamber with the same flow rate. The signal of the LIA output as a function of time is

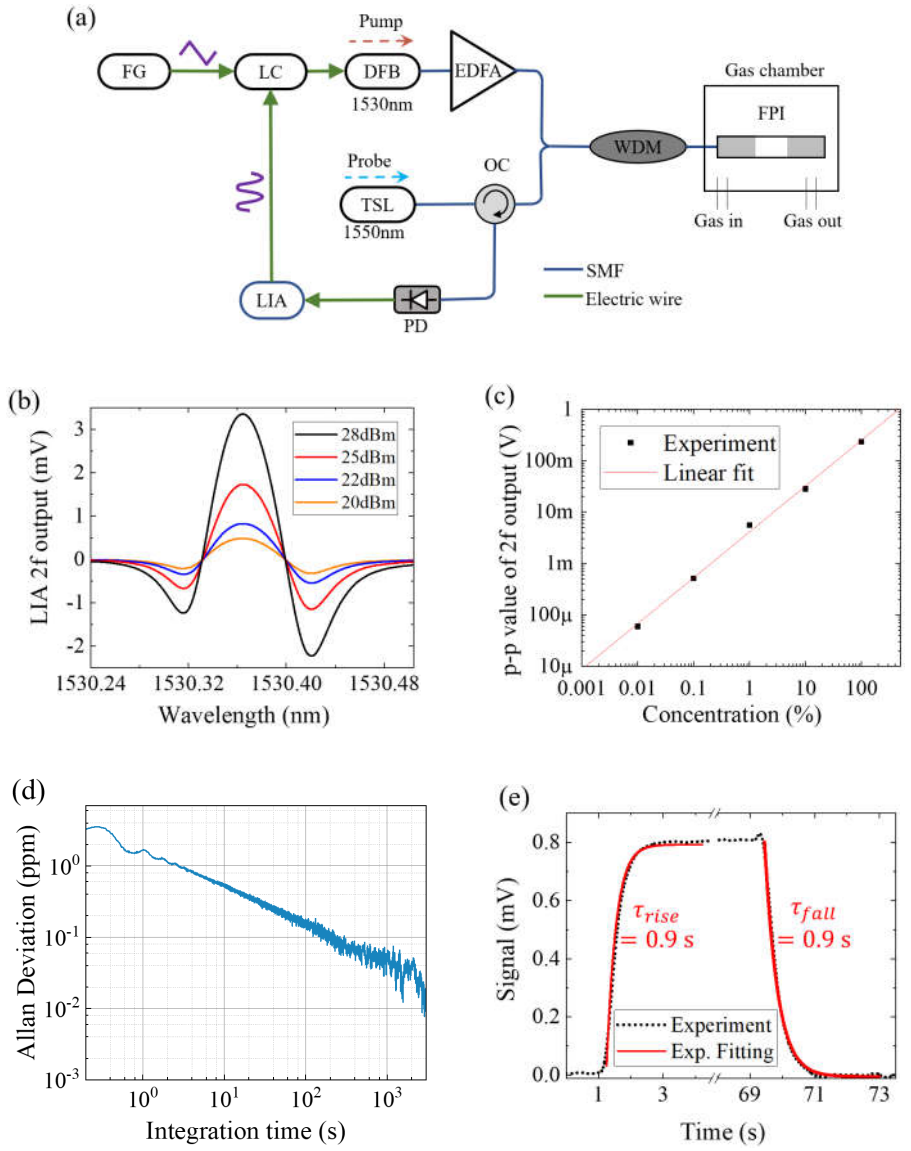

Figure 3.6 Gas detection with a sensor with the gap distance of 130 μm. (a) Experimental setup. LC: laser controller. (b) Measured LIA 2*f* output of the PT phase modulation for different pump power from 20 dBm to 28 dBm. The gas is 1% C_2H_2 balanced with N_2. (c) Experimental results and linear fit of p-p values of the LIA 2*f* output as functions of gas concentration. The pump power is 28 dBm. (d) Allan deviation analysis of the baseline noise over a period of 4 hours when the FPI is filled with pure N_2. The pump power is 28 dBm. The time constant of the LIA is 100 ms. (e) The measured 2*f*-signal in time domain during gas loading and unloading. The pump power is 28 dBm and the gas is 0.1% C_2H_2 balanced with N_2.

recorded and shown in Fig. 3.6(e). Exponential fitting shows that the response time t_{90} is ~0.9 s for both the rising and the falling processes.

3.8 Comparison with gas sensors using HCFs

The performances of some recently published optical fiber gas sensors for C_2H_2 detection are summarized in Table 3.1. There sensors use hollow-core photonic bandgap fiber (HC-PBGF) or hollow-core anti-resonant fiber (HC-ARF), and based on direct absorption wavelength modulation spectroscopy or PTS [1-6,15, 17-24]. The SMF sensor presented here is the smallest in size (130 μm long), which is 100 times shorter than the shortest HCF sensors reported. It also has the shortest response time of 0.9 s. Sub-ppm NEC is realized with the dynamic range larger than 7 orders of magnitude. In addition, the very small gas distance (0.13 mm) results in a large fringe spacing of ~10 nm, making the system insensitive to environmental perturbation and avoiding the use of servo-control to stabilize the interferometer, which is often needed for HCF based PTS sensors.

The short air gap can achieve the enhanced efficiency of PT modulation and reduced noise in the detection system. The area of the light beam coming out from the SMF is considerably smaller than that of the HC-ARF, resulting in higher pump power density and thus higher local heating. The PT modulation per unit length is thus larger than that of HCFs. The SMF has better mode purity, and the very small gas distance means the two interference beams return to the SMF almost simultaneously, making the system insensitive to external disturbance.

Table 3.1. Performances of some recent gas sensors with HCFs for C_2H_2 detection.

Year	Fiber type	Length/m	Technique	Wi/wo stabilization	Response time/s	NEC/ppb	Dynamic range
2014 [21]	HC-PBGF	13	WMS	wo	Not stated	1000	Not stated
2015 [1]	HC-PBGF	10	MZI-PTS	wi	7200	2	5.3*10^5
2016 [15]	HC-PBGF	0.62	SI-PTS	wo	Not stated	3300	Not stated
2016 [22]	HC-PBGF	0.3	MZI-PTS	wi	Not stated	1000	Not stated
2016 [22]	HC-PBGF	0.62	SI-PTS	wo	Not stated	775	Not stated
2016 [23]	HC-PBGF	0.02	FPI-PTS	wo	19	117	Not stated
2017 [3]	HC-PBGF	1.1	SI-PTS	wo	Not stated	18	Not stated
2017 [24]	HC-PBGF	0.094	CA-WMS	wo	Not stated	7000	Not stated
2018 [18]	HC-PBGF	0.62	IC-PTS	wo	Not stated	176	Not stated
2019 [20]	HC-PBGF	0.062	CA-FPI	wi	60	126	Not stated
2020 [5]	HC-ARF	4.67	MI-PTS	wo	44	0.015	2*10^7
2020 [17]	HC-ARF	0.055	FPI-PTS	wi	52	2.3	4.3*10^6
2021 [19]	HC-ARF	0.3	PABS	wo	Not stated	8	Not stated
2022 [6]	HC-ARF	0.1	OPMA-PTS	wi	Not stated	2.7	Not stated
This work	SMF	0.00013	FPI-PTS	wo	0.9	45	2*10^7

WMS: wavelength modulation spectroscopy, MZI: Mach Zehnder interferometer, SI: Sagnac interferometer, CA: cavity-enhanced, IC: intracavity, MI: modal interference, PABS: photoacoustic Brillouin spectroscopy, OPMA: optical-phase-modulation amplifying.

3.9 Summary

In summary, we demonstrate an ultra-compact optical fiber gas sensor based on PTS. The sensing unit is a low-finesse FPI formed by an air gap between the cleaved ends of two SMFs. PT phase modulation and detection of the sensor are studied by theoretical formulation and numerical simulation as well as experimental investigation for different gap distance to achieve optimal system performance. Theoretical and experimental results show that intensity modulation amplitude of the FPI output has an optimal value at ~130 μm. The sensor is insensitive to external disturbance because of the short cavity length with FSR of ~10 nm, without the requirement of controlling the

probe wavelength accurately. LOD of 45 ppb for C_2H_2 with a dynamic range of 2×10^7 is demonstrated with gap distance of 130 μm. The response time of the sensor is 0.9 s. The gas sensor is simple to construct, and may be used for real-time gas detection that requires compact sensors with fast response.

3.10 References

1. W. Jin, Y. Cao, F. Yang, and H. L. Ho, "Ultra-sensitive all-fibre photothermal spectroscopy with large dynamic range," Nat. Commun. 6, 1-8 (2015).

2. Z.L.I. Hili, Z.H.E.N.W. Ang, F.A.N.Y. Ang, and W.E.I.J. In, "Mid-infrared fiber-optic photothermal interferometry," Opt. Lett. 42, 3718–3721 (2017).

3. Y. Lin, W. Jin, F. Yang, Y. Tan, and H. L. Ho, "Performance optimization of hollow-core fiber photothermal gas sensors," Opt. Lett. 42, 4712–4715 (2017).

4.C. Yao, S. Gao, Y. Wang, P. Wang, W. Jin, and W. Ren, "MIR-pump NIR-probe fiber-optic photothermal spectroscopy with background-free first harmonic detection," IEEE Sens. J. 20, 12709–12715 (2020).

5. P. Zhao, Y. Zhao, H. Bao, H.L. Ho, W. Jin, S. Fan, S. Gao, Y. Wang, and P. Wang, "Mode-phase-difference photothermal spectroscopy for gas detection with an anti-resonant hollow-core optical fiber," Nat Commun. 11, 847 (2020).

6. H. Bao, W. Jin, Y. Hong, H. L. Ho, S. Gao, and Y. Wang, "Phase-modulation-amplifying hollow-core fiber gas sensing," J. Light. Technol. 40, 313–322 (2022).

7. T. Cai, P. Valecha, V. Tran, B. Engle, A. Stefanopoulou, and J. Siegel, "Detection of Li-ion battery failure and venting with Carbon Dioxide sensors," eTransportation, 7, 1-11 (2021).

8. P. Trefz, M. Schmidt, P. Oertel, J. Obermeier, B. Brock, S. Kamysek, J. Dunkl, R.

Zimmermann, J.K. Schubert, and W. Miekisch, “Continuous Real Time Breath Gas Monitoring in the Clinical Environment by Proton-Transfer-Reaction-Time-of-Flight-Mass Spectrometry,” Analytical chemistry (Washington). 85, 10321–10329 (2013).

9. D. G. Lancaster, D. Richter, R. F. Curl, and F. K. “Tittel, Real-time measurements of trace gases using a compact difference-frequency-based sensor operating at 3.5 μm,” Applied physics. B, Lasers and optics. 67, 339–345 (1998).

10. M. Born, “Principles of optics (Seventh (expanded) anniversary edition, 60th anniversary edition. ed.),” Cambridge: Cambridge University Press (2019).

11. A. M. Kowalevicz and F. Bucholtz, “Beam divergence from an SMF-28 optical fiber, photonics technology branch,” Optical Sciences Division, Naval Research Laboratory, Washington D.C., USA, Tech. Rep. NRL/MR/5650–06-8996, (2006).

12. A.W. Snyder, and J. Love, “Optical waveguide theory,” Springer Science & Business Media (2012).

13. C.N.T. Mori, and E.C. Romão, “Numerical simulation by FDM of unsteady heat transfer in cylindrical coordinates,” Applied Mechanics and Materials. 851, 322–325 (2016).

14. H. Kragh, “The Lorenz-Lorentz formula: origin and early history”, Substantia. 2, 7-18 (2018).

15. Y. Lin, W. Jin, F. Yang, J. Ma, C. Wang, H. L. Ho, and Y. Liu, “Pulsed photothermal interferometry for spectroscopic gas detection with hollow-core optical fibre,” Sci. Rep. 6, 1-12 (2016).

16. N. Ismail, C. Calil Kores, D. Geskus, and M. Pollnau, “The Fabry-Pérot resonator: Spectral line shapes, generic and related Airy distributions, linewidths, finesses, and performance at low or frequency-dependent reflectivity,” Optics Express. 24 16366-

16389 (2016).

17. H. Bao, Y. Hong, W. Jin, H.L. Ho, C. Wang, S. Gao, Y. Wang, and P. Wang, “Modeling and performance evaluation of in-line Fabry-Perot photothermal gas sensors with hollow-core optical fibers,” Opt. Express. 28, 5423–5435 (2020).

18. Y. Zhao, W. Jin, Y. Lin, F. Yang, and H.L. Ho, “All-fiber gas sensor with intracavity photothermal spectroscopy,” Opt. Lett. 43, 1566-1569 (2018).

19. Y. Zhao, Y. Qi, H.L. Ho, S. Gao, Y. Wang, and W. Jin, “Photoacoustic Brillouin spectroscopy of gas-filled anti-resonant hollow-core optical fibers,” Optica. 8, 532-538 (2021).

20. Y. Tan, W. Jin, F. Yang, Y. Jiang, and H.L. Ho, “Cavity-enhanced photothermal gas detection with a hollow fiber Fabry-Perot absorption cell,” Journal of Lightwave Technology. 37, 4222-4228 (2019).

21. F. Yang, W. Jin, Y. Cao, H.L. Ho, and Y. Wang, “Towards high sensitivity gas detection with hollow-core photonic bandgap fibers,” Opt. Express. 22, 24894-24907 (2014).

22. F. Yang, W. Jin, Y. Lin, C. Wang, H.L. Ho, and Y. Tan, “Hollow-core microstructured optical fiber gas Sensors,” Journal of Lightwave Technology. 35, 3413-3424 (2017).

23. F. Yang, Y. Tan, W. Jin, Y. Lin, Y. Qi, and H.L. Ho, “Hollow-core fiber Fabry–Perot photothermal gas sensor,” Opt. Lett. 41, 3025-3028 (2016).

24. Y. Tan, W. Jin, F. Yang, Y. Qi, C. Zhang, Y. Lin, and H.L. Ho, “Hollow-Core Fiber-Based High Finesse Resonating Cavity for High Sensitivity Gas Detection,” Journal of Lightwave Technology. 35, 2887-2893 (2017).

Chapter 4 Pump–probe-alternating PTS for two-component gas sensing

4.1 Introduction

HCF provides an efficient platform for strong light-gas interaction over a longer distance due to stronger light confinement in the hollow-core region surrounded by a micro-structured cladding [1-3]. With HCF as the gas cells, fiber optical PTS (FO-PTS) gas sensors have been used for single and multi-component gas sensing [4-6]. However, in conventional FO-PTS systems such as the one in [4], in addition to the pump lasers tuned to the specific absorption lines of the target gas species, an additional laser is used as the probe beam for PT phase detection.

In this chapter, we present an acetylene (C_2H_2)/methane (CH_4) gas sensing system based on FO-PTS with an alternating pump and probe technique. Two distributed-feedback (DFB) lasers are used in the proposed approach, which serve alternatively as the pump and probe beams respectively for the two gas components via time-division multiplexing (TDM), enabling the construction of a sensitive yet more cost-effective FO-PTS system. With a centimeter-long hollow-core conjoint-tube fiber (HC-CTF), noise-equivalent concentration (NEC) of 370 ppb and 130 ppb are achieved for CH_4 and C_2H_2, respectively.

4.2 Principle of the pump–probe-alternating technique

The pump-probe-alternating technique uses two lasers for two-component gas sensing. These two lasers (denoted as Laser1 and Laser2) act alternatively as the pump and probe beams respectively for the two gas components (denoted as Gas1 and Gas2) via time-division multiplexing. Specifically, when Laser1 is used as the pump absorbed by Gas1

to generate PT phase modulation, Laser2 is used as the probe to detect the phase modulation, and vice versa. More specifically, Laser1 used as the pump has its wavelength modulated and swept to be around the absorption line of Gas1, while Laser2 serving as the probe has its wavelength tuned away from the absorption lines of Gas2 and stabilized around the quadrature point.

4.3 Experimental setup

Figure 4.1 depicts the experimental setup. In the optical part, a 1533-nm (DFB1) and a1654-nm (DFB2) lasers, with linewidths of 1 MHz and 2 MHz, respectively, are served as the light sources, corresponding to the P (13) and R (3) absorption lines of C_2H_2 and CH_4, respectively. An erbium-doped fiber amplifier (EDFA) and a Raman fiber amplifier (RFA) are used to boost the optical power levels of DFB1 and DFB2, respectively. The two DFB lasers are alternately served as the pump and probe sources for the two gas components. Specifically, when DFB2 is used as the pump for CH_4 to generate PT phase modulation, DFB1 is used as the probe to detect the phase modulation, and vice versa. The pump and probe beams are combined by a wavelength-division multiplexer (WDM1) before launched into a low-finesse Fabry-Perot interferometer (FPI), which is formed by sandwiching a 2.5-cm-long HC-CTF between two thermally expanded core fibers (TECFs) [7-9]. The reflected beams from the FPI pass through WDM2, which separates the 1533-nm and 1654-nm beams. Only the probe beam passes through one of the two on-off optical switches (OSW1/OSW2) and is detected simultaneously by two photodetectors (PD1 and PD2).

In the electrical part, the AC component from PD1 is demodulated by a lock-in amplifier (LIA) to obtain the second harmonic component ($2f$) of the PT signal. The DC component from PD2 is used to generate servo control signal to stabilize operating point of the probe beam at a phase quadrature point of the FPI. Wavelength modulation and sweeping signal from the LIA and the function generator (FG), respectively, are

applied to the pump beam to generate PT phase modulation. The FG sends control signal (CTRL) to OSW1/OSW2, as well as the two single-pole double-throw electrical switches (ESW1 /ESW2).

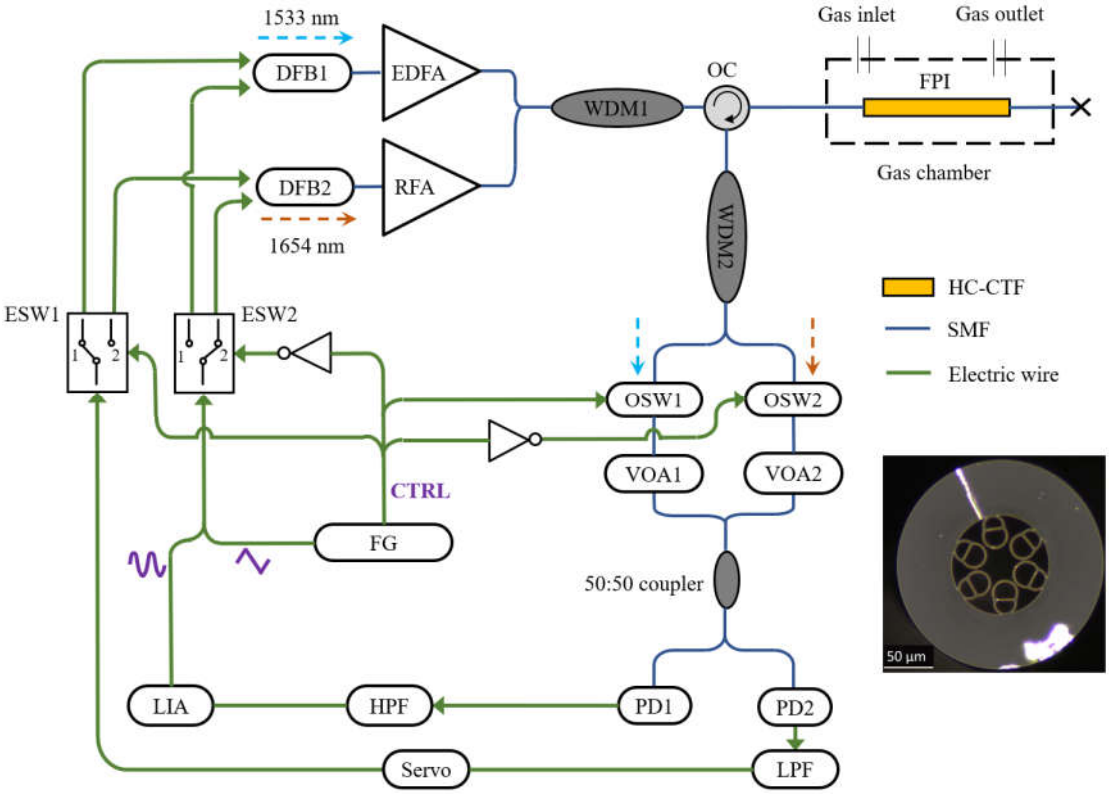

Figure 4.1 Schematic of the two-component gas detection system. SMF, single mode fiber. OC, optical circulator. VOA1 and VOA2, variable optical attenuators. HPF, high-pass filter. LPF, low-pass filter. The inset is the cross section of HC-CTF.

For CH_4 detection, DFB1 and DFB2 serve as the probe and pump beams, respectively. ESW1 is switched to port 1 so that the servo control signal is delivered to DFB1, with its wavelength (λ_{pr1}) tuned away from the absorption lines of C_2H_2 and stabilized around the quadrature point of the FPI fringes, as indicated in Figs. 4.2(a) and 2(c); at the same time, ESW2 is switched to port 2 to apply wavelength modulation and sweeping to DFB2 around the R (3) line of CH_4 to generate PT phase modulation. Simultaneously, OSW1 (OSW2) is on (off) to allow the probe beam from DFB1 to the photodetectors

for PT phase demodulation and for quadrature stabilization.

For C_2H_2 detection, DFB1 and DFB2 serve as the pump and probe beams, respectively. ESW1 (ESW2) is switched to port 2 (port 1). The servo control signal is delivered to DFB2, with its wavelength (λ_{pr2}) tuned away from the absorption line of CH_4 and stabilized around the quadrature point of the FPI fringes, as indicated in Figs. 4.2(b) and 2(d). Wavelength modulation and sweeping signal are delivered to DFB1 to generate PT phase modulation. OSW1 (OSW2) is off (on) to allow the probe beam from DFB2 to the photodetectors to detect the PT phase modulation.

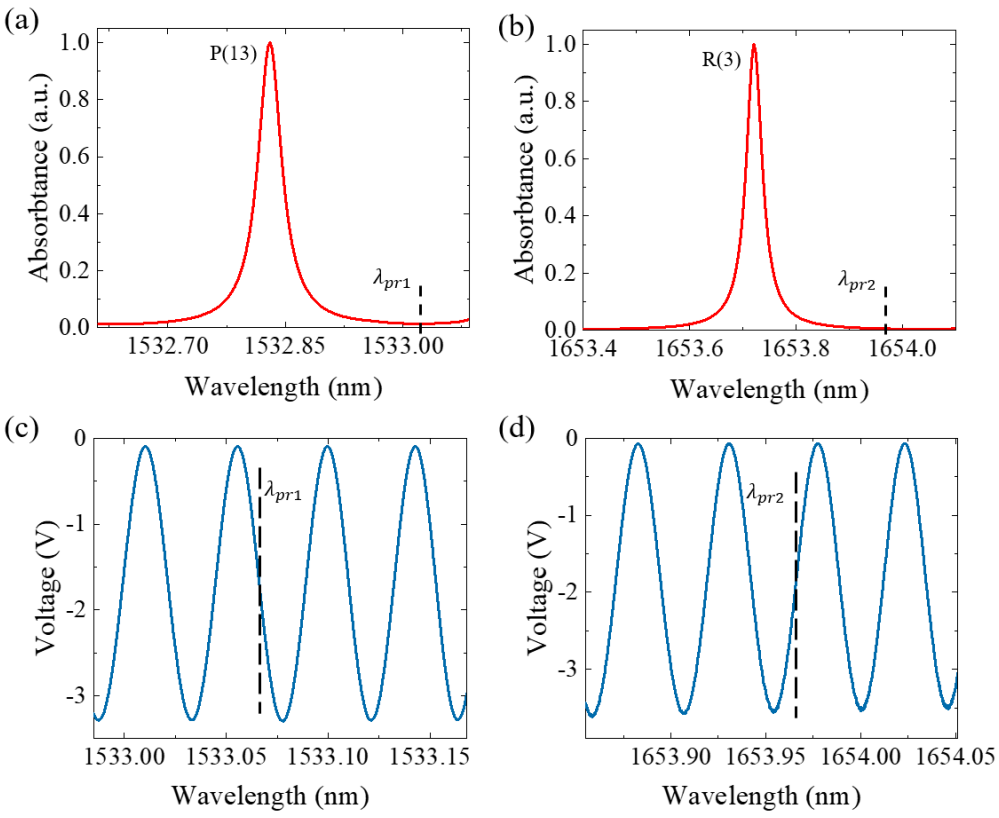

Figure 4.2 Stabilization of probe wavelengths to be away from the absorption lines and simultaneously around the quadrature point of the fringes. Calculated absorption spectra around (a) the P (13) absorption line of C_2H_2 and (b) the R (3) absorption line of CH_4 [10-11]. Measured interferometric fringes of the FPI (c) around λ_{pr1} with DFB1, and (d) around λ_{pr2} with DFB2.

4.4 Two-component gas detection

Experiments of two-component gas detection are conducted with the gas chamber filled with 500-ppm (parts per million) C_2H_2 and 5000-ppm CH_4 balanced with nitrogen (N_2). The pressure in the gas chamber is atmospheric pressure of ~1 bar. The laser power delivered to the FPI is ~400 mW at ~1533 nm and ~170 mW at ~1654 nm. The probe power (i.e., power accepted by PD1) is ~40 μW. The CTRL signal is of a rectangular waveform with a half period of 100 s and duty cycle of 50%. The low (0 V) and high (5 V) levels correspond to C_2H_2 and CH_4 detection, respectively, as shown in Fig. 4.3(a). The probe wavelength is stabilized at the quadrature point by servo control immediately after each switching action, as shown in Figs. 4.3(b-d). The second harmonic output ($2f$ = 4 kHz) as the pump wavelength tuned across the absorption line of the detected gas is demodulated by the LIA with time constant of 1 s, as shown in Fig. 4.3(e).

For example, consider the details of switching from C_2H_2 to CH_4 detection. At ~100 s, the CTRL signal is switched from low to high level, as shown in Fig. 4.3(a). ESW1 (ESW2) is switched to port 1 (port 2), so that DFB1 is immediately changed from the pump mode to the probe mode, while DFB2 from probe to pump mode. OSW1 (OSW2) is on (off) to allow only the 1533-nm probe beam to pass through and be delivered to PD1 and PD2. Synchronously, the wavelength of DFB2 is sinusoidally modulated at 2 kHz and swept across the R (3) line of CH_4 to generate the PT phase modulation, while the wavelength of DFB1 is changed from around the P (13) line of C_2H_2 to the preset value λ_{pr1} and then stabilized to the quadrature point around λ_{pr1} by servo control to detect the phase modulation. The time taken to stabilize the probe wavelength to quadrature is ~3.5 s, as shown in Fig. 4.3(c).

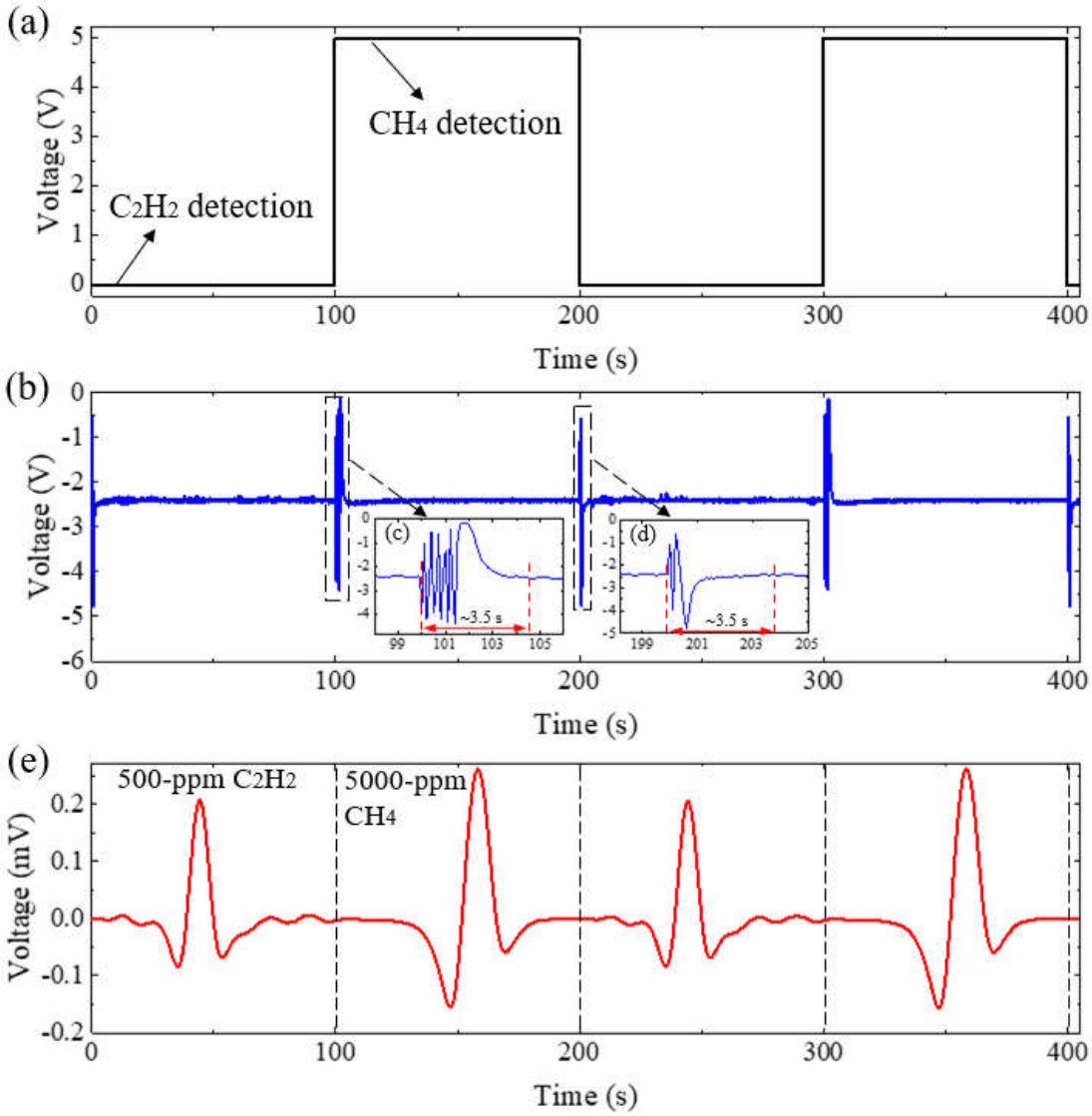

Figure 4.3 Two-component gas detection results with a pump-probe-alternating technique. (a) The "CTRL" signal waveform from the FG. (b) DC-component signal from PD2 during stabilization of the probe wavelength around the quadrature point. Inset: the zoom-in images for switching (c) from C_2H_2 to CH_4 detection and (d) from CH_4 to C_2H_2 detection. (e) The LIA 2*f*-signal of the two-component gas detection system.

Figure 4.4(a) shows the peak-to-peak (p-p) values of PT phase modulation signals at different pump power levels with the gas chamber respectively filled with 0.1% C_2H_2 and 1% CH_4 balanced with N_2. Approximately linear relationships are obtained for both

the C_2H_2 detection from 0 to 400 mW and the CH_4 detection from 0 to 200 mW. Figure 4.4(b) shows the p-p values of PT phase modulation signals for different C_2H_2 and CH_4 concentration. Approximately linear relationships are obtained for both the C_2H_2 detection from 10 ppm to 50% and the CH_4 detection from 100 ppm to 100%.

Allan deviation analysis is conducted to investigate the stability of the proposed time-division-multiplexed system. Allan plot of the baseline noise is recorded for 2 hours respectively with only OSW1 on (i.e., 1533-nm as the probe) or only OSW2 on (i.e., 1654-nm as the probe), as shown in Fig.4.4(c). The optimal averaging time τ is determined to be ~575 s for C_2H_2 detection and ~556 s for CH_4 detection, at which the noise levels are respectively 0.067 μV and 0.027 μV, corresponding NEC of ~130 ppb, and ~370 ppb for a signal-to-noise ratio (SNR) of unity.

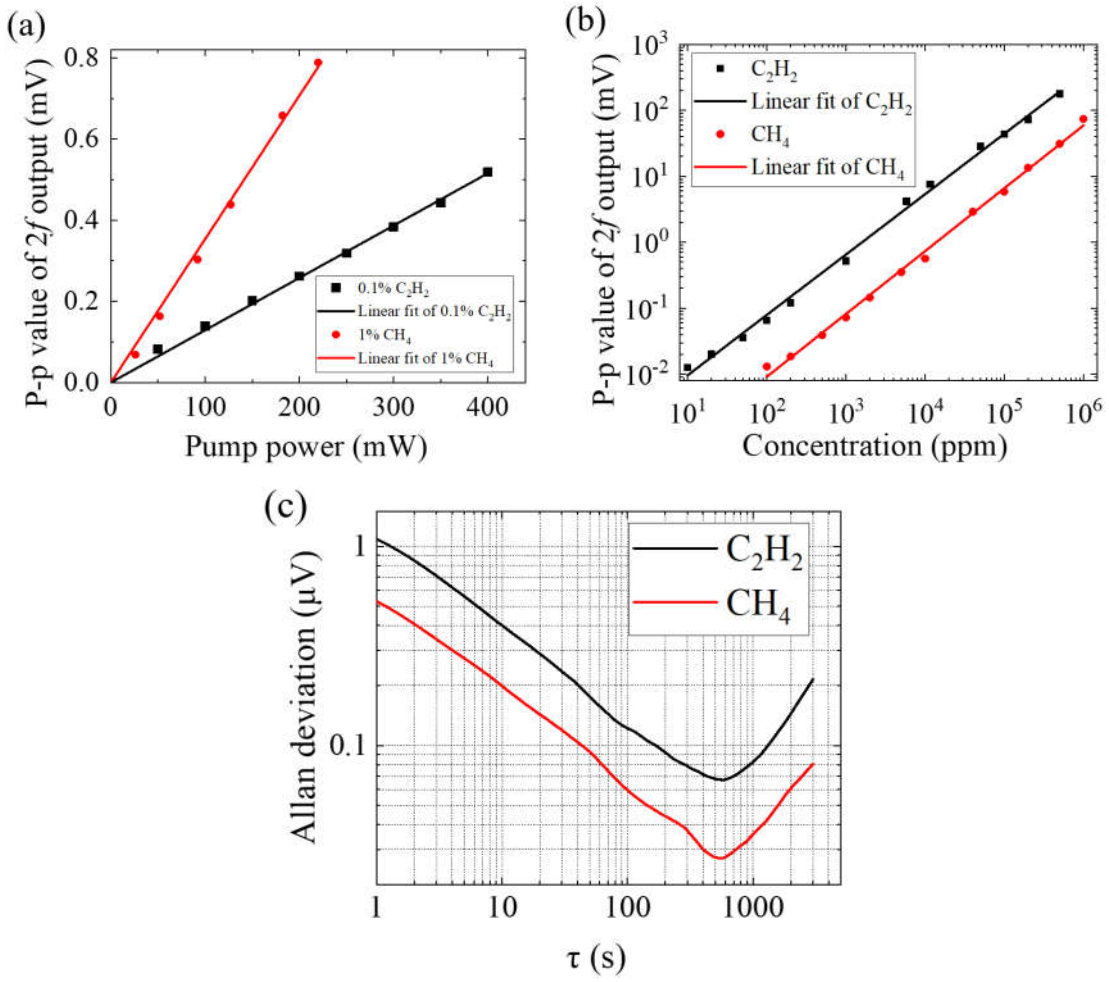

Figure 4.4 (a) Peak-to-peak (P-p) values of the 2*f* signal as functions of the pump power level for 0.1% C_2H_2 and 1% CH_4. (b) P-p values of the 2*f* signal as functions of gas concentration. The pump powers for C_2H_2 and CH_4 detection are ~400 mW and ~170 mW, respectively. (c) Allan deviation analysis of the baseline noise over a period of 2 hours when the gas chamber is filled with pure N_2.

4.5 Comparison with gas sensors using HCFs for multi-component detection

Table 4.1 summarizes the performances of some recently published optical fiber gas sensors based on PTS with HCFs for multi-component detection. These sensors use

HC-CTF or HC-ARF with near-infrared (NIR) or mid-infrared (MIR) lasers as the pump beam tuned to the specific absorption lines of the target gas species and an additional NIR laser as the probe beam for PT phase detection [4-5, 12]. The sensors in [5] and [13] are based on FDM, and need multi-frequency modulation and detection, leading to additional burdens on the LIA. The sensor presented here is based on TDM, and uses two NIR lasers serving alternatively as the pump and probe beams respectively, and hence doesn't need an additional laser. Compared to [4] based on TDM as well, the sensor in this work needs two optical switches to allow only the probe beam to pass through. It's straightforward to extend the technique to multi-gas component detection for both NIR and MIR sensing. Gas sensors integrating NIR and MIR lasers can be realized without additional mid-infrared detectors given that there are two NIR lasers which can be used alternatively as pump and probe beams, with one of them as a probe beam for all the rest of lasers.

Table 4.1. Performances of some recent gas sensors based on PTS with HCFs for multi-component detection.

Year	HCF type	Length/m	Technique	Wi/wo an additional laser	Detected gas	NEC/ppb	Averaging time/s
2021 [4]	HC-CTF	0.15	TDM	wi	C_2H_2	2	450
					CH_4	3.7	450
					NH_3	7	450
2022 [5]	HC-ARF	0.07	FDM	wi	C_2H_2	2.5	200
					CO_2	21000	400
					CH_4	200	200
2022 [12]	HC-ARF	0.13	FDM	wi	H_2O	222	1000
					CO_2	1.5	1000
					CO	0.6	1000
This work	HC-CTF	0.025	TDM	wo	C_2H_2	130	575
					CH_4	370	556

HC-ARF: hollow-core anti-resonant fiber, FDM: frequency division multiplexing.

4.6 Summary

In summary, we report a two-component gas sensor based on hollow-core fiber optical photothermal spectroscopy (FO-PTS) with a pump-probe-alternating technique. Only two lasers are required, instead of three, to detect two gas components by operating the lasers alternately as pump and probe beams via time-division multiplexing. A servo controller is used to tune the wavelength of the probe beam away from the absorption lines of the gas and simultaneously stabilize it at the quadrature point of interferometric fringes after each switching action. A gas sensor with a 2.5-cm-long HC-CTF demonstrates NEC of 370 ppb and 130 ppb for CH_4 and C_2H_2, respectively. The proposed PTS system is more cost-effective, making it attractive for a wide range of practical applications.

4.7 References

1. S. Gao, Y. Wang, W. Ding, D. Jiang, S. Gu, X. Zhang, and P. Wang, “Hollow-core conjoined-tube negative-curvature fibre with ultralow loss,” Nat. Commun. 9(1), 1–6 (2018).

2. A. R. Bhagwat and A. L. Gaeta, “Nonlinear optics in hollow-core photonic bandgap fibers,” Opt. Express. 16(7), 5035-5047 (2008).

3. F. Benabid, and P. J. Roberts, “Linear and nonlinear optical properties of hollow core photonic crystal fiber,” J. Mod. Opt. 58(2), 87–124 (2011).

4. F. Liu, H. Bao, H.L. Ho, W. Jin, S. Gao, and Y. Wang, “Multicomponent trace gas detection with hollow-core fiber photothermal interferometry and time-division multiplexing,” Opt. Express. 29(26), 43445-43453 (2021).

5. Z. Wang, H. Zhang, J. Wang, S. Jiang, S. Gao, Y. Wang, W. Jin, Q. Wang, and W. Ren, “Photothermal multi-species detection in a hollow-core fiber with frequency-division multiplexing,” Sensors and Actuators B: Chemical.369(132333), 1-6 (2022).

6. K. Krzempek, P. Jaworski, P. Kozioł, and W. Belardi, “Antiresonant hollow core fiber-assisted photothermal spectroscopy of nitric oxide at 5.26 μm with parts-per-billion sensitivity,” Sensors and Actuators B: Chemical. 345(130374), 1-10 (2021).

7. H. Bao, Y. Hong, W. Jin, H.L. Ho, C. Wang, S. Gao, Y. Wang, and P. Wang, “Modeling and performance evaluation of in-line Fabry-Perot photothermal gas sensors with hollow-core optical fibers,” Opt. Express. 28(4), 5423-5435 (2020).

8. F. Yang, Y. Tan, W. Jin, Y. Lin, Y. Qi, and H. L. Ho, “Hollow-core fiber Fabry–Perot photothermal gas sensor,” Opt. Lett. 41(13), 3025-3028 (2016).

9. S. L. Jiang, F. F. Chen, Y. Zhao, S. Gao, Y. Y. Wang, H. L. Hoi, and W. Jin,

"Broadband all-fiber optical phase modulator based on photo-thermal effect in a gas-filled hollow-core fiber," Opto-Electron Adv. 6, 220085 (2023).

10. R. E. Hachtouki, and J. V. Auwera, "Absolute line intensities in acetylene: the 1.5-μm region," Journal of Molecular Spectroscopy. 216(2), 355-362 (2002).

11. C. Frankenberg, T. Warneke, A. Butz, I. Aben, F. Hase, P. Spietz, and L. R. Brown, "Pressure broadening in the 2ν3 band of methane and its implication on atmospheric retrievals," Atmos. Chem. Phys. 8(17), 5061–5075 (2008).

12. F. Chen, S. Jiang, H.L. Ho, S. Gao, and Y. Wang, "Frequency-division-multiplexed multicomponent gas sensing with photothermal spectroscopy and a single NIR/MIR fiber-optic gas cell," Anal. Chem. 94, 13473–13480 (2022).

Chapter 5 Fiber-enhanced Fourier-transform PTS for multi-component gas sensing

5.1 Introduction

Multi-component gas identification and concentration detection play an important role in medical diagnosis, industrial process control and environmental monitoring [1-3]. Fiber-enhanced photothermal spectroscopy (FE-PTS) based on a hollow-core fiber (HCF) has proved to be a powerful technique to achieve high sensitivity and selectivity, and large dynamic range [4-6]. The FE-PTS technique employs a pump and probe configuration: pump absorption of gas molecules modulates the refractive index of the gas medium in the hollow-core via the so-called photothermal (PT) effect, which modulates the phase of a probe beam detectable with an optical fiber interferometer. Multi-component gas detection has been demonstrated with a single HCF gas cell and a single probe laser. By using multiple pump lasers tuned to the respective gas components, Liu et al. demonstrated the detection of methane, acetylene and ammonia based on time-division multiplexing, while Chen et al. reported the detection of water, carbon monoxide and carbon dioxide by using frequency division multiplexing [7-8]. We have recently reported the detection of acetylene and methane by using two lasers alternatively used as pump and probe, reducing the number of lasers for FE-PTS by one [9]. However, in general, the number of the required pump lasers increases as the number of the target gas species increases, making the multi-component FE-PTS system complex and expensive.

In this paper, we report a gas sensing technique named Fourier transform FE-PTS (FT-FE-PTS). It combines the features of the Fourier transform infrared spectroscopy and the FE-PTS, and requires only a single HCF absorption cell and one broadband light source covering the absorption spectra of multiple gas components. With a 10-

centimeter-long hollow-core conjoint-tube fiber (HC-CTF), we demonstrate the detection of two gas components, i.e., acetylene (C_2H_2) and carbon dioxide (CO_2).

5.2 Principle of Fiber-enhanced FT-PTS

Figure 5.1 depicts the principle of fiber-enhanced FT-PTS which can be divided into four blocks of generation of pump beam, generation of PT-phase spectrum, detection of PT-phase spectrum, and determination of gas components and concentration.

I. Generation of pump beam. A broadband light source (BLS) having a power spectrum of $P_{in}(v)$ with v the wavenumber is launched into a scanning two-beam interferometer (STBI). When the STBI scans with a constant velocity of optical path difference of $\tilde{V}$, the intensity of the output light beam from the STBI without considering the loss may be expressed as [10]

$$I_{out}(v) = 0.5I_{in}(v)(1 + cos2\pi\tilde{V}vt) \tag{5.1}$$

where $I_{in}(v)$ is the intensity of the BLS at v, and t is the time. According to (5.1), the light beam with the wavenumber of v will be modulated with a frequency as

$$f_m = \tilde{V}v \tag{5.2}$$

When the loss is considered, the output mean power of the light beam from the STBI may be expressed as

$$P_{pump}(v) = P_{in}(v)I_L(v) \tag{5.3}$$

where $I_L(v)$ is the loss spectrum of the STBI. Combining (5.1), (5.2) and (5.3), the instantaneous power may be expressed as

$$\tilde{P}_{pump}(v,t) = P_{pump}(v)W(v,t) \tag{5.4}$$

where $W(v,t)$ is the sinusoidal waveform with the modulation frequency related to the wavenumber according to (5.2) and may be expressed as

$$W(v,t) = 0.5 + 0.5\cos(2\pi f_m t) = 0.5 + 0.5\cos(2\pi \tilde{V} v t) \tag{5.5}$$

II. Generation of PT-phase spectrum. The generated pump beam $\tilde{P}_{pump}(v,t)$ is then launched into a gas-filled hollow-core fiber (HCF). When the pump spectrum covers the absorption lines of the target gas, the pump beam will be absorbed. Since only those beam that matches the absorption lines of the target gases can be absorbed, the absorbed pump power in the cross-section of the HCF under the assumption of weak absorption may be expressed as [11]

$$\tilde{P}_{abs}(v,t) = \sum_i^g \alpha_i(v) C_i \tilde{P}_{pump}(v,t) \tag{5.6}$$

where i denotes the i_{th} absorptive gas in the gas mixture with the total number of the absorptive gases of g, $\alpha_i(v)$ is the absorption coefficient of the i_{th} absorptive gas for a relative concentration of 100%, and C_i is the concentration of the i_{th} absorptive gas. After absorption of the pump beam, a heat source is generated via PT effect and may be expressed as

$$Q(r,\ t) = \int \tilde{P}_{abs}(v,t) I_p(r) dv \tag{5.7}$$

where r is the radial distance from the center of the beam, and $I_p(r)$ is the area-normalized intensity profile and equal to

$$I_p(r) = \frac{2}{\pi w_{pump}^2} exp\left(\frac{-2r^2}{w_{pump}^2}\right) \tag{5.8}$$

where w_{pump} is the mode field radius of the pump beam. The temperature distribution $T(r,\ t)$ within the hollow core may be obtained by solving the heat transfer equation [12]

$$\rho C_P \frac{\partial T(r,t)}{\partial t} = \nabla \cdot \left(\kappa \nabla T(r,\, t)\right) + Q(r,\, t) \tag{5.9}$$

where ρ is the density, C_P is the isobaric heat capacity, and κ is the thermal conductivity of the gas mixture. The local temperature distribution will modulate the refractive index (RI) change due to thermos-optic effect, which may be expressed as [13]

$$\Delta n(r,\, t) = -(n-1)\frac{T(r,t)-T_{amb}}{T_{amb}} \tag{5.10}$$

where n is the RI of the gas mixture and T_{amb} is the ambient temperature. When a probe beam enters the HCF, its phase modulation brought about by the RI distribution may be expressed as

$$\Delta\phi_{pr}(t) = 2\pi L v_{pr} \int \Delta n(r,\, t) \frac{2}{\pi w_{probe}^2} exp\left(\frac{-2r^2}{w_{probe}^2}\right) 2\pi r dr \tag{5.11}$$

where L is the absorption length, v_{pr} is the wavenumber of the probe beam and w_{probe} is the mode field radius of the probe beam. The phase change in radiofrequency (RF) domain, i.e., the PT-phase spectrum, can be obtained by Fourier transform of $\Delta\phi_{pr}(t)$ as

$$\Delta\Phi_{pr}(f_m) = \mathcal{F}\left[\Delta\phi_{pr}(t)\right] \tag{5.12}$$

III. Detection of PT-phase spectrum. The phase change $\Delta\phi_{pr}(t)$ of the probe beam can be demodulated by an interferometer [5], with the interference intensity change detected by a photodetector to collect the PT signal. After equal interval sampling of the PT signal, we can obtain an interferogram. After Fourier-transform of the interferogram, we can get the PT spectrum as $P_{pt}(f_m)$, which can be expressed as functions of the wavenumber as $P_{pt}(v)$ by using (5.2).

IIII. Determination of gas components and concentration. Full-spectrum analysis with

the linear least-squares (LLS) method for fitting is used to determine the gas components and concentration based on the reference spectra measured in advance, with the formula as [7]

$$\min_{x_1,x_2\ldots x_g} \sum_i^q \left(P_i - x_1 M_{1,i} - x_2 M_{2,i} - \cdots - x_g M_{g,i}\right)^2 \tag{5.13}$$

where i is the point number and q is the total number of points in the PT spectrum, P_i is the measured PT spectrum with the gas components and concentration to be determined, $M_{1,i}, M_{2,i} \cdots M_{g,i}$ are the measured reference spectra of single-component gas with known concentration, and $x_1, x_2 \cdots x_g$ are the fitted coefficients. $x_1, x_2 \cdots x_g$ represent the proportions of reference spectra and can be used to determine the gas components and concentration in the mixed gas.

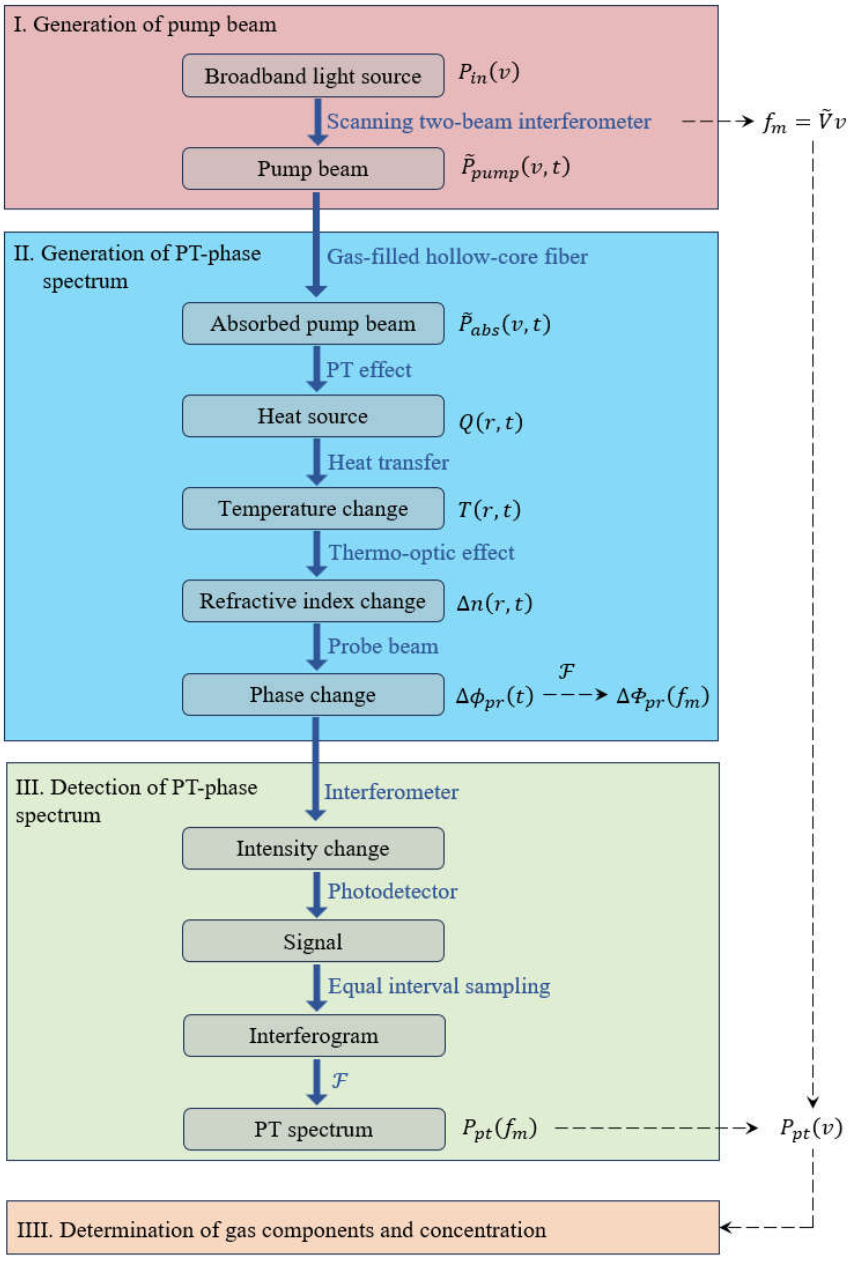

Figure 5.1. Principle of fiber-enhanced FT-PTS for gas sensing with four blocks.

In the following, the proposed technique will be applied in conjunction with specific examples for gas sensing.

5.3 Generation of pump beam

A pump beam is generated from an BLS which is detected by an optical spectrometer, as shown in Fig. 5.2(a). The wavenumber range of the BLS is from 6507 to 6523 cm^{-1} with the full width at half maximum (FWHM) of ~9 cm^{-1}, which covers a number of gases, such as acetylene (C_2H_2), ammonia (NH_3), and carbon dioxide (CO_2), etc., as shown in Fig. 5.2(b). The BLS is then launched into a scanning Michelson interferometer (SMI), with one arm formed by a fiber collimator and a movable mirror, and the other by a stable mirror, as shown in Fig. 5.2(c). When the movable mirror moves with a constant velocity of the optical path difference of $\tilde{V}$, the optical path difference between the beams that propagate in the two arms is $\delta = \tilde{V}t$. The output light from the SMI is used as the pump beam and launched into a gas-filled HCF. Here we use a 10-centimeter-long HC-CTF, which has a low-loss broadband from 5000 to 6600 cm^{-1}, covering the spectrum range of the BLS, as shown in Fig. 5.2(d).

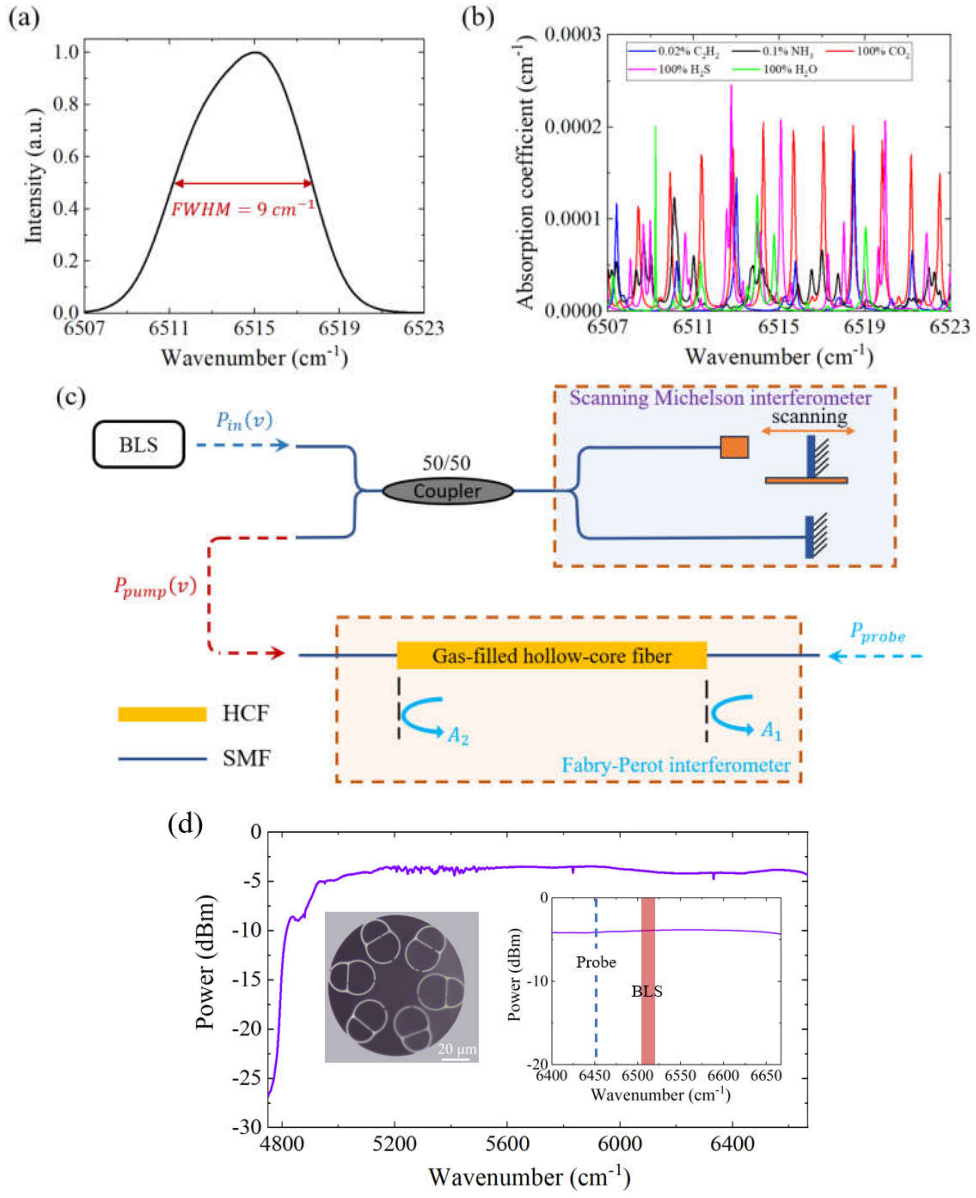

Figure 5.2. (a) Measured spectrum of the BLS with an optical spectrometer. (b) Calculated absorption coefficient of 0.02% C_2H_2, 0.1% NH_3, 100% CO_2, 100% H_2S and 100% H_2O from HITRAN database [14]. (c) Generation of the pump beam from the BLS through a scanning Michelson interferometer, and detection of the PT-phase modulation of the probe beam through a Fabry-Perot interferometer. (d) Spectral transmission of a 2-m-long HC-CTF, with its cross-section image on the left inset. The right inset is the spectral transmission to indicate the positions of the probe beam and the BLS.

5.4 Measurement and fitting of the pump beam

In order to acquire the absorbed pump power $\tilde{P}_{abs}(v,t)$ to establish the heat source for simulation according to (5.3) - (5-7), the power spectrum of the output light beam from the SMI is measured and fitted to match the wavenumber scale of the gas absorption lines.

Figure 5.3(a) depicts the experimental setup for measuring the pump spectrum with a SMI. The BLS and a reference source (RS) with the wavenumber of ~6623 cm^{-1} are combined through a wavelength-division multiplexer (WDM) and co-propagate into the interferometer. The SMI is constructed by two arms, with one arm formed by a scanning electrical delay line (EDL) and an optical fiber mirror (OFM1), and the other by the other OFM2. The maximum optical delay and the optical speed of the SMI are 20 cm and 1.5 cm/s, respectively. The output beams from the SMI pass through the WDM and are divided into the transmitted RS and the $P_{pump}(v)$, which are detected simultaneously by two photodetectors (PD1 and PD2), respectively, with the electrical signal collected by a data acquisition card (DAQ) and processed by a computer. The data acquisition rate of the DAQ is 200 kHz per channel. The interferogram of the pump signal is obtained by equal interval sampling through the RS signal with the sampling interval of 377.5 nm, as shown in Fig. 5.3(b). After Fourier transform of the interferogram, the output pump spectrum is obtained and fitted with a two-order Gaussian model, with R^2=0.9999, as shown in Fig. 5.3(c). The loss spectrum is calculated according to (5.3) and is nearly flat in the region of 6509-6519 cm^{-1} where the pump power mainly distributes, as shown in Fig. 5.3(d).

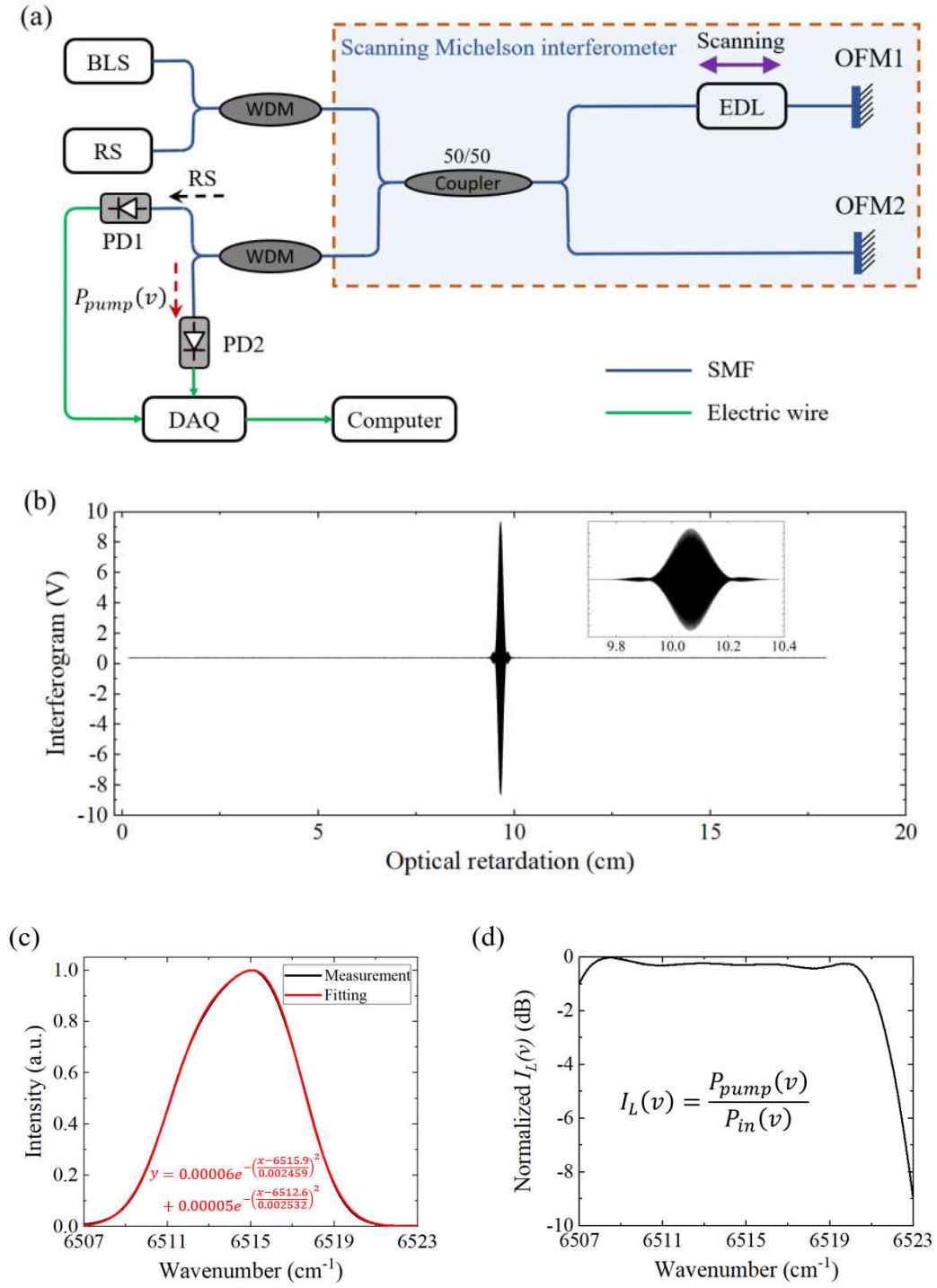

Figure 5.3. (a) Experimental setup for measuring the pump spectrum. (b) Interferogram of the pump signal after equal interval sampling. (c) Measured and fitted spectra of the pump spectrum. (d) Loss spectrum of the SMI.

5.5 Simulation of the generation of PT phase spectrum

A simplified model is used for the simulation of the generation of the PT phase spectrum by using COMSOL Multiphysics, as shown in the inset of Fig. 5.4(a). Based on (5.4) – (5.8), the fitting curve in Fig. 5.3(c) is used as $P_{pump}(v)$, and multiplied by the absorption lines of acetylene shown in Fig. 5.2(b) to acquire $\tilde{P}_{abs}(v,t)$, which is further multiplied by $I_p(r)$ and integrates over v to set up the heat source $Q(r,\ t)$ in the fluid region. After the simulation of heat transfer, the phase modulations are calculated from the temperature filed $T(r,\ t)$ to obtain an interferogram for acetylene detection according to (5.10) – (5.11), as shown in Fig. 5.4(a). Finally, the interferogram is Fourier-transformed to acquire the PT phase spectrum, as shown in Fig. 4(b).

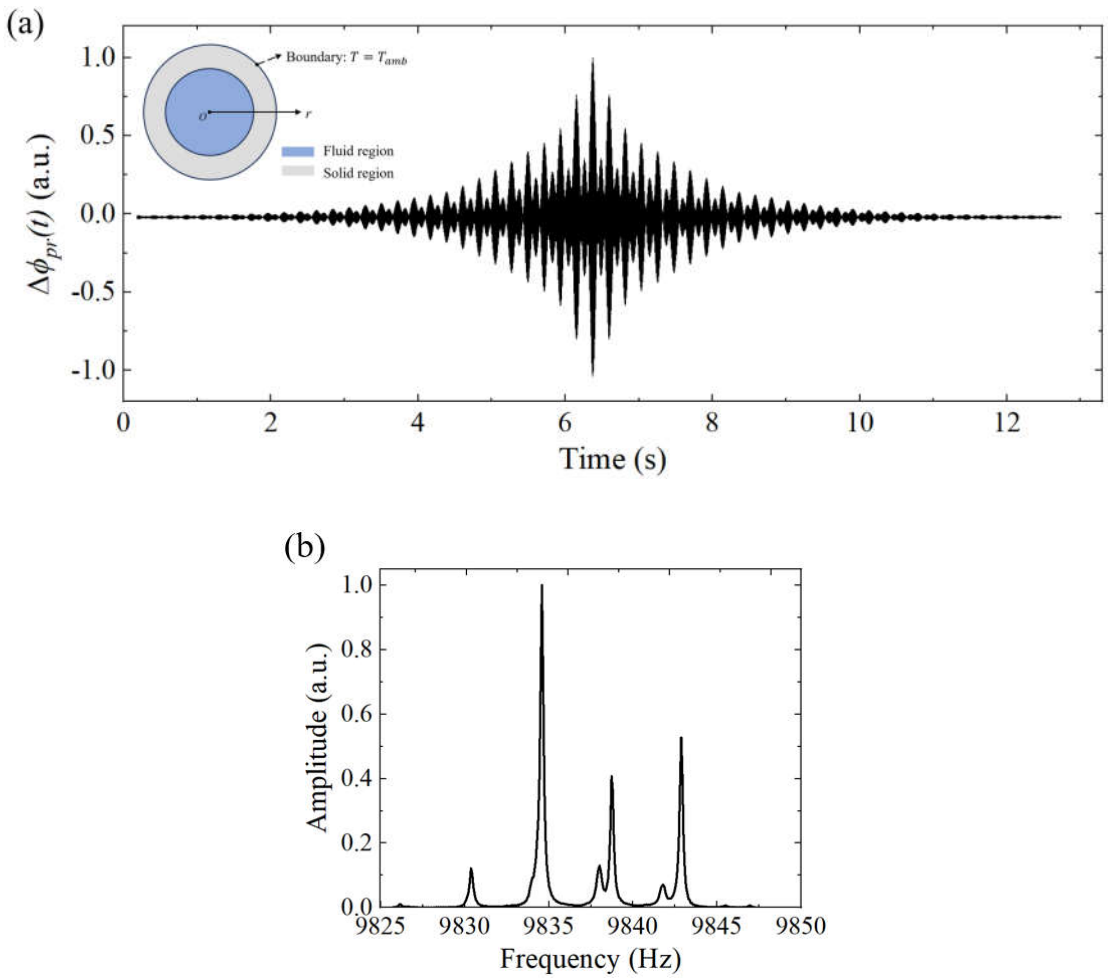

Figure 5.4. Simulation of the phase modulation of fiber-enhanced FT-PTS. (a) Interferogram of the phase modulation for acetylene detection. The inset is the simulation model. (b) Phase spectrum by Fourier transform of the interferogram shown in (a).

5.6 Detection of PT phase spectrum

The PT phase modulation of the probe beam is demodulated with a low-finesse Fabry-Perot interferometer (FPI), constructed by the HC-CTF sandwiched between two single-mode fibers (SMFs), with two reflected beams A_1 and A_2 from the cleaved ends of the two SMFs, as shown in Fig. 5.2(c). The wavenumber of the probe beam is ~6452 cm^{-1} and also located at the low-loss band of the HC-CTF, as shown in Fig. 5.2(d).

Figure 5.5 depicts the experimental setup for gas sensing based on the FT-PTS with an HCF. Different from Fig. 5.3(a) for the measurement of the pump beam, the generated pump beam is launched into the HCF filled with the target gas. The probe beam is launched into the HCF through an optical circulator (OC), with the reflected beams from the FPI and the residual pump beam filtered through a WDM. Only the reflected probe beams reach the coupler and are detected simultaneously by PD2 and PD3. The DC component from PD3 is used for stabilizing the operating point of the probe beam at a phase quadrature point of the FPI by a servo control. The AC component of the PT signal from PD2 and the electrical signal of the transmitted RS from PD1 are simultaneously launched into the DAQ to sample the interferogram and then analyzed by the computer.

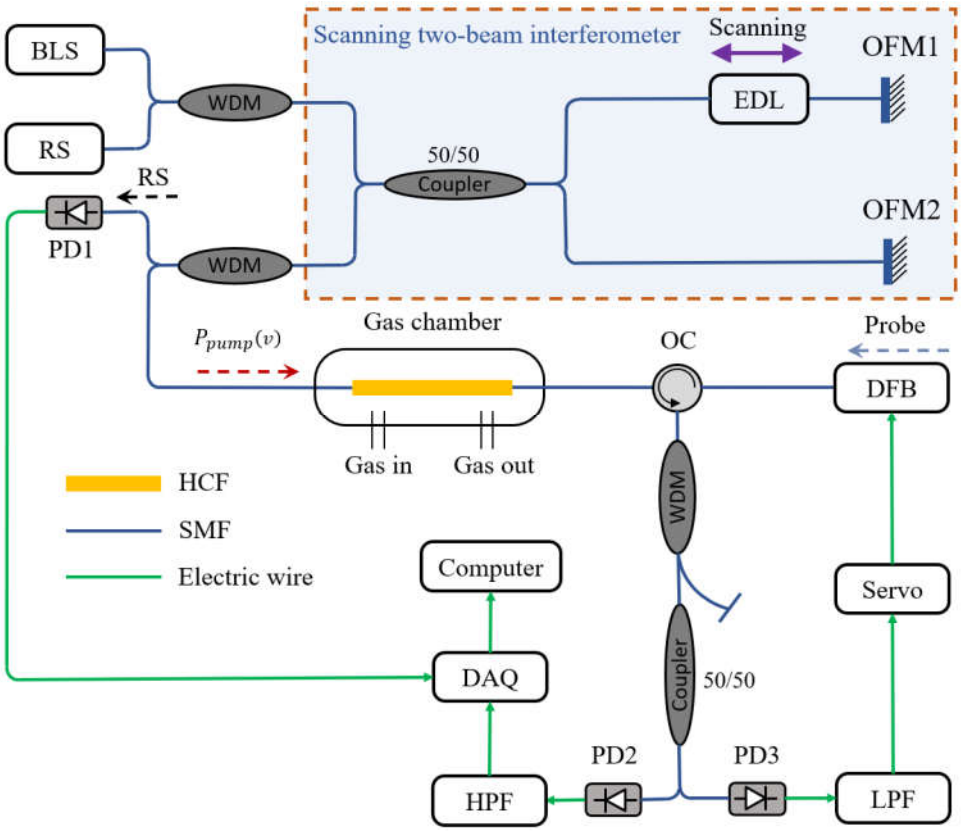

Figure 5.5 Experimental setup for gas sensing based on the FT-PTS with an HC-CTF. HPF: high-pass filter. LPF: low-pass filter.

5.7 Gas detection

5.7.1 Single-component gas detection of C_2H_2

Figure 5.6(a) shows the measured interferogram of the PT signal with the HC-CTF filled with 1000-ppm C_2H_2 balanced with N_2. The input pump power is ~45 mW. It should be noted that the input pump power means the average power directly launched into the HC-CTF. A PT spectrum is obtained by Fourier transform of the measured interferogram, as shown in Fig. 5.6(b). Figure 5.6(c) depicts an interferogram with the low-frequency components removed, which is obtained by inverse Fourier transform of the frequency components in the range of 9825-9850 Hz shown in the red dashed box of Fig. 5.6(b). The filtered interferogram in Fig. 5.6(c) have almost the same profile as the simulated interferogram shown in Fig. 5.4(a). The PT spectrum shown in the red dashed box of Fig. 5.6(b) is compared with PT phase spectrum from the simulation, as shown in Fig. 5.6(d). The measured and simulated spectra have almost the same profile and the same positions of the absorption peaks with the heights of the peaks corresponding to each other. Figure 5.6(e) shows the PT spectra for different C_2H_2 concentration from 200 to 1000 ppm. The measure PT spectrum of 1000-ppm C_2H_2 is used as the reference spectrum and denoted as of $M_{1,i}$ to calculate the fitting coefficients for the PT spectra of C_2H_2 with different concentrations from 200 to 1000 ppm according to (5.13), which can be written as $\min_{x_1} \sum_i^q \left[P_i - x_1 M_{1,i}\right]^2$ for single-component gas detection of C_2H_2. Figure 5.6(f) depicts the fitting coefficient x_1 as functions of the input C_2H_2 concentration, with an approximately linear relationship obtained for the C_2H_2 detection from 0 to 1000 ppm. Therefore, the solved concentration can be calculated as $C_1 = 1000x_1\ (ppm)$, and shown in Fig. 5.6(g) as functions of the input C_2H_2 concentration, which has an approximately linear relationship.

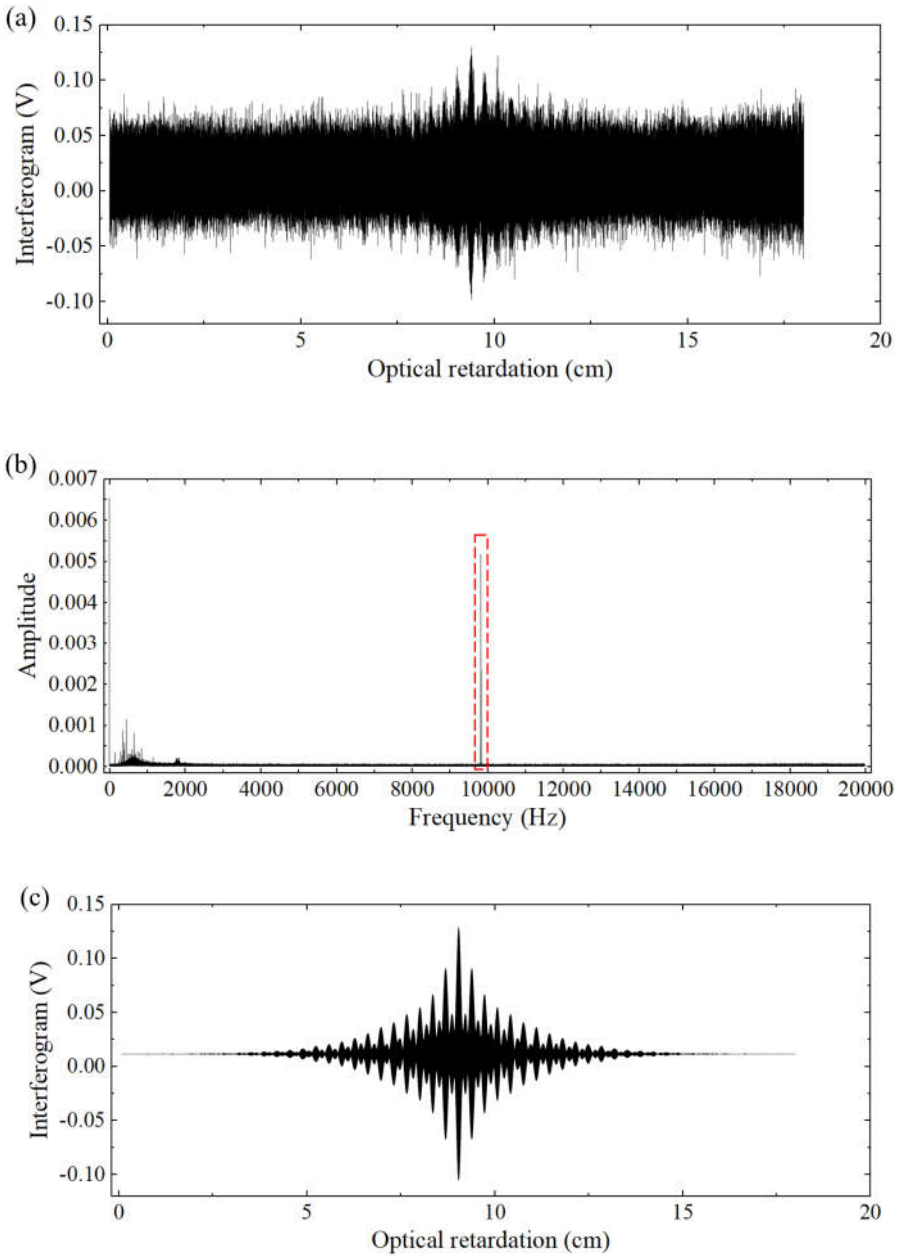
(a)
Interferogram (V)
0.15
0.10
0.05
0.00
-0.05
-0.10
0
5
10
15
20
Optical retardation (cm)
(b)
Amplitude
0.007
0.006
0.005
0.004
0.003
0.002
0.001
0.000
0
2000
4000
6000
8000
10000
12000
14000
16000
18000
20000
Frequency (Hz)
(c)
Interferogram (V)
0.15
0.10
0.05
0.00
-0.05
-0.10
0
5
10
15
20
Optical retardation (cm)

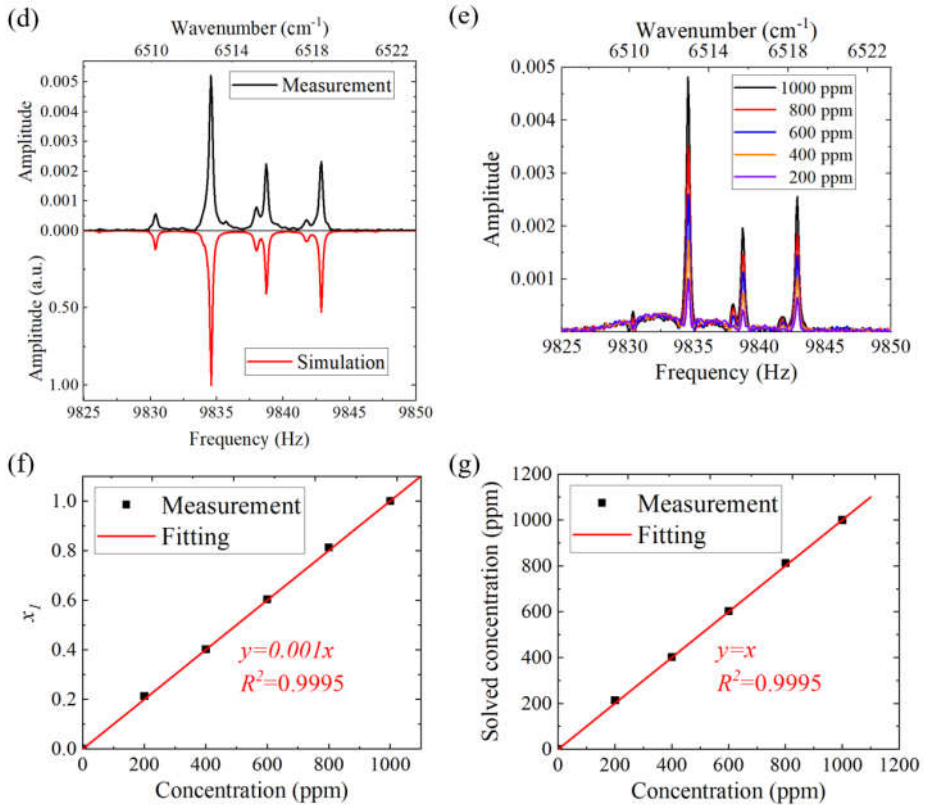

Figure 5.6. (a) The measured interferogram of the photothermal signal. The HCF is filled with 1000-ppm C_2H_2 balanced with N_2. (b) The measured PT spectrum by Fourier transform of the interferogram shown in (a). (c) The interferogram by inverse Fourier transform of the spectrum shown in the red dashed box of (b) with removal of the low-frequency components. (d) The measured PT spectrum by Fourier transform of the interferogram for 1000-ppm C_2H_2, and the simulated PT spectrum. (e) The measured PT spectra for different C_2H_2 concentration from 200 ppm to 1000 ppm. (f) The fitting coefficient x_1 and (g) the solved concentration as functions of the input C_2H_2 concentration with reference spectrum of 1000-ppm C_2H_2. The input pump power is ~45 mW. The buff gas is N_2.

5.7.2 Single-component gas detection of CO_2

Figure 5.7(a) shows the measured interferogram of the PT signal with the HC-CTF

filled with 100% CO_2. A PT spectrum is obtained by Fourier transform of the measured interferogram, as shown in Fig. 5.7(b). Figure 5.7(c) depicts an interferogram with the low-frequency components removed, which is obtained by inverse Fourier transform of the frequency components in the range of 9825-9850 Hz shown in the red dashed box of Fig. 5.7(b). The PT spectrum shown in the red dashed box of Fig. 5.7(b) is compared with PT phase spectrum from the simulation, as shown in Fig. 5.7(d). The measured and simulated PT spectra have almost the same profile and the same positions of the absorption peaks with the heights of the peaks corresponding to each other. Figure 5.7(e) shows the PT spectra for different CO_2 concentrations from 20% to 100% balanced with N_2. The measure PT spectrum of 100% CO_2 is used as the reference spectrum and denoted as of $M_{2,i}$ to calculate the fitting coefficients for the PT spectra of CO_2 with different concentrations from 20% to 100% according to (5.13), which can be written as $\min_{x_2} \sum_i^q \left[P_i - x_2 M_{2,i}\right]^2$ for single-component gas detection of CO_2. Figure 5.7(f) depicts the fitting coefficient x_2 as functions of the input CO_2 concentration, with a quadratic function relationship obtained for the CO_2 detection from 0 to 100%. Therefore, the solved concentration C_2 can be calculated by solving the equation

$$x_2 = 7.02 \times 10^{-5} C_2^2 + 0.00276 C_2 + 0.0118 \tag{5.14}$$

Figure 5.7(g) shows the solved concentration as functions of the input CO_2 concentration, which has an approximately linear relationship.

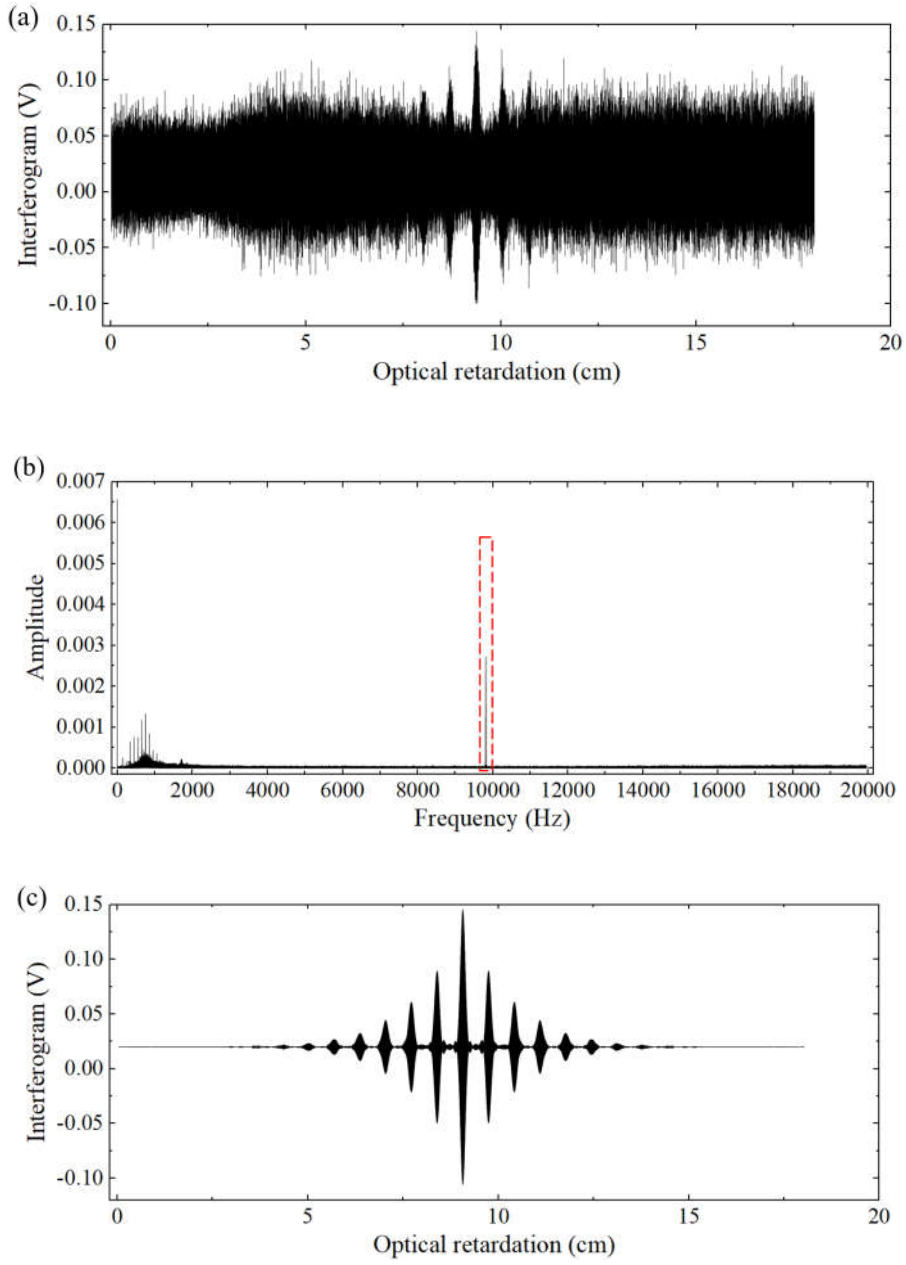
(a)
Interferogram (V)
0.15
0.10
0.05
0.00
-0.05
-0.10
0
5
10
15
20
Optical retardation (cm)
(b)
Amplitude
0.007
0.006
0.005
0.004
0.003
0.002
0.001
0.000
0
2000
4000
6000
8000
10000
12000
14000
16000
18000
20000
Frequency (Hz)
(c)
Interferogram (V)
0.15
0.10
0.05
0.00
-0.05
-0.10
0
5
10
15
20
Optical retardation (cm)

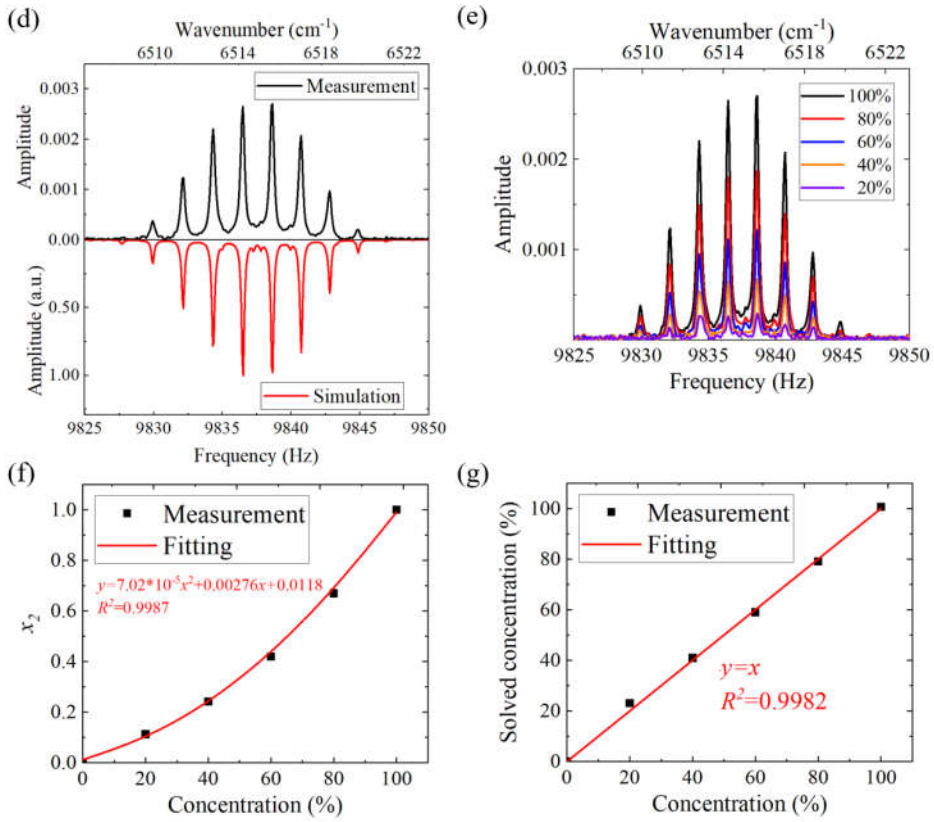

Figure 5.7. (a) The measured interferogram of the photothermal signal. The HCF is filled with 100% CO_2. (b) The measured PT spectrum by Fourier transform of the interferogram shown in (a). (c) The interferogram by inverse Fourier transform of the spectrum shown in the red dashed box of (b) with removal of the low-frequency components. (d) The measured PT spectrum by Fourier transform of the interferogram for 100% CO_2, and the simulated PT spectrum. (e) The measured PT spectra for different CO_2 concentration from 20% to 100%. (f) The fitting coefficient and (d) the solved concentration as functions of the input CO_2 concentration with reference spectrum of 100% CO_2. The input pump power is ~45 mW. The buff gas is N_2.

5.7.3 Two-component gas detection of C_2H_2 and CO_2

Figure 5.8(a) shows the absorption coefficient of 100% CO_2 and 200-ppm C_2H_2 with the buff gas of N_2 from HITRAN database [14]. The absorption lines of C_2H_2 have

strong overlaps with those of CO_2 at the range of the pump spectrum, especially between the absorption lines of P(17e) and R(12e), P(16e) and R(16e), as well as P(15e) and R(20e). It can be seen from the single-component gas detection of CO_2 that there exists a nonlinear relationship between the fitting coefficient and the input concentration under high CO_2 concentration, which may have effect on the detection of low-concentration C_2H_2 under high CO_2 concentration. Experiment with the gas chamber filled with a fixed C_2H_2 concentration of 200 ppm under different CO_2 concentration from 0 to 80% with the buff gas of N_2 is conducted to obtain the gain factor defined as

$$Gain\ factor = \frac{Fitting\ coefficient\ under\ CO_2 concentraion\ of C_2}{Fitting\ coefficient\ under\ buff\ gas\ of N_2} \tag{5.15}$$

The measured PT spectra are shown in Figure 5.8(b). Figure 5.8(c) shows the separated spectra of 200-ppm C_2H_2 under different CO_2 concentration through the spectrum of the gas mixture shown in Fig. 5.8(b) subtracting the corresponding spectrum of high-concentration CO_2 shown in Fig. 5.7(e). Figure 5.8(d) depicts the fitting coefficient x_1 as functions of the CO_2 concentration with the reference spectrum of 1000-ppm C_2H_2. An approximately linear relationship is obtained for a fixed C_2H_2 concentration of 200 ppm under different CO_2 concentration from 0 to 80%. The gain factor calculated according to (5.15) is thus $x_1/0.2$ and is $0.0092C_2 + 1$, meaning that 1% increase in the CO_2 concentration makes the PT modulation amplitude increase by ~0.92%.

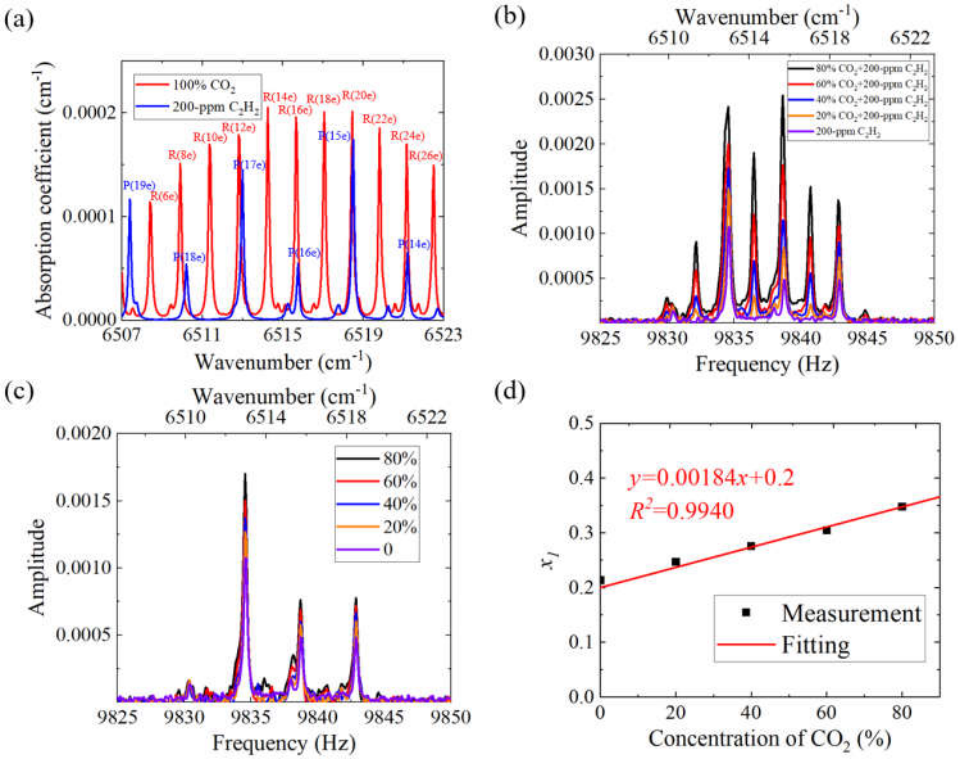

Figure 5.8. (a) Calculated absorption coefficient of 100% CO_2 and 200-ppm C_2H_2 from HITRAN database. (b) The measured PT spectrum with the HCF filled with a fixed C_2H_2 concentration of 200 ppm under different CO_2 concentration from 0 to 80%. (c) The calculated spectrum by subtracting the corresponding spectrum of high-concentration CO_2 shown in Fig. 5.7(e) from the spectrum of the gas mixture shown in (b). (d) The fitting coefficient of the C_2H_2 spectra in (c) as functions of the CO_2 concentration with the reference spectrum of 1000-ppm C_2H_2. The input pump power is ~45 mW. The buff gas is N_2.

For two-component gas detection of CO_2 and C_2H_2, (5.13) can be written as

$$\min_{x_1,x_2} \sum_i^q \left(P_i - x_1 M_{1,i} - x_2 M_{2,i}\right)^2 \tag{5.16}$$

By solving (5.16), x_2 is obtained and used to determine the concentration C_2 of CO_2 by using (5.14). The solved concentration C_2 is then used to determine the gain factor to solve the concentration of C_2H_2 as

$$C_1 = \frac{1000x_1}{0.0092C_2+1}\ (ppm) \tag{5.17}$$

A PT spectrum is obtained by filling the gas chamber with a gas mixture of 60% CO_2 and 400-ppm C_2H_2 with the buff gas of N_2, as shown in Fig. 5.9(a). The spectrum is fitted according to (5.16) with x_2 calculated to be ~0.435, corresponding to ~60.4% CO_2 by using (5.14), with the error of ~1%. x_1 is calculated be ~0.612, corresponding to ~394 ppm C_2H_2 by using (5.17), with the error of ~1.5%. The separated individual spectra for CO_2 and C_2H_2 from the gas mixture are shown in Fig. 5.9(a). The residual between the measured PT spectrum and the fitted spectrum by adding the fitted CO_2 spectrum with C_2H_2 spectrum is shown in Fig. 5.9(b).

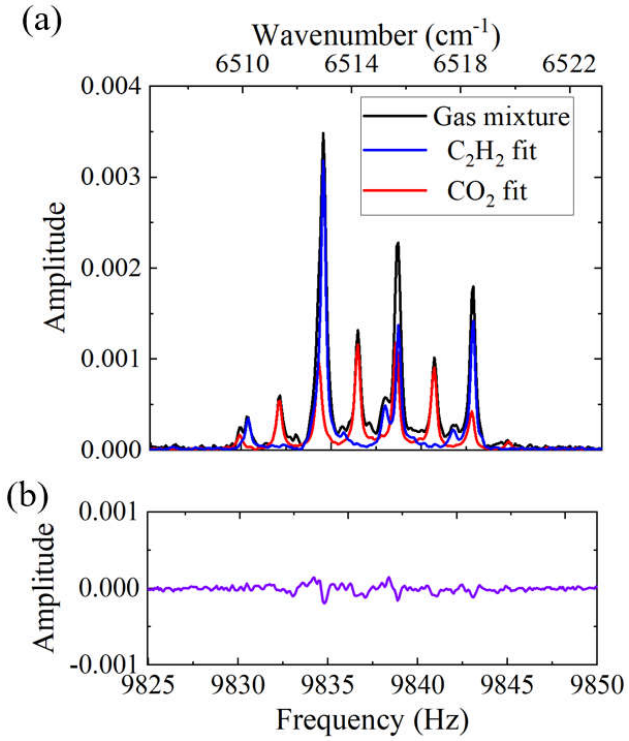

Figure 5.9. (a) The measured PT spectrum with the HCF filled with a gas mixture of 60% CO_2 and 400-ppm C_2H_2 and the fitted individual spectra for CO_2 and C_2H_2 from the gas mixture. (b) The residual between the measured PT spectrum and the fitted spectrum by adding the fitted CO_2 spectrum with C_2H_2 spectrum shown in (a). The input pump power is ~45 mW. The buff gas is N_2.

5.8 Discussion

It can be seen in Fig. 5.6(b) and Fig. 5.7(b) that the low-frequency waveband, especially those lower than 3 kHz, may bring about larger uncertainty and noise, which the measured PT spectrum in the range of 9825-9850 Hz is far away from. Ten repeated measurements of 1000-ppm C_2H_2 are conducted and fitted according to (5.13) with the reference spectrum of 1000-ppm C_2H_2, with a standard deviation of ~7 ppm obtained for the ten solved concentrations. The precision of the system may be calculated by the standard deviation of ~7 ppm divided by the input concentration of 1000 ppm and is ~0.7%. The noise-equivalent-concentration (NEC) may be calculated as the standard deviation of ten solved concentrations from ten repeated measurements by filling the gas chamber with pure N_2 and fitted according to (5.13). With the reference spectrum of 1000-ppm C_2H_2 and 100% CO_2, NECs of ~465 ppb and ~457 ppm are obtained for the detection of C_2H_2 and CO_2, respectively.

The nonlinear relationship between x_2 and C_2 in Fig. 5.7 and the gain factor for low-concentration C_2H_2 detection in Fig. 5.8 under high CO_2 concentration may be due to the change of the thermal properties and overall refractive index of the background gas medium. According to (5.10), $|\Delta n|$ increases as $(n-1)$ and ΔT increases. As shown in Table 5.1, the $(n-1)$ of CO_2 is ~1.5 times of that of N_2, which increases $|\Delta n|$, resulting in higher phase modulation. According to (5.9), the ρC_P of CO_2 is higher than that of N_2, which may make the temperature rise slower for the same $Q(r, t)$, but the κ of CO_2 is smaller, which allows slower heat dissipation and higher temperature rising. Considering that the gain factor increases by ~2 times from 0 to 100% CO_2 for the detection of 200-ppm C_2H_2, the combination of the factors ρC_P and κ may also lead to higher ΔT, and hence larger $|\Delta n|$ and phase modulation. Both the thermal properties and overall refractive index of the background gas of high-concentration CO_2 can cause larger $|\Delta n|$ and thus larger phase modulation.

Table 5.1. Thermal properties of N_2 and CO_2 at 300 K and 1 bar [15-16], and RI thereof at 6452 cm^{-1} [17].

Properties	ρC_P [J/(m^3·K)]	κ [W/(m·K)]	$n-1$
N_2	1.165	0.026	0.00029
CO_2	1.499	0.017	0.000438

Some conditions on how to realize an HCF-enhanced FT-PTS system may be summarized as: (1) The low-loss transmission band of the HCF should cover the wavenumbers of the pump and probe beams; (2) The scanning velocity of the STBI should be high enough to keep away from the low-frequency waveband but should match the frequency response of the phase modulation of the HCF to ensure high phase modulation efficiency. For the HC-CTF used here, the -3dB roll-off frequency is ~50 kHz and has a nearly flat response until 10 kHz [18].

5.9 Summary

In summary, we report a gas sensor based on HCF-enhanced FT-PTS. A broadband light source passing through a scanning two-beam interferometer with its light intensity modulated at different frequencies for different wavenumbers is used as the pump beam and launched into the HCF gas cell. A probe beam is used to detect the PT phase modulation through the PTS method. With a 10-cm-long HC-CTF, NECs of ~465 ppb and ~457 ppm are achieved for the detection of C_2H_2 and CO_2, respectively. The system is used to demonstrate two-component gas detection of C_2H_2 and CO_2. The proposed method enables the PTS system for multi-component gas detection with a compact size.

5.10 References

1. D. Smith, and P. Španěl, “The challenge of breath analysis for clinical diagnosis and therapeutic monitoring,” Analyst. 132, 390–396 (2007).

2. Q. Wang, Z. Wang, T. Kamimoto, Y. Deguchi, S. Cao, D. Wen, and D. Takahara, “Muti-species hydrocarbon measurement using TDLAS with a wide scanning range DFG laser,” Spectrochimica Acta Part A: Molecular and Biomolecular Spectroscopy, 265, 120333 (2022).

3. P. Laj, J. Klausen, M. Bilde, C. Plaß-Duelmer, G. Pappalardo, C. Clerbaux, U. Baltensperger, J. Hjorth, D. Simpson, S. Reimann, P.-F. Coheur, A. Richter, M. De Mazière, Y. Rudich, G. McFiggans, K. Torseth, A. Wiedensohler, S. Morin, M. Schulz, J.D. Allan, J.-L. Attié, I. Barnes, W. Birmili, J.P. Cammas, J. Dommen, H.-P. Dorn, D. Fowler, S. Fuzzi, M. Glasius, C. Granier, M. Hermann, I.S.A. Isaksen, S. Kinne, I. Koren, F. Madonna, M. Maione, A. Massling, O. Moehler, L. Mona, P.S. Monks, D. Müller, T. Müller, J. Orphal, V.-H. Peuch, F. Stratmann, D. Tanré, G. Tyndall, A. Abo Riziq, M. Van Roozendael, P. Villani, B. Wehner, H. Wex, and A.A. Zardini, “Measuring atmospheric composition change. Atmos,” Environ. 43, 5351–5414 (2009).

4. S. Gao, Y. Wang, W. Ding, D. Jiang, S. Gu, X. Zhang, and P. Wang, “Hollow-core conjoined-tube negative-curvature fibre with ultralow loss,” Nat. Commun. 9(1), 1–6 (2018).

5. W. Jin, Y. Cao, F. Yang, and H. L. Ho, “Ultra-sensitive all-fibre photothermal spectroscopy with large dynamic range,” Nat. Commun. 6, 1-8 (2015).

6. P. Zhao, Y. Zhao, H. Bao, H.L. Ho, W. Jin, S. Fan, S. Gao, Y. Wang, and P. Wang, “Mode-phase-difference photothermal spectroscopy for gas detection with an anti-resonant hollow-core optical fiber,” Nat Commun. 11, 847 (2020).

7. F. Liu, H.H. Bao, H.L. Ho, W. Jin, S.F. Gao, and Y.Y. Wang, “Multicomponent trace gas detection with hollow-core fiber photothermal interferometry and time-division multiplexing,” Optics Express. 29, 43445-43453 (2021).

8. F. Chen, S. Jiang, H.L. Ho, S. Gao, and Y. Wang, “Frequency-division-multiplexed multicomponent gas sensing with photothermal spectroscopy and a single NIR/MIR fiber-optic gas cell,” Anal. Chem. 94, 13473–13480 (2022).

9. L. H. Guo, P. C. Zhao, H. L. Ho, S. L. Jiang, H. H. Bao, S. F. Gao, Y. Y. Wang, and W. Jin, “Pump–probe-alternating photothermal interferometry for two-component gas sensing,” Opt. Lett. 48, 6440-6443 (2023).

10. P. R. Griffiths, J. A. De Haseth, and J. D. Winefordner, “Fourier Transform Infrared Spectrometry,” Wiley (2007).

11. G. Stewart, “Laser and fiber optic gas absorption spectroscopy,” Cambridge University Press (2021).

12. C.N.T. Mori, and E.C. Romão, “Numerical simulation by FDM of unsteady heat transfer in cylindrical coordinates,” Applied Mechanics and Materials. 851, 322–325 (2016).

13. H. Kragh, “The Lorenz-Lorentz formula: origin and early history,” Substantia. 2, 7-18 (2018).

14. I.E. Gordon, L.S. Rothman, R.J. Hargreaves, et al, “The HITRAN2020 molecular spectroscopic database,” Journal of Quantitative Spectroscopy and Radiative Transfer. 277, 1-82 (2022).

15. D. R. Lide, “CRC Handbook of Chemistry and Physics: A ready-reference book of chemical and physical data,” CRC Press, Boca Raton (2004).

16. L. V. Gurvich, I. V. Veyts, and C. B. Alcock, “Thermodynamic Properties of Individual Substances”, Hemisphere, New York. 4th ed., Vols. 1-2 (1989).

17. https://refractiveindex.info

18. Y.Z. Hong, "Performance enhancement of fiber optic photothermal interferometry for gas sensing," PhD Thesis, Hong Kong Polytechnic University (2023).

Chapter 6 PTS with HCFs for phase modulators

6.1 Introduction

Optical phase modulators (PMs) play an important role in optical communication, sensing, and coherent beam combining [1]. Compared to traditional electrically driven optical PMs, all-optical PMs use a control beam to modulate the phase of a signal beam [2]. Among the various all-optical PMs, fiber-based PMs have the advantage of smaller size, easier to construct and connect into optical fiber systems [3]. In recent years, two-dimensional (2D) materials, including black phosphorus (BP), transition metal dichalcogenides (TMDs), graphene, antimonene and MXenes, have been studied for all-optical fiber PMs [4-10]. These materials were coated onto tapered microfibers (MFs) or D-shaped fibers, allowing the evanescent field of the control beam to interact with the materials to modulate the phase of a co-propagating signal beam through nonlinear optical effect or photothermal (PT) effect of the materials. However, the manufacture and the transfer processes of 2D materials are complex and unreliable, leading to imperfect deposition of the materials onto the fibers. In addition, evanescent field of the signal beam is also absorbed by the materials, leading to high insertion loss (IL) over a broad wavelength band. Fiber-based PMs with 2D materials also have the problem of long response time.

In this chapter, we explore the application of PTS with HCFs for phase modulators. Phase modulation of the PM is realized by gas absorption of a control beam to generate heat via the PT effect, which modulates the refractive index (RI) of the gas medium and hence the accumulated phase of a signal beam propagating through the HCF. A broadband all-fiber optical PT PM can be achieved by using an acetylene-filled hollow-core fiber (HCF) with low IL and fast response [11]. We study the effect of varying gas (acetylene) concentration, buffer gases, HCF length and transverse microstructure on

the PT phase modulation, which enables better understanding of the modulation process to optimize the PM performance.

6.2 Principle of PM based on PTS with HCFs

Figure 6.1 depicts an HCF-based optical PM, showing the parameters that could be varied to optimize its performance. The HCF is filled with a mixture of absorptive gas and buffer gas. The pressure of the gas mixture in the HCF is 1 atm. The absorptive gas absorbs the control beam via PT effect, which generates heat and modulates the temperature and hence the RI distribution of the gas mixture. With appropriate gas concentration and HCF length, the configuration can be applied as a phase modulator for a signal beam copropagating in the HCF. The signal beam is free from the absorption of the gas as well as the solid fiber materials, because its wavelength is kept away from the gas absorption line and most of its optical mode power propagates in the hollow core. The performance of the PM is affected by concentration of the absorptive gas (i.e., C_2H_2), the buffer gas, the length and cross section of the HCF. Two HCFs with different cross-sections are considered here, a hollow-core anti-resonant fiber (HC-ARF) with a mode field radius of ~22 μm and a hollow-core photonic bandgap fiber (HC-PBGF) with a mode field radius of ~4.5 μm.

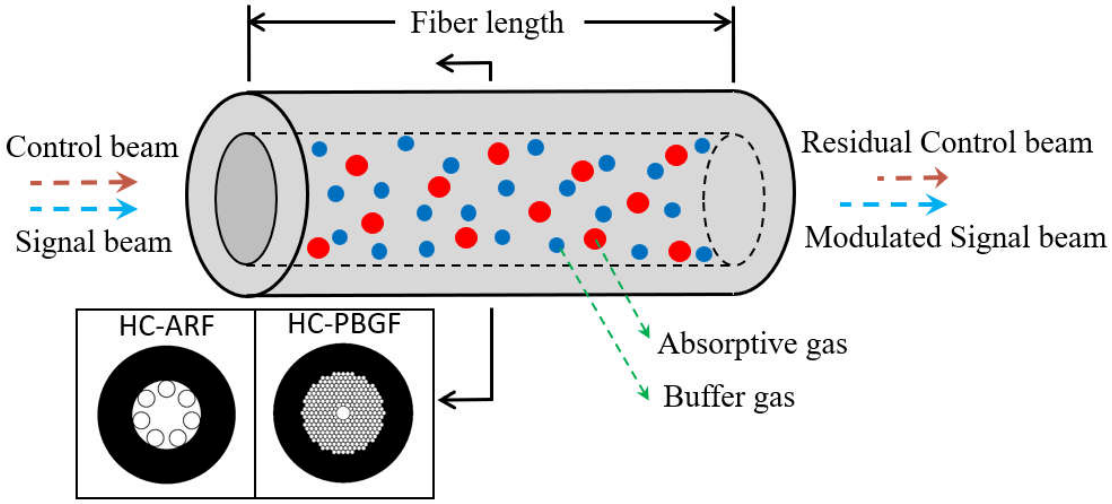

Figure 6.1 Basics and parameters of PM with a gas-filled HCF. The insets are cross-sections of HC-ARF and HC-PBGF, respectively.

6.3 Experimental setup

Figure 6.2(a) shows the experimental setup to characterize the PM. The gas-filled HCF is placed in one arm of a Mach-Zehnder interferometer (MZI) made of standard single mode fibers (SMFs). The control beam is from a distributed feedback (DFB) laser with its wavelength fixed at the center of the P (9) absorption line of C_2H_2 at 1530.371 nm. An acoustic optical modulator (AOM) and erbium-doped fiber amplifier (EDFA) are used to modulate and amplify the control beam, respectively. The control beam is sinusoidally modulated with a function generator (FG) via the AOM. 1% of control light power (P_{ctrl}) is directed to an optical power meter (OPM1) to monitor the power level of the pump. In the experiment, the wavelength of the signal beam is fixed at 1550 nm. However, the PM could operate over a broad range of signal wavelengths from 1480 to 1640 nm, as has been demonstrated previously [11]. The control and signal beams are combined by the wavelength-division multiplexer (WDM) before launched into the HCF. A second WDM is used after the HCF to separate the signal and residual control beam that is fed into a second optical power meter (OPM2) to monitor the

absorbance of control beam. A compensation fiber (CF) is used to match the optical path lengths of two arms of the MZI to minimize the effect of laser phase noise [12]. A polarization controller (PC) and a variable optical attenuator (VOA) are used to adjust the polarization state and equalize the power levels of the signal beams of the two arms to maximize the interference contrast.

The fiber MZI is quite sensitive to environmental disturbance, such as temperature and vibration, and the output detected from the photodetector (PD2) fluctuates significantly, as shown in Fig. 6.2(b) as the red line. By using the low frequency component to servo control a piezoelectric transducer (PZT), the MZI is phase stabilized around the quadrature point [13], as shown in Fig.6.2(b) as the blue line. The standard deviation (std) of phase fluctuation is 0.04° after servo control is applied, as shown in Fig. 6.2(c). With the MZI stabilized at the quadrature point, the phase modulation of the signal beam can be conveniently determined by examining the interference waveform from PD1, which is displayed on an oscilloscope (OSC) [11].

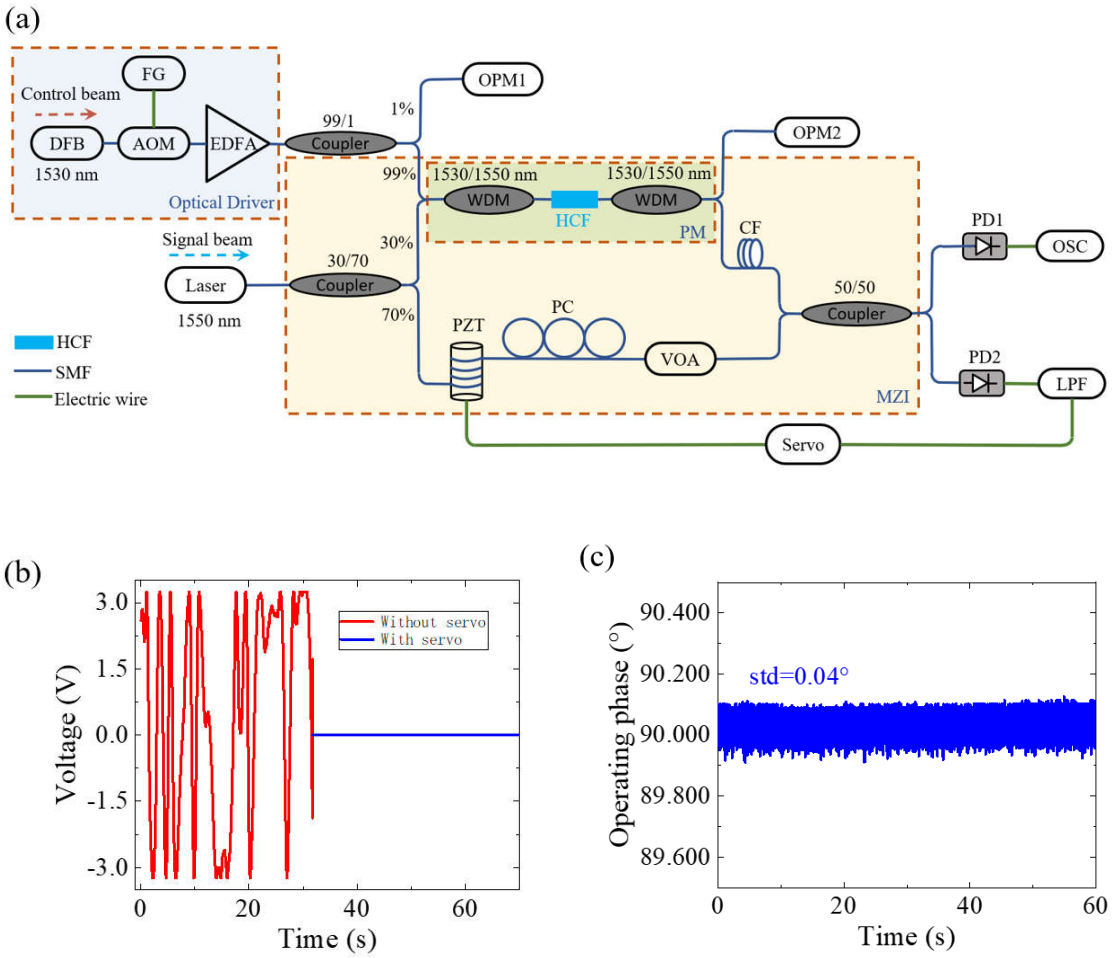

Figure 6.2 (a) Experimental setup for characterizing the PM. LPF, low-pass filter. (b) Voltage output from the MZI (PD2) with and without servo control. (c) Operating phase of the MZI with phase stabilization, where phase fluctuation is stabilized around the quadrature point.

6.4 Results and discussion

We first study the effect of buffer gas on the PT phase modulation. A 23-cm-long HC-ARF was filled with 5% C_2H_2 balanced respectively by argon (Ar), nitrogen (N_2) and helium (He). The HC-ARF is butt-coupled to thermally expanded core fibers (TECFs) at both ends, and the total insertion loss (IL) of the PM, defined as the ratio of the light power emergent from the second WDM (i.e., measured by OPM2) over the power

incident into the first WDM (i.e., measured by OPM1) when the hollow-core fiber is filled with air, is measured to be ~2 dB, primarily due to joint losses, which could be reduced to below 1 dB by the mode field matching [11]. Fig. 6.3 shows the measured amplitude of phase modulation for a control modulation frequency of 100 kHz, as a function of control power level P_{ctrl}. It should be noted that P_{ctrl} is the average power into HCF estimated from the measurement of OPM1 and by deducting the IL (~1 dB) of the input joint. The PT phase modulation is the largest for Ar as buffer gas, which is ~1.3 times larger than N_2, and ~4 times higher than He. The difference may be due to different thermal properties and RI of the buffer gases. After absorbing the same control beam, the heat generation Q is approximately the same for buffer gases. Considering that the thermal conduction is the dominant process, the temperature distribution T of the HCF may be determined from [14]

$$\rho C_P \frac{\partial T}{\partial t} = \nabla \cdot (\kappa \nabla T) + Q \tag{6.1}$$

where ρ is the density, C_P is the isobaric heat capacity, and κ is the thermal conductivity of the gas mixture. The RI change Δn may be expressed as [15]

$$\Delta n = -(n-1)\frac{\Delta T}{T_0} \tag{6.2}$$

where n is the RI of the gas mixture, ΔT is the temperature change and equal to $(T - T_0)$ and T_0 is the initial temperature. $|\Delta n|$ increases as n and ΔT increases. As shown in Table 6.1, Ar and He have the same ρC_P, but κ of He is higher, allowing faster heat dissipation and hence smaller heat accumulation, leading to lower ΔT. Besides, n of He is smaller than Ar, which further reduces $|\Delta n|$, resulting in smaller phase modulation. Ar and N_2 have almost the same RI, but κ of Ar is smaller, allowing slower heat dissipation. ρC_P of Ar is smaller as well, meaning higher temperature rise for the same Q. Both factors result in higher ΔT, hence larger $|\Delta n|$ and phase modulation.

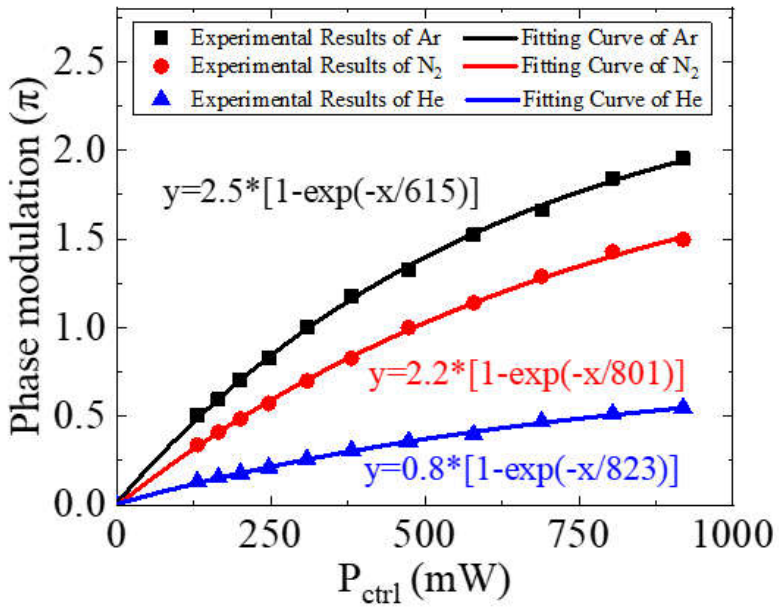

Figure 6.3 Phase modulation as a function of P_{ctrl} for a 23-cm-long HC-ARF filled with 5% C_2H_2 in different buffer gases of Ar, N_2 and He. The modulation frequency is 100 kHz.

Table 6.1. Thermal properties of gases at 300 K and 1 bar [16-17], and RI thereof at 1.55 μm [18].

Properties	Ar	N_2	He	C_2H_2
ρC_P [J/(m^3·K)]	0.832	1.165	0.832	1.768
κ [W/(m·K)]	0.0179	0.026	0.157	0.0214
n	1.00028	1.00029	1.000035	1.00055

From now on, we use Ar as the buffer gas and study the influence of varying C_2H_2 concentration and HCF length on the PT phase modulation. Three PMs were fabricated

using HC-ARFs with lengths of 10 cm, 15.5 cm, and 23 cm. The IL of these PMs is ~2 dB. Absorbance, defined as the ratio of the absorbed control power over P_{ctrl}, and phase modulation amplitude were measured for different C_2H_2 concentrations, and shown in Figs. 6.4(a) and (b), respectively. It should be noted that the absorbed control power is the difference between P_{ctrl} and the residual power which is the average power out of HCF estimated from the measurement of OPM2 and by deducting the IL (~1 dB) of the output joint.

For a fixed length of HCF, the absorbance increases with C_2H_2 concentration, following the asymptotic exponential relationship, as shown in Fig. 6.4(a). It reaches approximately a constant level for concentration higher than 30%, and the maximum absorbance for the HCFs with lengths of 10 cm, 15.5 cm, and 23 cm are 97.5%, 99.9% and 100%, respectively. For a fixed gas concentration, the absorbance is higher for a longer length of HCF.

For a fixed C_2H_2 concentration, the phase modulation increases with HCF length, as shown in Fig. 6.4(b). For C_2H_2 concentration higher than 30%, the difference in the PT phase modulation amplitude for the 15.5-cm and 23-cm long HCFs becomes small and approaches zero at 100%. For a fixed HCF length, the phase modulation amplitude firstly increases and then reduces with C_2H_2 concentration. The peak phase modulation is achieved at 12.5%, 17.5% and 50% concentration for 23-, 15.5- and 10-cm-long HCFs, respectively. The gas concentration corresponding to the peak phase modulation decreases with HCF length. The existence of modulation peak may be explained by considering the effects of heat generation and dissipation. Take the 23-cm-long HC-ARF as an example. For C_2H_2 concentration lower than 12.5%, the absorbed control power increases quickly with concentration, resulting in fast increase of gas temperature and hence the PT phase modulation. When the concentration is higher than 12.5%, the absorption approaches saturation, further increasing in gas concentration does not increase the total absorbed control power but cause re-distribution of the power

absorbed along the HCF, with the gas near the input end of the HCF absorbing more control power, resulting in higher local temperature near the input end. However, local high temperature increases thermal conductivity, which in turn reduces the temperature change, leading to reduced phase modulation [16]. Therefore, for a fixed HCF length, there exists an appropriate gas concentration to achieve maximum phase modulation.

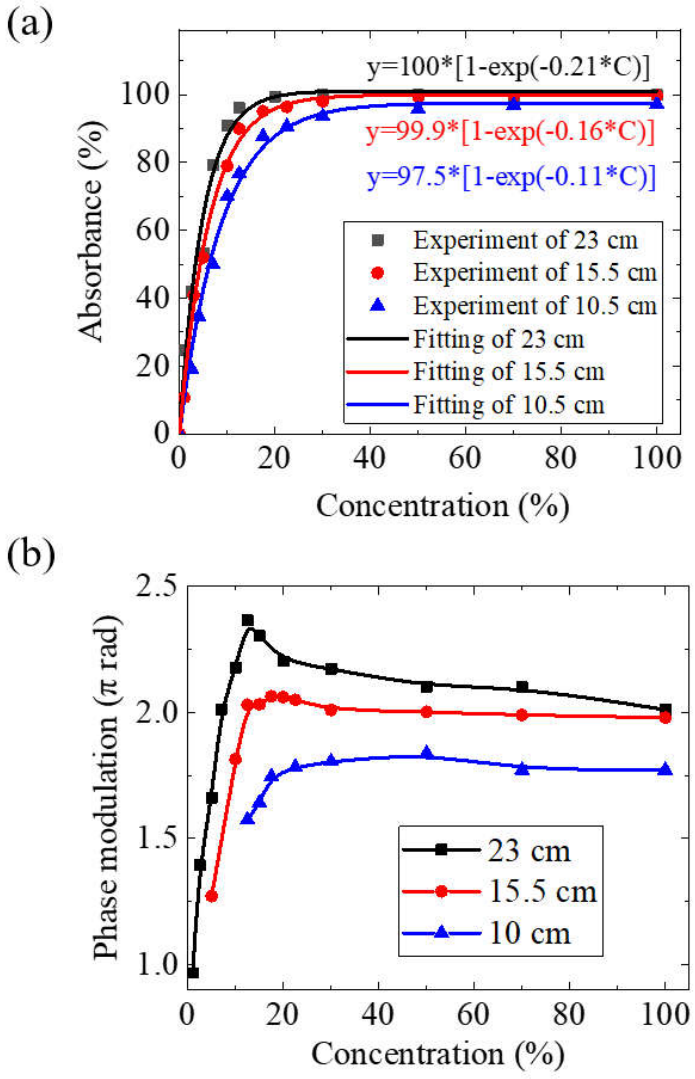

Figure 6.4 (a) Absorbance and (b) phase modulation amplitude as a function of C_2H_2 concentration for three PMs using HC-ARFs with lengths of 10 cm, 15.5 cm and 23 cm. The buffer gas is Ar. The modulation frequency is 100 kHz. P_{ctrl} is 675 mW. C: concentration of C_2H_2.

Figure. 6.5(a) shows the PT phase modulation as a function of control power level (black squares) for a 23-cm-long HC-ARF filled with 12.5% C_2H_2 in Ar. For a modulation frequency of 100 kHz, π-rad phase modulation is achieved with control power of ~200 mW. This power level is ~25% lower than that reported previously where a 5.6-cm-long HC-ARF is filled with pure C_2H_2 and 270 mW control power is needed to achieve π-rad phase modulation [11]. The frequency response of the PM is shown in Fig. 6.5(b) as the black squares. The -3dB bandwidth is ~ 150 kHz. For the PM made of a 23-cm-long hollow-core fiber and ~2-m-long single-mode fiber with control light power of ~200 mW, the Kerr-induced signal is calculated to be in the level of sub-mrad, much smaller than the π-rad phase modulation obtained from the photo-thermal effect and thus can be ignored [19].

Further investigation was carried out with a PM made of 23-cm-long HC-PBGF filled with 12.5% C_2H_2 buffered with Ar. The HC-PBGF is butt- coupled to SMFs at both ends and the total IL is ~5.5 dB, which could be reduced to less than 1 dB by the mode field matching [20]. The modulation performance is shown in Figs. 6.5(a) and 6.5(b) as the red dots. To achieve π-rad modulation at 100 kHz, this PM requires the control power (P_{ctrl}) of ~480 mW. The -3dB modulation bandwidth of the PM using HC-PBGF is ~1.1 MHz, significantly higher than that of HC-ARF, as shown in Fig. 6.5(b).

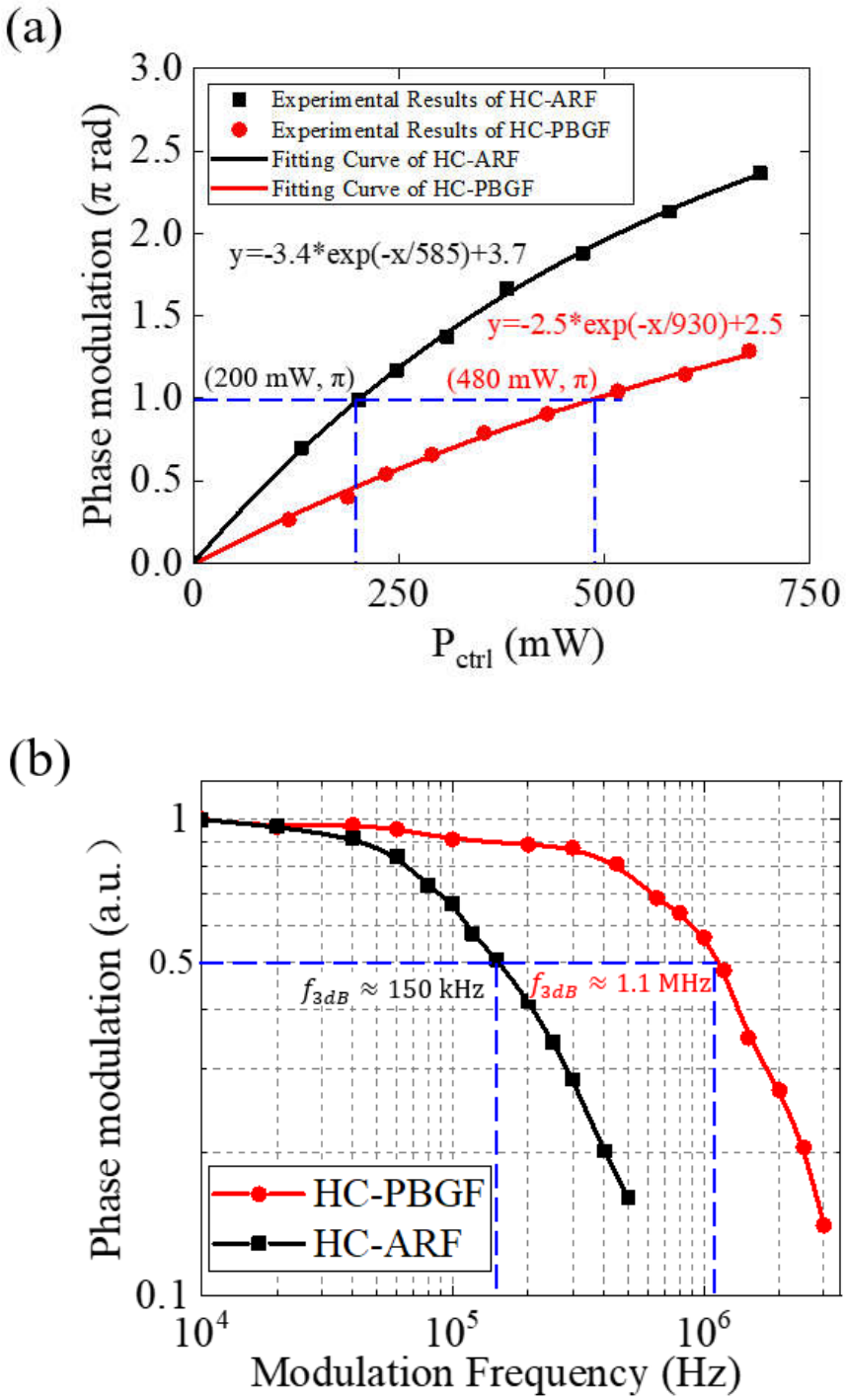

Figure 6.5 Comparison of the modulation performance between two samples based on HC-PBGF and HC-ARF. The two HCFs have the same length of 23 cm, and filled with 12.5% C_2H_2 in buffer gas of Ar. (a) Phase modulation as a function of P_{ctrl} for modulation frequency of 100 kHz. (b) Frequency response with P_{ctrl} of 150 mW.

The PBG-PM is further tested with square pulses with frequency of 200 kHz and duty cycle of 50%. The response of the PM is shown in Fig. 6.6. The 10-90% rise and fall time of the PM are respectively 0.57 μs and 0.55 μs, one order of magnitude smaller than those of HC-ARF of ~7.7 μs and ~8.1 μs [11].

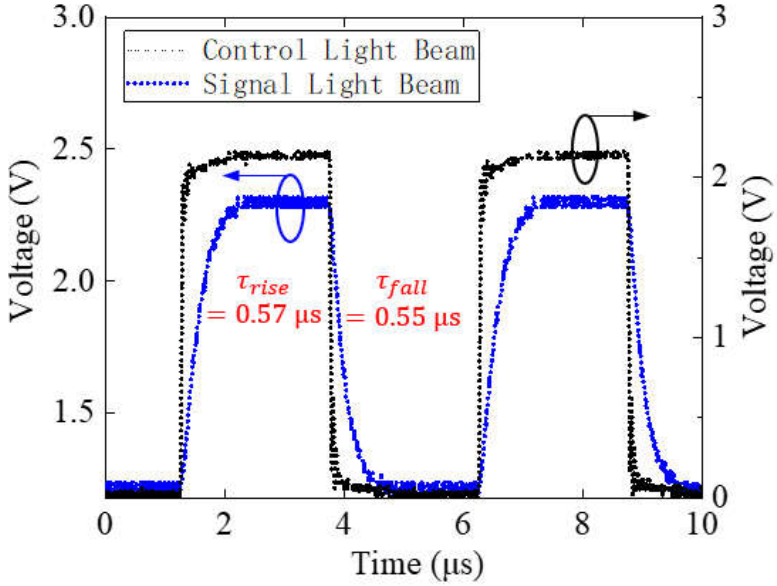

Figure 6.6 Response of the PT phase modulation with the HC-PBGF to square control pulses with pulse width of 2.5 μs.

The different modulation bandwidth and rise and fall time of the HC-PBGF and HC-ARF PM are believed to be due to different cross sections of the fibers and thus different effective heating dissipation radii, which are estimated to be 32 μm and 6.3 μm, respectively [13]. HCF with smaller effective heating dissipation radius may be regarded as to have smaller heat resistance and thus shorter rise and fall time, or a higher -3dB roll-off frequency, which may be analogous to an electrical low-pass filter with the cutoff frequency inversely proportional to the resistance. Under the assumption of a single-pole low-pass electrical filter, the 10-90% rise time is calculated to be ~0.32 μs from the -3dB bandwidth of ~1.1 MHz, smaller than the measured rise time, indicating that the heat accumulation and dissipation process inside the HCF may be

more complex and could not be evaluated with a single-pole low-pass RC filter and further research is needed.

6.5 Summary

In summary, we study the modulation performance of PMs based on HCFs filled with C_2H_2 of different concentration balanced with buffer gases of Ar, N_2 and He. The largest phase modulation is achieved with C_2H_2 balanced with Ar. For HCF with a fixed length, there exists an optimal gas concentration to achieve maximum phase modulation. With a 23-cm-long HC-ARF filled with 12.5% C_2H_2 balanced with Ar, we demonstrate phase modulation of π-rad at 100 kHz with control light power of ~200 mW. The -3dB modulation bandwidth is ~150 kHz. By using a HC-PBGF of the same length and gas concentration, we achieved -3dB modulation bandwidth of ~1.1 MHz, the highest among all the reported fiber-based all-optical PMs to our knowledge. The measured rise and fall time of HC-PBGF-based sample are 0.57 μs and 0.55 μs, respectively, one order of magnitude smaller than that based on the HC-ARF.

6.6 References

1. I. Fsaifes, L. Daniault, S. Bellanger, M. Veinhard, J. Bourderionnet, C. Larat, E. Lallier, E. Durand, A. Brignon, and J.-C. Chanteloup, "Coherent beam combining of 61 femtosecond fiber amplifiers," Opt. Express. 28, 20152-20161 (2020).

2. X. Zhang, M. Belal, G. Y. Chen, Z. Song, G. Brambilla, and T. P. Newson, “Compact optical microfiber phase modulator,” Opt Lett. 37, 320-322 (2012).

3. M. Zhang, Q. Wu, H. Chen, Z. Zheng, and H. Zhang, “Fiber-based all-optical modulation based on two-dimensional materials,” 2D Mater. 8, 1 (2020).

4. H. Yang, Y. Wang, Z. C. Tiu, S. J. Tan, L. Yuan, and H. Zhang, “All-Optical

Modulation Technology Based on 2D Layered Materials," Micromachines (Basel). 13(1), 92 (2022).

5. Y. Meng, Y. Zhao, C. Hu, H. Cheng, Y. Hu, Z. Zhang, G. Shi, and L. Qu, "All-Graphene Core-Sheath Microfibers for All-Solid-State, Stretchable Fibriform Supercapacitors and Wearable Electronic Textiles," Adv. Mater. 25(16), 2326-2331 (2013).

6. J. C. Shin, W. G. Kwak, and Y.-G. Han, "Temperature-Insensitive Microfiber Mach–Zehnder Interferometer for Absolute Strain Measurement," Journal of Lightwave Technology. 34(19), 4579-4583 (2016).

7. M. Liu, R. Tang, A.-P. Luo, W.-C. Xu, and Z.-C. Luo, "Graphene-decorated microfiber knot as a broadband resonator for ultrahigh-repetition-rate pulse fiber lasers," Photonics Research (Washington, DC). 6(10), C1 (2018).

8. Y. Wang, X. Gan, C. Zhao, L. Fang, D. Mao, Y. Xu, F. Zhang, T. Xi, L. Ren, and J. Zhao, "All-optical control of microfiber resonator by graphene's photothermal effect," Appl. Phys. Lett. 108, 171905 (2016).

9. Y. Wang, W. Huang, C. Wang, J. Guo, F. Zhang, Y. Song, Y. Ge, L. Wu, J. Liu, J. Li, and H. Zhang, "An All-Optical, Actively Q-Switched Fiber Laser by an Antimonene-Based Optical Modulator," Laser & Photonics Reviews. 13, 1800313 (2019).

10. L. Wu, X. Jiang, J. Zhao, W. Liang, Z. Li, W. Huang, Z. Lin, Y. Wang, F. Zhang, S. Lu, Y. Xiang, S. Xu, J. Li, and H. Zhang, "MXene-Based Nonlinear Optical Information Converter for All-Optical Modulator and Switcher", Laser & Photonics Reviews. 12, 1800215 (2018).

11. S. L. Jiang, F. F. Chen, Y. Zhao, S. F. Gao, Y. Y. Wang, H. L. Hoi, and W. Jin, "Broadband all-fiber optical phase modulator based on photo-thermal effect in a gas-

filled hollow-core fiber," Opto-Electron Adv. 6, 220085 (2023).

12. Y. Bai, H. Yu, Y. Zhang, Z. Miao, C. He, R. Dou, Y. Zhang, and X. Lin, "Phase noise of the near-infrared single-mode fiber Mach–Zehnder interferometer and its stabilization technology," Appl. Opt. 60, 2652-2656 (2021).

13. H. Bao, Y. Hong, W. Jin, H.L. Ho, C. Wang, S. Gao, Y. Wang, and P. Wang, "Modeling and performance evaluation of in-line Fabry-Perot photothermal gas sensors with hollow-core optical fibers," Opt. Express. 28, 5423-5435 (2020).

14. C.N.T. Mori, and E.C. Romão, "Numerical simulation by FDM of unsteady heat transfer in cylindrical coordinates," Applied Mechanics and Materials. 851, 322–325 (2016).

15. H. Kragh, "The Lorenz-Lorentz formula: origin and early history," Substantia. 2, 7-18 (2018).

16. D. R. Lide, "CRC Handbook of Chemistry and Physics: A ready-reference book of chemical and physical data," CRC Press, Boca Raton (2004).

17. L. V. Gurvich, I. V. Veyts, and C. B. Alcock, "Thermodynamic Properties of Individual Substances", Hemisphere, New York. 4th ed., Vols. 1-2 (1989).

18. https://refractiveindex.info

19. M. Digonnet, S. Blin, H. K. Kim, V. Dangui, and G. Kino, "Sensitivity and stability of an air-core fibre-optic gyroscope," Measurement Science & Technology. 18, 3089-3097 (2007).

20. S. Gao, Y. Wang, C. Tian, and P. Wang, "Splice loss optimization of a photonic bandgap fiber via a high v-number fiber," IEEE photonics technology letters. 26, 2134-2137 (2014).

Chapter 7 Conclusions and future works

7.1. Conclusions

In this thesis, we have studied the optical fiber photothermal spectroscopy for gas sensors and phase modulators. The contributions of this thesis can be summarized as follows:

(1) We proposed a technique with the sensing region formed by an air gap between the cleaved ends of two single-mode fibers (SMFs). Compared to hollow-core fiber (HCF), the short air gap can enhance the photothermal (PT) efficiency and reduce the system noise, since the mode field coming out from the SMF is considerably smaller than that of the HCF, resulting in higher pump power density and thus higher local heating and larger PT modulation per unit length. Meanwhile, the SMF has better mode purity, and the very small gas distance means the two interference beams return to the SMF almost simultaneously, making the system insensitive to external disturbance. An FO-PTS sensor with such a short air gap was demonstrated with fast response and large dynamic range. We presented the theoretical formulations of photothermal (PT) phase modulation and interferometric phase detection, and carried out the numerical simulation and experimental investigation to optimize the system parameters to maximize the PT signal. A gas sensor with an air gap of 130 μm demonstrated a limit of detection (LOD) of 45 parts per billion (ppb) for acetylene detection. The dynamic range and response time of the sensor were 2×10^7 and 0.9 s, respectively.

(2) A pump-probe-alternating technique was proposed for gas sensing based on FO-PTS. In conventional FO-PTS systems, in addition to the pump lasers tuned to the specific absorption lines of the target gas species, an additional laser is used as the probe beam for PT phase detection. The proposed approach eliminates the need for

an additional laser. For example, it requires only two lasers, instead of three, to detect two gas components by operating the lasers alternately as pump and probe beams via time-division multiplexing. A servo controller is used to tune the wavelength of the probe beam away from the absorption lines of the gas and simultaneously stabilize it at the quadrature point of interferometric fringes after each switching action. A gas sensor with a 2.5-cm-long HCF presented LODs of 400 ppb and 130 ppb for methane and acetylene detection, respectively. The proposed technique enables the construction of a sensitive yet more compact and cost-effective PTS system for multi-component gas sensing.

(3) We investigated a fiber-enhanced Fourier-transform photothermal spectroscopy (FT-PTS) technique for multi-species gas sensing. In conventional FO-PTS systems for multiple gas sensing, multiple pump lasers are required to be tuned to the specific absorption lines of the target gas species and the number of the pump lasers is normally equal to that of the target gas species. The proposed technique combines the FO-PTS with Fourier-transform spectroscopy to enable multiple gas sensing with a single pump beam. A broadband light source is used as the pump beam with the light intensity modulated at different frequencies for different wavenumbers. The PT spectrum is acquired after Fourier transform of the measured interferogram. A gas sensor with a 10-cm-long HCF presented noise equivalent concentrations (NECs) of ~465 ppb and ~457 ppm for detection of acetylene and carbon dioxide, respectively. The system is applied for detection of two-component gas of acetylene and carbon dioxide. The proposed PTS system is more compact and cost-effective for multi-component gas sensing, making it attractive for a wide range of practical applications.

(4) We explored the FO-PTS with HCFs for the application of phase modulators. We investigated the modulation performance of PMs based on HCFs filled with acetylene of different concentration balanced with buffer gases of argon, nitrogen

and helium. The largest phase modulation is achieved with acetylene balanced with argon. For HCF with a fixed length, there exists an optimal gas concentration to achieve maximum phase modulation. With a 23-cm-long hollow-core anti-resonant fiber (HC-ARF) filled with 12.5% acetylene balanced with argon, we demonstrated phase modulation of π-rad at 100 kHz with control light power of ~200 mW. The -3dB modulation bandwidth is ~150 kHz. By using a hollow-core photonic bandgap fiber (HC-PBGF) of the same length and gas concentration, we achieved -3dB modulation bandwidth of 1.1 MHz, the highest among all the reported fiber-based all-optical PMs to our knowledge. The measured rise and fall time of HC-PBGF-based modulator are 0.57 μs and 0.55 μs, respectively, one order of magnitude smaller than those based on the HC-ARF.

7.2. Future works

So far, we have demonstrated the FT-PTS to detect multiple gases with only one pump source. The performance of the FT-PTS system may be further improved along the following directions:

(1) Using more information from the measured spectra, such as by multiple measurements to reduce the white noise, by using the peak areas rather the peak heights, or by fitting of the whole spectral region with methods of classic least-squares (CLS), partial least-squares (PLS) or iterative nonlinear least-squares (NLLSQ).

(2) Using a supercontinuum source (SC) as the pump beam to provide a wider spectrum to enable the detection of more gases.

(3) Using a mid-infrared (MIR) source as the pump beam, since gases normally have higher absorption coefficients in the MIR region and MIR photodetectors may be unnecessary by keeping a near-infrared laser as the probe beam [1].

7.3 References

1. F. Chen, S. Jiang, H.L. Ho, S. Gao, and Y. Wang, “Frequency-division-multiplexed multicomponent gas sensing with photothermal spectroscopy and a single NIR/MIR fiber-optic gas cell,” Anal. Chem. 94, 13473–13480 (2022).